Experiments Towards Optical Nuclear Spectroscopy With Thorium-229

Von der Fakultät für Mathematik und Physik der
Gottfried Wilhelm Leibniz Universität Hannover

zur Erlangung des Grades

Doktor der Naturwissenschaften
Dr. rer. nat.

genehmigte Dissertation

von

Dipl.-Phys. Kai Zimmermann
geboren am 25. Dezember 1976 in Berlin

2010

Referent: PD Dr. Ekkehard Peik
Korreferent: Prof. Dr. Ernst Rasel
Tag der Promotion: 10.06.2010

Abstract

The discovery of the low-lying isomeric nuclear state of ^{229}Th at 7.6 ± 0.5 eV above the ground state opened a new field of research as a bridge between nuclear and atomic physics. Since indirect γ-spectroscopy techniques were applied for detection of the isomeric state, the direct observation of the nuclear photon emission is still pending. This thesis describes the steps towards the direct observation of ^{229m}Th.

The first conducted experiments examine measurements of atoms in the isomeric state ^{229m}Th being produced in the α-decay of ^{233}U. Recoil atoms were ejected from a thin ^{233}U source, accumulated in an absorber and analyzed for the emission of UV and VUV photons. No evidence for the decay of the isomeric state was found. The observed background signal has been identified as Cherenkov radiation.

The main part of this thesis describes the setup of a linear Paul trap with a high storage capacity that has been built and loaded with more than $8 \cdot 10^4$ Th^+ ions using laser ablation loading. Laser ablation of thorium ions has been shown using a pulsed nitrogen laser at a wavelength of 337 nm, a pulse energy of 170 μJ and a pulse width of 4 ns in a time-of-flight mass spectrometer. The ratio of ablated Th^+ to Th^{2+} ions was investigated in relation to the laser pulse power. Th^+ ablation from a dried $^{232}Th(NO_3)_4$ solution has been shown from multiple substrate surfaces as a preparation for the loading of the more radioactive ^{229}Th from a minimum amount of substance.

The trapped ions were characterized by ion ejection and counting, electronic detection and optical detection methods. We investigated the loading conditions, trap potentials, the stored ion numbers, buffer gas cooling, the laser ablation velocity distribution, and the phase dependence of the radiofrequency field for the ion loading. Gas discharges were observed between the electrodes in the plasma created by laser ablation, increasing the amount of created ions by collision ionization.

Using an external cavity diode laser, the excitation of the strong resonance line of Th^+ at 401.9 nm has been executed as a first step of a two step excitation of the isomeric state, establishing the means to perform high resolution laser spectroscopy of Th^+ ions. Helium buffer gas cooling to room temperature and depopulation of metastable levels by buffer gas quenching has been shown, thus obtaining a cycling excitation in the multilevel structure of Th^+. The laser excitation was limited due to formation of ThO^+ ions with a time constant of about 45 s.

keywords: Th-229, ion trap, laser spectroscopy

Zusammenfassung

Die Entdeckung des tief liegenden isomeren Kernzustandes von ^{229}Th bei einer Energie von 7.6 $\pm$ 0.5 eV über dem Grundzustand eröffnete ein neues Forschungsgebiet als Brücke zwischen Kern- und Atomphysik. Da indirekte γ-Spektroskopie-Techniken für den Nachweis des isomeren Zustandes angewandt wurden, steht der direkte Nachweis der nuklearen Photonenemission noch immer aus. Diese Arbeit beschreibt die Schritte auf dem Weg zum direkten Nachweis von ^{229m}Th.

Die ersten ausgeführten Experimente behandeln Messungen von Atomen im isomeren Zustand ^{229m}Th, die während des α-Zerfalls von ^{233}U produziert werden. Rückstoß-Atome wurden aus einer dünnen ^{233}U-Quelle ausgestoßen, in einem Absorber gesammelt und auf die Emission von Photonen im UV und VUV untersucht. Es konnte kein Nachweis für den Zerfall des isomeren Zustandes gefunden werden. Das beobachtete Hintergrundsignal wurde als Cherenkov-Strahlung identifiziert.

Der Hauptteil dieser Arbeit beschreibt die Konstruktion einer linearen Paulfalle mit einer hohen Speicherkapazität, die gebaut und mit mehr als $8 \cdot 10^4$ Th^+ Ionen mit Hilfe von Laserablation geladen wurde. Laserablation von Thorium-Ionen wurde mittels gepulstem Stickstoff-Laser bei einer Wellenlänge von 337 nm, Pulsenergie von 170 μJ und 4 ns Pulsbreite in einem Flugzeit-Massenspektrometer nachgewiesen. Das Verhältnis von Th^+- zu Th^{2+}-Ionen wurde in Abhängigkeit der Laserpulsleistung untersucht. Ablation von Th^+ aus einer getrockneten $^{232}Th(NO_3)_4$-Lösung wurde unter Verwendung verschiedener Substratmaterialien als Vorbereitung des Ladens des stärker radioaktiven ^{229}Th aus einer minimalen Substanzmenge gezeigt.

Die gespeicherten Ionen wurden mittels Ionenausstoß und -zählen, elektronischen und optischen Nachweismethoden charakterisiert. Wir untersuchten die Ladebedingungen, Fallenpotentiale, Ionenspeichervermögen, Puffergaskühlung, Geschwindigkeitsverteilung der ablatierten Ionen und die Abhängigkeit des Ionenladens von der Phase des Fallenfeldes. Es wurden Gasentladungen, die die Anzahl der Ionen durch Stoßionisation erhöhen, zwischen den Elektroden im erzeugten Plasma beobachtet.

Mit einem Diodenlaser wurde die Anregung der starken Th^+-Resonanzlinie bei 401,9 nm als erster Schritt einer Zwei-Photonen-Anregung des isomeren Zustands durchgeführt. Dies bildet die Basis für hochauflösende Laserspektroskopie an Th^+ Ionen. Helium-Puffergaskühlung auf Raumtemperatur und die Entvölkerung metastabiler Zustände durch Stöße mit dem Puffergas wurden gezeigt, wodurch eine zyklische Anregung in dem Vielniveausystem Th^+ ermöglicht wird. Die Laseranregung wurde limitiert durch Bildung von ThO^+ mit einer Zeitkonstante von 45 s.
Schlagworte: Th-229, Ionenfalle, Laser Spektroskopie

Contents

1 Introduction **1**

2 The Low-Lying State of ^{229}Th **5**
2.1 Nuclear Structure of ^{229}Th 5
2.2 Search for the Isomeric State Transition 15

3 Thorium Recoil Nuclei **22**
3.1 Production and Detection of Recoil Nuclei 22
3.2 Temporal Decay Curves 29
3.3 Spectral Analysis 34

4 Laser Ablation Ion Production **36**
4.1 Setup and Time-of-Flight Principle 36
4.2 Thorium Sample Preparation 42
4.3 Ablation of Thorium Ions 44

5 Thorium in a Linear Paul Trap **52**
5.1 The Linear Paul Trap 52
5.2 Experimental Setup 59
5.3 Resonant Electronic Detection 67
5.4 Ion Detection with a Channeltron 71

6 Laser Excitation of Th^+ **80**
6.1 Optical Setup 81
6.2 Fluorescence Detection 83

7 Summary and Outlook **89**

Bibliography **92**

1 Introduction

The dawn of nuclear physics was the discovery of radioactivity in 1896 by Henry Becquerel [1]. The Rutherford scattering experiment in 1910 revealed the existence of a very small, very dense positively charged nucleus containing most of the atom's mass that is surrounded by electrons, balancing out the charges to a neutral atom. Atomic and nuclear physics were at the crossroads and started to separate into two different branches of physics.

Atomic physics studied the interactions in the electron shell of the atom and evolved with the development of the laser into a high-precision science. Powerful tools for manipulating atoms such as laser cooling [2] and spectroscopy with optical frequency combs [3] were developed. Nowadays, spectroscopy on selected transitions can reach uncertainties of 10^{-17} [4].

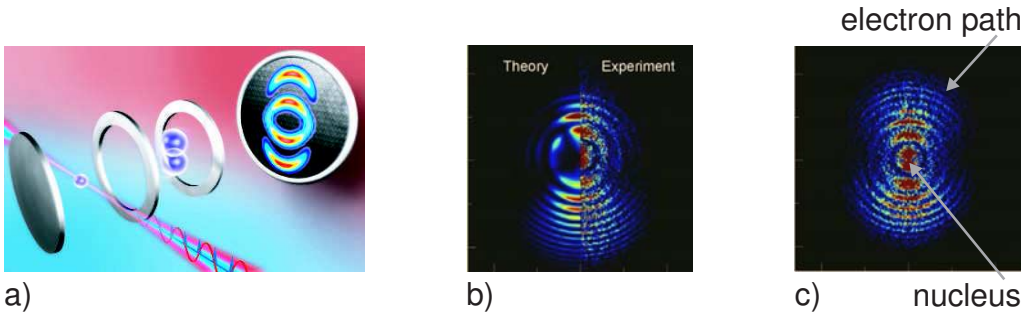

Figure 1.1: a) Scheme of attosecond laser interferometry [5] for visualizing the atomic shell. b) Experimental and Theoretical results of helium in a quantum stroboscope based on a sequence of identical attosecond pulses that are used to release electrons into a strong infrared laser field exactly once per laser cycle [6]. c) The nucleus is still three orders of magnitude smaller and invisible in the center of the electron trajectory.

In contrast, nuclear physics investigated not the atomic shell but the nucleus of the atom and examines the composition of matter itself. Nuclear fusion and fission entered a complete new energy region and γ-spectroscopy helped understanding the inner structure of nuclei. High-resolution methods were established such as nuclear magnetic resonance spectroscopy [7], used to observe transitions between nuclear

spin energy levels in a magnetic field and Mössbauer spectroscopy [8], which in solid samples allows to detect recoil-free absorption of γ-rays in nuclei.

Whilst atomic and nuclear physics made progress in their research fields, they distanced themselves from each other, most noticeable separated by energy. Typical energy values in the atomic shell are on the order of a few electron volt whereas nuclear excitation levels and α-energies can be observed on the order of several MeV. This energy difference requires completely different techniques for detection and manipulation and to this date it was not possible to apply well understood and developed atomic physics techniques to examine the nucleus.

Mössbauer spectroscopy is an important tool in nuclear physics but has the disadvantage that it provides only relative measurements and has to deal with big energies. The sensitivity and resolution of Mössbauer spectroscopy and the interaction with the nuclear environment could be enhanced when working with lower energies. The detection of the isomeric energy state of ^{235}U at 76.5 eV above the ground state [9] with a half-life of 27 minutes [10] was the first time that the energies were low enough to observe interactions of the atomic shell with the nucleus. The isomeric state $^{235\mathrm{m}}$U decays entirely by internal conversion and the subsequent emission of electrons [11].

Low-lying nuclear energy states open new ways of merging atomic and nuclear physics and manipulating decay channels of nuclear isomeric states by laser interaction with the atomic shell [12]. Laser-assisted internal conversion processes change the atomic surroundings of the nucleus and can lead to a significant decrease of the coefficient of internal conversion for example by removing one of the electrons that significantly contribute to the internal conversion [13].

A more powerful way to use the electron shell as a mediator between a laser beam and the nucleus for studying nuclear low-energy properties is provided by the electronic bridge process [14]. In this process, the energy of the nucleus is transferred to the atomic shell that is excited to an intermediate state and photons are emitted during the decay of this intermediate to the final state. Usually dealing with high energies and competing processes, the observation of nuclear deexcitation via the electronic bridge process is difficult to detect due to low resolution and small contributions to the decay channels [15]. The electronic bridge process is a third-order process with respect to the electromagnetic interaction and is usually accompanied by processes connected with internal conversion. These effects being second-order processes are more probable than electronic bridge processes and produce strong background effects as for example bremsstrahlung associated with the internal conversion of the nuclear level and the emission of fast electrons.

To study and manipulate electronic bridge processes, the suppression of internal conversion effects is necessary. Using lasers to excite selected atomic levels, it is then possible to enhance or avert decay channels for nuclear isomeric states. Unfortunately, the elimination of the internal conversion channel is usually not possible, because γ-ray energies generally exceed the ionization potential of the

atomic shell. If a nucleus was found with an energy of the excited nuclear state lower than the ionization potential, it would provide a completely new access to the electronic bridge process and the manipulation of nuclei with lasers.

The detection of the low-lying isomeric state of ^{229}Th [16] may provide this bridge between atomic and nuclear physics. The ^{229}Th nucleus has an excited state at only 7.6 eV above the ground state [17], several orders of magnitude smaller than usual nuclear excitation energies. Therefore, investigating $^{229\mathrm{m}}$Th has the power to provide a link between nuclear and atomic physics and examine the nuclear structure with high-precision spectroscopy methods. Thorium has a ionization energy of 6.08 eV and working with Th^+ will prohibit the internal conversion process due to the second ionization energy of 11.5 eV, opening an inimitable access to the electronic bridge process. This makes ^{229}Th a unique and outstanding system in physics. The last major obstacle before entering this new world of opportunities is the direct detection and confirmation of the isomeric state of ^{229}Th.

The estimated lifetime of 1–4 hours of the isomeric state predicts a natural linewidth of this nuclear transition on the order of 10 μHz and the quality factor of the resonance can approach 10^{20}. Additionally, the nuclear resonance shows an extraordinary insensitivity to external perturbations. Broadening and resonance shifts [18] can by effectively eliminated using ion trapping techniques [19]. This makes the ^{229}Th resonance a remarkable candidate for the reference of an optical clock that will be highly immune to systematic frequency shifts [20].

No one succeeded to detect the isomeric state directly so far. All observations of $^{229\mathrm{m}}$Th are based on indirect γ-spectroscopy measurements [16, 17] and are burdened with high uncertainties [21]. Several difficulties meet the experimenter in the task of the observation of $^{229\mathrm{m}}$Th. The interaction with the electron shell is not satisfactory known and presents an additional complication to the understanding of the nuclear properties. The radius of the nucleus is on the order of a few femtometer while a photon energy of 7.6 eV corresponds to a wavelength of 163 nm. The difference of approximately eight orders of magnitude is sometimes denoted as an antenna problem and is a challenge for direct excitation of the nucleus.

The missing piece for further experiments on $^{229\mathrm{m}}$Th is the knowledge of the exact value of the energy of the isomeric state. γ-spectroscopy measurements disclosed the energy to 2 decimal places. Optical spectroscopy can measure up to 17 decimal places. Closing this gap is the first main objective for experiments with ^{229}Th.

This thesis describes several steps towards the detection of the isomeric state. In the first conducted experiments for the detection of γ-rays, that is to say 7.6 eV photons emitted from the nucleus, $^{229\mathrm{m}}$Th atoms were accumulated after being ejected from a thin uranium source during the α-decay of ^{233}U using recoil energies. This method allowed to collect thorium atoms in the isomeric state and implant them on a substrate without background from the uranium. As it will be seen in chapter 3, even a low background can disturb measurements significantly and the setup of an ion trap is concluded as the best way to investigate ^{229}Th in a

controlled environment. Using ^{232}Th to perform tests without the constraints to work with highly radioactive samples, laser ablation loading is studied in chapter 4 as a new and easy way to produce ions and load them into an ion trap. A linear Paul trap with a high storage capacity is described in chapter 5 and loaded with up to 10^5 thorium ions using laser ablation. The characterization of the trap with a channeltron and electronic detection allowed to study loading methods and properties of Paul traps. To establish an excitation and fluorescence detection scheme for thorium, the trapped ion cloud has been excited on the strong resonance line at 401.9 nm. Buffer gas cooling and quenching was established and studied using this resonance line as described in chapter 6, founding the base necessary for the observation of the isomeric state of ^{229}Th by laser excitation of Th^+.

2 The Low-Lying State of ^{229}Th

It is advisable to survey all facts known about thorium so far before starting the search for the isomeric state ^{229m}Th of ^{229}Th. While section 2.1 will recapitulate the most important properties of ^{229}Th that are useful for the search for ^{229m}Th, the history of the quest for the isomeric state is outlined in section 2.2.

2.1 Nuclear Structure of ^{229}Th

^{229}Th seems to be a unique system in nuclear physics since it is the only known nucleus possessing an isomeric state with an excitation energy in the range of optical photon energies and outer-shell electronic transitions. The energy level of 7.6 eV above the ground state as shown in figure 2.1 is significantly lower than the next known low-energy level at 76.5 eV of ^{235}U [22] and therefore the ^{229m}Th nucleus stands out in its unrivaled capability of being excited by laser radiation. Figure 2.1 summarizes the presently known spectroscopic properties of the low-energy transition in ^{229}Th.

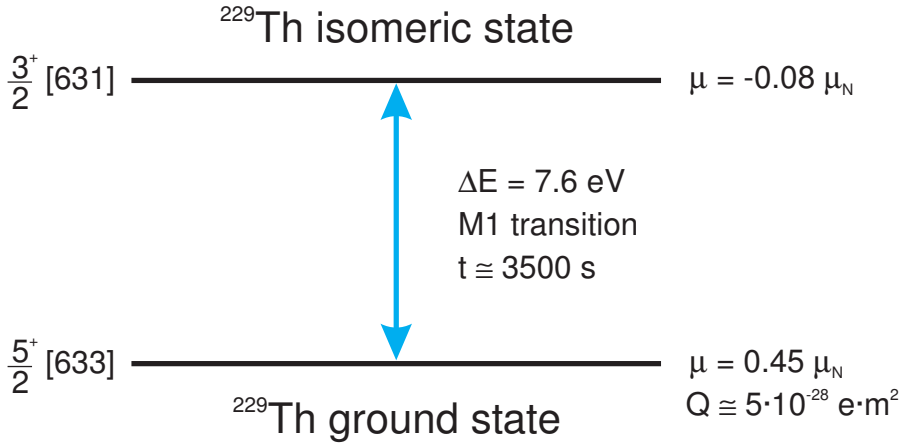

Figure 2.1: The lowest nuclear levels of ^{229}Th [17] with their nuclear spin and Nilsson state classifications [23], radiative lifetime for the magnetic dipole transition [24], the magnetic moments in nuclear magnetons [25] and the quadrupole moment Q of the ground state [26].

The decay of the isomeric state is possible via processes of different order. The direct emission of a γ-quantum is a first order process and will determine the natural linewidth. The direct γ-emission is considered in section 2.1.3. Internal conversion is a second order process since it involves a transfer of the energy to the atomic shell and the subsequent emission of an electron. This second order process is possible in neutral thorium atoms since the ionization energy of 6.08 eV is lower than the energy of the isomeric state. The second and third ionization potential of 11.504 eV and 20.003 eV avert this process for thorium ions. Internal conversion is highlighted in section 2.1.4. The electronic bridge process as a third order process involves the transfer of the energy from the nucleus to an intermediate bound state of the atomic shell and the following emission of a photon during the decay of this atomic state. It will play an important role for thorium ions as pointed out in section 2.1.5.

The radiative lifetime of $^{229\mathrm{m}}$Th [24] is still under discussion but is assumed to be at about 3500 s in an isolated nucleus. The lifetime as well as the influence of different electronic environments is considered in sections 2.1.3 and 2.1.4. Different magnetic moments [25,26] for the ground and the isomeric state offer a way for the detection of the isomeric state via the atomic shell as noted in section 2.1.6. This could help building a nuclear clock and searching for variations of fundamental constants which is discussed in section 2.1.8.

2.1.1 Band Structure and Nilsson States

The nuclear band structure for ^{229}Th is shown in figure 2.2. The transition from the ground state to the isomeric state is a transition between the heads of the two lowest rotational bands. The characterization of the nuclear levels is based on the nuclear shell model with axially symmetric elliptical potential, a phenomenological approach to the parametrization of the nuclear potential developed by S. G. Nilsson [27].

The Nilsson state classification characterizes the shape of the nucleus in an elliptical deformed oscillator potential $V(\boldsymbol{r})$ [28] where the z-axis is the symmetry axis of the rotational ellipsoid so that $\omega_{xy} = \omega_\perp$. The solutions of the associated Hamilton operator with a constant influence of the spin-orbit coupling $V_{\boldsymbol{ls}} = const = C < 0$ that is enhanced with an interpolation term with $D = const < 0$ to match the Woods-Saxon-Potential [29] of the nucleus in the form

$$H = -\frac{\hbar^2}{2m}\Delta + \frac{m}{2}\left(\omega_\perp^2\left(x^2+y^2\right) + \omega_z^2 z^2\right) + C(\boldsymbol{l}\cdot\boldsymbol{s}) + D\boldsymbol{l}^2 \tag{2.1}$$

$$= -\frac{\hbar^2}{2m}\Delta + V(\boldsymbol{r}) + C(\boldsymbol{l}\cdot\boldsymbol{s}) + D\boldsymbol{l}^2 \tag{2.2}$$

$$= -\frac{\hbar^2}{2m}\Delta + V_N(\boldsymbol{r}) \tag{2.3}$$

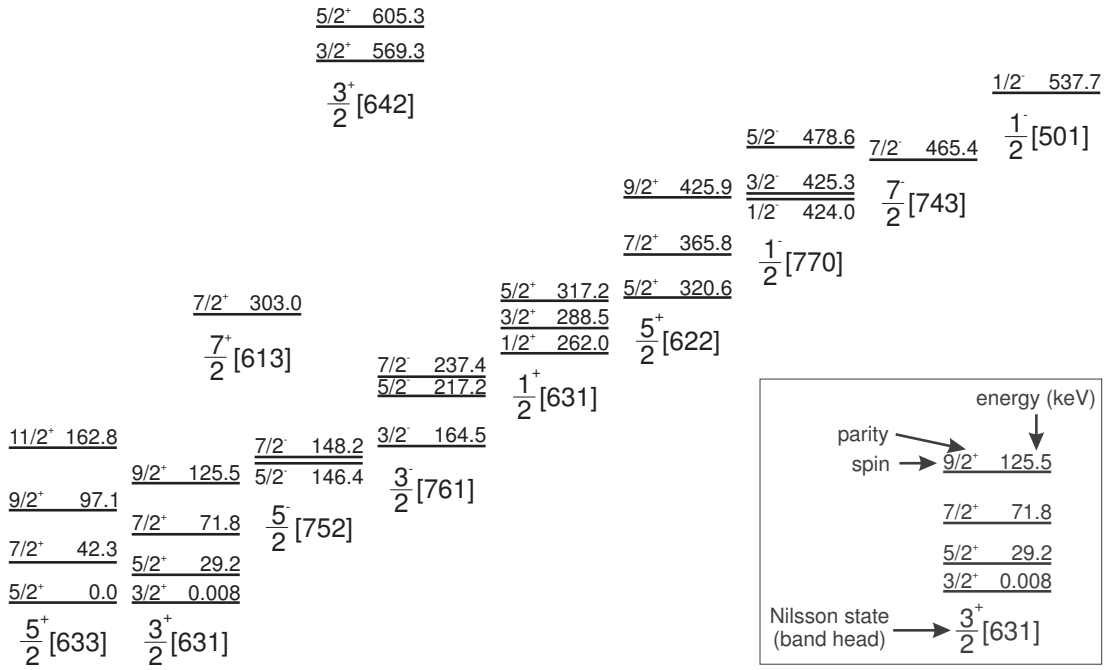

Figure 2.2: Experimental levels in ^{229}Th grouped into rotational bands [24].

lead to state energies of the nucleons as a function of a deformation parameter δ, which is proportional to the difference between the big and the small axis of this rotational ellipsoid. For $\delta < 0$ the deformation is oblate (lens-shaped), $\delta > 0$ is a prolate (cigar-shaped) deformation and $\delta = 0$ is a spherical shape of the nucleus.

The movement of the nucleons in the Nilsson potential $V_N(\boldsymbol{r})$ can be separated in independent oscillators along and perpendicular to the nuclear symmetry axis z. The eigenvalues of the energy are calculated to

$$E(n_z, n_\perp) = \hbar\omega_z(n_z + \frac{1}{2}) + \hbar\omega_\perp(n_\perp + 1) \ , \qquad n_\perp = n_x + n_y \tag{2.4}$$

with

$$\omega_\perp^2 = \omega_0^2\left(1 + \frac{2}{3}\delta\right) \ , \quad \omega_z^2 = \omega_0^2\left(1 - \frac{4}{3}\delta\right) \ , \quad \omega_0(\delta) = \hat{\omega_0}\left(1 - \frac{4}{3}\delta - \frac{16}{27}\delta^3\right)^{-\frac{1}{6}} \tag{2.5}$$

where $\hat{\omega_0}$ is the oscillator frequency of the undeformed nucleus and the total number of oscillator quanta is

$$N = n_z + n_\perp \ . \tag{2.6}$$

The term $D\boldsymbol{l}^2$ lifts the degeneracy with regard to $\boldsymbol{l}$ of the standard single particle shell model [30] and the degenerated states with a fixed $n_\perp$ can be described with the projection of $\boldsymbol{l}$ on z to

$$\Lambda = \pm n_\perp, \pm(n_\perp - 2), \ldots, \pm 1 \text{ or } 0 \; . \tag{2.7}$$

With the parity and the projection Ω of the nuclear total angular momentum I on the symmetry axis z, the set of quantum numbers known as Nilsson classification can be written as

$$\Omega^\pi[N, n_z, \Lambda] \tag{2.8}$$

and is noted for ^{229}Th in figure 2.1 and figure 2.2.

The Nilsson diagram in figure 2.3 is an example for a graphical representation of the single-particle state dependence on the deformation parameter δ. This scheme becomes more complicated for nuclei with higher quantum numbers but can nevertheless be calculated.

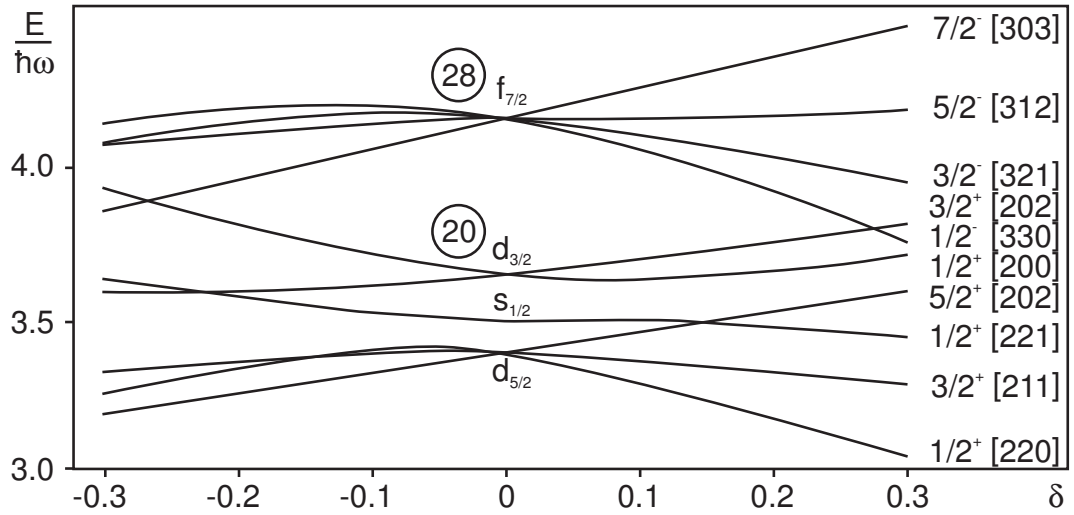

Figure 2.3: Example for single-particle states for an axially symmetric elliptical Nilsson potential, shown for nuclei with $8 < Z < 28$ [28].

Using the distribution of the excited states in the rotational bands [24, 31] and comparing these positions with the Nilsson diagram, it is possible to calculate the deformation parameter δ [32, 33]. The fits are based on the measured values of the quadrupole moments and result in a small positive deformation parameter of about $\delta \approx 0.1$ for ^{229}Th. This leads to a prolate deformation of the nucleus in the ground state as well as in the isomeric state.

2.1.2 The Neptunium Series

The ^{229}Th isotope is radioactive with a half-life of 7880 years. It is part of the Neptunium series [28] shown in figure 2.4.

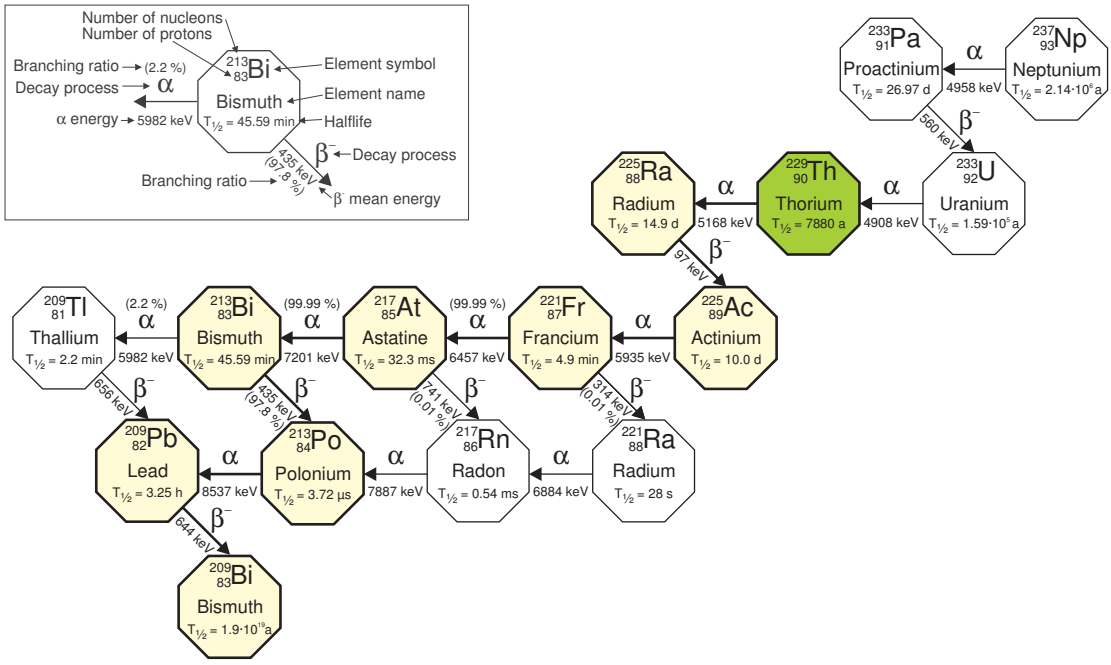

Figure 2.4: The neptunium series. The main decay channel of ^{229}Th is marked in yellow. All noted energies of α- and β-decays are mean values of all emitted particle energies.

The radioactive displacement laws [34] identify four different natural radioactive decay chains since in nature only α- and β^--decays change a nuclide. Due to the ^{237}Np half-life of $2.14 \cdot 10^6$ years, the Neptunium series is the only extinct series on earth and elements in this series have to be produced by nuclear reactions.

Some elements in the Neptunium series have both, α- and β-decay channels. While ^{221}Fr and ^{217}At have a 99.99% probability for an α-decay, ^{213}Bi will decay with a 97.8% chance in a β-decay. The main decay channel is colored in figure 2.4. In all cases the final element is ^{209}Bi that can be considered stable due to a half-life of $1.9 \cdot 10^{19}$ years.

The elements in the Neptunium series lighter than thorium have half-lives between a few μs and two weeks. The background signal produced by the decay of these elements will increase with the age of the thorium sample and has to be considered when conducting experiments with $^{229\mathrm{m}}$Th and is further discussed in section 3.2.1.

2.1.3 Lifetime of the Isomeric State

The lifetime for the α-decay of ^{229}Th depends on the state of the nucleus. By analyzing the excited states of the ^{225}Ra nucleus following the ^{229}Th and $^{229\mathrm{m}}$Th decay, it is estimated that the α-decay half-life of the isomeric state is about 2–4 times smaller than the half-life of 7880 years of thorium in the ground state [35].

The estimations for the radiative lifetime of the isomeric state vary between a few minutes [36] and several days [16]. The lifetime is determined by different effects that have to be considered.

Because of the emission of dipole radiation, the lifetime for $^{229\mathrm{m}}$Th has a cubic dependency on the energy of the isomeric state by

$$T_{\frac{1}{2}} = \frac{10.95\,\mathrm{h}}{E_\gamma^3 \cdot \mathrm{B(M1)}} \tag{2.9}$$

with the reduced magnetic dipole transition probability $B(M1) = 0.025\,\mu_N^2$ obtained from quasiparticle-plus-phonon model calculations, where E_γ is given in eV [24]. With $E_\gamma = 7.6 \pm 0.5$ eV, this leads to an estimated lifetime of 3500^{+900}_{-600} s. The estimation for the lifetime depends on the applied nuclear model and is therefore burdened with a high uncertainty.

In addition, the lifetime depends on the availability of other decay channels that can shorten the lifetime significantly. While the ionization energy of neutral ^{229}Th of 6.08 eV provides a radiationless internal conversion decay channel that will shorten the lifetime, this decay channel is not available in $^{229\mathrm{m}}$Th$^+$ as the second ionization potential is 11.504 eV. Depending on the precise value of the energy of the isomeric state, the level structure of the electron shell may possess a resonant level that provides a coupling between the nucleus and the electron shell and opens an electronic bridge decay channel that can shorten the lifetime (see section 2.1.5). If $^{229\mathrm{m}}$Th is implanted in other elements as metals, semiconductors or crystals, the electronic environment may provide an additional radiationless decay channel.

2.1.4 Electronic Environment

When a $^{229\mathrm{m}}$Th nucleus is inserted into a metal, the predominantly decay channel of the isomeric state will be via conduction electrons or via electrons from the valence band if the energy of the isomer exceeds the Fermi energy [37]. This decay can be interpreted as internal conversion with the initial state of the electron not being a bound state of the atomic shell. In a simple free-electron approximation [38], the lifetime of $^{229\mathrm{m}}$Th in a metal will reduce to 10^{-4} s [39], making this radiationless decay the dominant decay channel.

The situation is similar when $^{229\mathrm{m}}$Th is injected into a semiconductor. Most semiconductors will have a band gap that is smaller than 7.6 eV, allowing the nucleus to transfer its energy to an electron and move it to the conduction band

where the energy will be dissipated radiationless. Even if the band gap is bigger than the energy of the isomer, the nucleus will occupy a position in the semiconductor lattice and induce a perturbation in the initial band structure, leading to additional levels in the forbidden band. These levels will assist the energy transfer and may lead to a radiationless energy dissipation as well [40].

This leads to the conclusion that for experiments searching for the direct emission of γ-rays from the ^{229}Th nucleus on a surface or in a crystal, only dielectric materials can be chosen. Materials which are transparent in the spectral range of interest, for example calciumfluoride, will generally fulfill this requirement. However, the lifetime may still be shortened in a dielectric environment, depending on the refractive index of the dielectric material [41].

2.1.5 Electronic Bridge Process

Due to the low energy of the isomeric state, the influence of the electronic bridge (EB) process [14, 42] as a third order process where the atomic shell is used as a mediator for the depopulation of the isomeric will become more important than for nuclei with higher excitation energies. This process had been proposed soon after the detection of the isomeric state of ^{229}Th [43,44] and opens a way to depopulate and to excite the isomeric state [13].

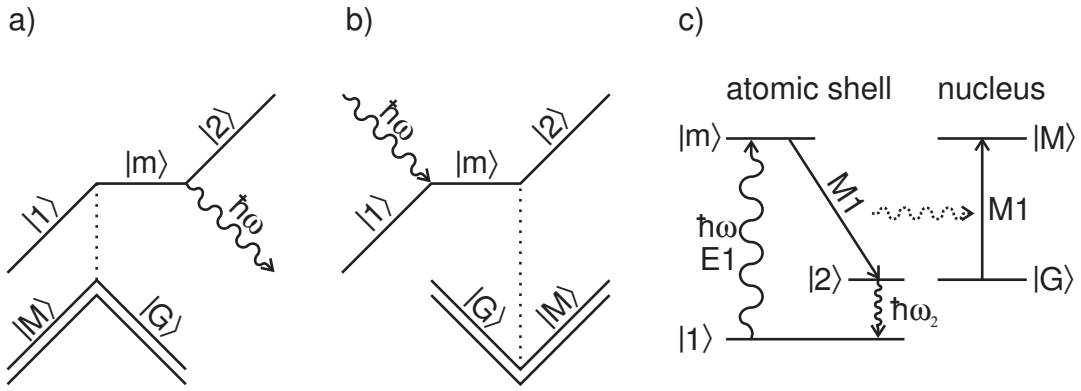

Figure 2.5: Feynman graphs of a) the electron bridge process and b) the inverse electron bridge process. The interaction between the nucleus and the atomic shell is marked with dashed lines. G denotes the nuclear ground state, M denotes the nuclear isomeric metastable state. 1,m,2 are the atomic initial, metastable and final state. Scheme c) shows the inverse electronic bridge process for ^{229}Th. The energy mismatch between isomeric and atomic states is balanced by a photon. State $|2\rangle$ can be a real or a virtual level.

The process strongly depends on the existence of resonant levels in the atomic shell. As noted in figure 2.5a, the first step of the EB process involves the resonant radiationless transfer of the energy to the atomic shell and will excite the atom to an intermediate state. This metastable state will decay to a final state and emit a photon with the energy corresponding to the difference between the intermediate and the final state. The probability for this process can be enhanced significantly by exciting the atomic shell with a laser to a state that matches the resonance condition for the isomeric state and the initial and intermediate state of the atomic shell [15]. In this scheme, the depopulation of the isomeric state can only be detected by photons with a lower energy than the excited state of the nucleus [45].

This process can be used to excite the isomeric state with the inverse electronic bridge process (IEB)[1] [46]. The process shown in figure 2.5b excites the atom with laser radiation to an intermediate state. The energy is transferred to the nucleus and the atomic shell decays to the final state. In the ^{229}Th nucleus, the probability strongly depends on the existence of an intermediate state with the correct energy, spin and parity to fulfill the resonance condition that can excite the isomeric state ^{229m}Th with a magnetic dipole transition.

2.1.6 Hyperfine Structure and double-resonance Detection

The level structure of the atomic electron shell is modified by the hyperfine interaction between the electrons and the nuclear electric and magnetic moments. In the nuclear transition from ^{229}Th to ^{229m}Th, the nuclear spin changes by $\hbar$ and the magnetic moment by about 0.5 nuclear magnetons [25] as seen in figure 2.1. For the 7s electronic state this will lead to a change of the hyperfine splitting of several gigahertz [20].

This can be used for a double-resonance detection of the excitation of the isomeric state as shown in figure 2.6 by performing laser spectroscopy of the electron shell. When the nucleus is in the ground state, a laser that is tuned to a closed two-level electric-dipole transition of the shell will constantly produce resonance fluorescence photons scattered from the atom. When the nucleus is excited to the isomeric state, the change of the nuclear spin and the nuclear magnetic moment induces a change of the hyperfine splitting. The laser used for driving the closed two-level system will be out of resonance and the fluorescence intensity will drop [20].

The involved electronic transition has to have a sufficiently lower energy than the energy difference between the ground state and the isomeric state of the nucleus to avoid inducing an electronic bridge process (see section 2.1.5) and decreasing the lifetime of the isomeric state. This would be the case for the 401.9 nm laser for the two-stage excitation in section 2.1.7.

[1] The IEB and EB processes are also known as nuclear excitation by electronic transition (NEET) and transfer of energy by electrons from nuclei (TEEN)

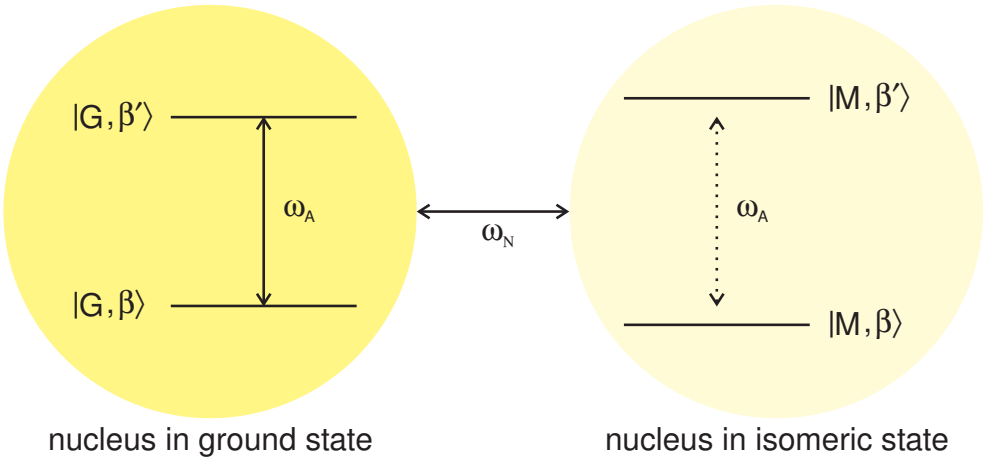

Figure 2.6: Scheme of the double-resonance detection of the excitation of the isomeric state.

This method is similar to the electron shelving scheme for the detection of metastable states in the shell of a single trapped ion [47] and similar schemes are used in high-resolution laser spectroscopy of trapped ions [19]. The repeated excitation and decay of the isomer will lead to a sequence of periods of high and low fluorescence intensity. Additionally, a third laser could be used that is tuned in resonance with a closed two-level system of the shell of the isomer. This would lead to a constant scattering of photons from the atom with wavelengths corresponding to the energy difference for the electronic two-level system of the nucleus in the ground state or the isomeric state and thus indicating the state of the nucleus [20].

2.1.7 Two-Stage Excitation

The energy of 7.6 ± 0.5 eV corresponds to a wavelength of 163^{+11}_{-10} nm. Unfortunately, no widely tunable lasers are available in this spectral region. Additionally, this laser radiation has to be generated and transmitted in vacuum since photons with a wavelength shorter than 180 nm are absorbed by oxygen.

To overcome the obstacle of generating laser radiation with an energy matching the energy of the isomeric state, the atomic shell may be used as a mediator as shown in figure 2.7. In this scheme, the energy will be provided by several photons to the atomic shell before transferring the energy to the nucleus with the inverse electronic bridge process as described in section 2.1.5.

The atomic level for the IEB process will be excited in two steps by two different lasers. Since the ionization energy of neutral thorium exceeds the energy of the isomeric state, ionized ^{229}Th has to be used to excite the atomic shell. The first excitation step involves a laser at a fixed wavelength tuned at the strong resonance line of Th^+ at 401.9 nm. Starting from this level at 24 874 cm^{-1}, a tunable laser

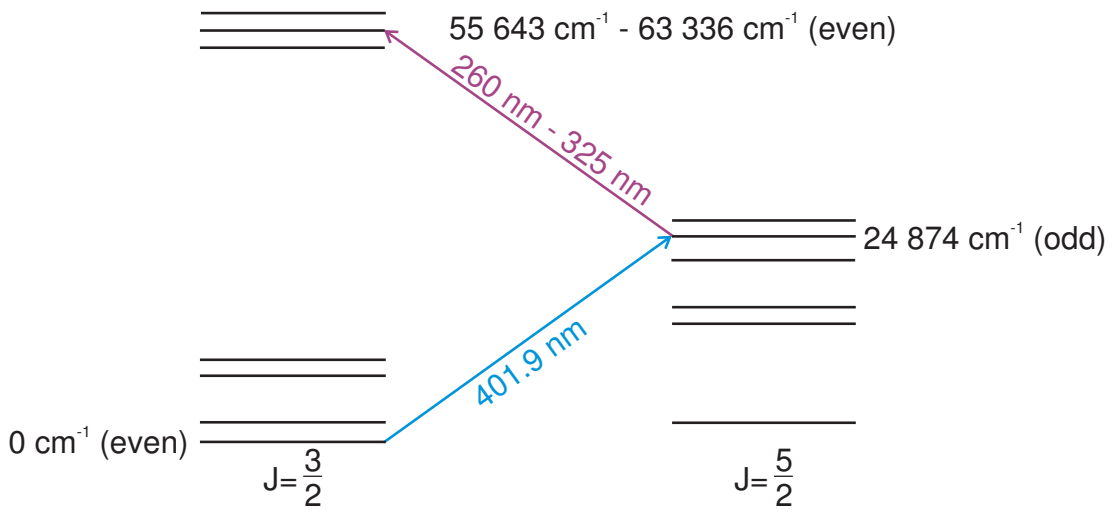

Figure 2.7: Schematic of the two-stage excitation in Th^+.

will excite a state in the atomic shell with an energy comparable to the ^{229m}Th energy level. Th^+ has a dense level scheme that can be used to match the IEB conditions.

Due to the big uncertainty of the isomeric state energy, the second laser will have to be tuned in a wide spectral range. The probability for the occurrence of the inverse electronic bridge process depends strongly on the parameter of the attained atomic state. Besides the energy matching of isomeric and atomic state, the selection rules for magnetic dipole transitions have to be fulfilled for the atomic states before and after the excitation of the nucleus. Since the energy of the isomeric state is not known, the best matching state cannot be predicted but has to be identified by double-resonance detection or direct detection of a γ-ray of the decaying isomeric state.

2.1.8 Variation of Fundamental Constants

The unique system of ^{229}Th with its low excitation energy accessible by laser radiation and the very narrow linewidth of about 10^{-4} Hz makes thorium a possible reference for an optical clock with very high accuracy. This clock would be highly immune to systematic frequency shifts and broadening effects could be effectively eliminated using techniques of trapping and cooling [20].

A nuclear frequency standard opens a new possibility for a laboratory search for the variation of the fundamental constants [20]. The possibility of spatial and temporal variation of physical "constants" in the Universe is suggested by theories unifying gravity and other interactions [48]. A very sensitive method to study

the variation for the fine structure constant α in a laboratory [49] consists of the comparison of different optical atomic clocks [50, 51].

Comparing the ^{229}Th nuclear frequency to present atomic clocks will allow to search for variations of the fine structure constant but with an additional important advantage. The relative effects of the variation of α and $\frac{m_q}{\Lambda_{QCD}}$ with the quark mass m_q and the quantum chromodynamics mass scale Λ_{QCD} are magnified by an enhancement factor [52]. A rough estimate for the relative variation of the ^{229}Th transition frequency ω is

$$\frac{\partial\omega}{\omega} \approx 10^5 \left(0.1\frac{\partial\alpha}{\alpha} + \frac{\partial X_q}{X_q}\right) , \tag{2.10}$$

where $X_q = \frac{m_q}{\Lambda_{QCD}}$ [53], giving thorium the potential of improving the sensitivity to temporal variations of fundamental constants by many orders of magnitude. Depending on the applied nuclear model, the sensitivity of a temporal drift of the fine structure constant is estimated to be enhanced by 2–4 orders of magnitude [32, 33, 54].

Current atomic clock limits on the variation of the fundamental constants are approaching 10^{-17} per year. Using the nuclear thorium clock for comparisons with atomic clocks, the sensitivity to the variation of the fundamental constants can be enhanced to more than 10^{-20} per year.

2.2 Search for the Isomeric State Transition

Reich and Helmer were the first to suggest that ^{229}Th had a uniquely low-lying excited state close to the ground state in 1976 [23]. They measured differences in intra- and interband γ-ray-radiation of states populated in the α-decay of ^{233}U based on measurements of the rotational–band structure [23, 55]. The isomeric state had been identified as the band head of a $\Omega^\pi[Nn_z\Lambda] = \frac{3}{2}^+[631]$ band that is populated from higher excited states as well as the ground state of ^{229}Th in a $\frac{5}{2}^+[633]$ band.

In order to identify the isomeric state in an indirect detection, they examined the decay of excited 97.1 keV and 148.1 keV states [56]. These states have different channels to decay which end in the ground state and the isomeric state respectively, emitting multiple γ-rays in the keV range in this process. Despite the limited resolution of transitions five orders of magnitude higher than the state of interest, they managed to derive the first value of the isomeric state: E(^{229m}Th)= -0.001 $\pm$ 0.004 keV. This interval still included zero.

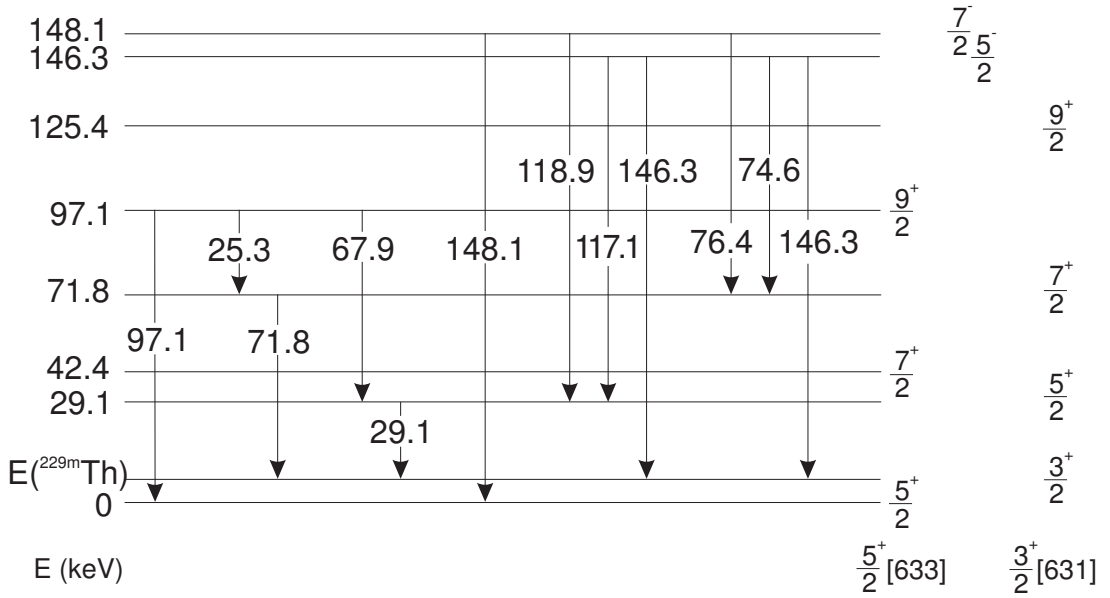

Figure 2.8: γ-rays taken into account to calculate the energy of the isomeric state of ^{229}Th [16, 56]

Remeasuring the energy of a number of γ-rays in 1994 [16], enhancing the resolution by increasing the number of detectors, reference lines and measurement runs, it was possible to improve this first measurement of the isomeric state. Using

$$\begin{aligned} E(^{229\mathrm{m}}\mathrm{Th}) &= (97.1 - 25.3 - 71.8)\,\mathrm{keV} \\ &= (97.1 - 67.9 - 29.1)\,\mathrm{keV} \\ &= (148.1 - 118.9 + 117.1 - 146.3)\,\mathrm{keV} \\ &= (148.1 - 76.4 + 74.6 - 146.3)\,\mathrm{keV}, \end{aligned}$$

as shown in figure 2.8, it was finally possible to identify the isomeric state and to obtain a result that surely excluded zero:

$$E(^{229\mathrm{m}}\mathrm{Th}) = 3.5 \pm 1.0\,\mathrm{eV}. \tag{2.11}$$

This energy corresponds to a wavelength of 350^{+150}_{-75} nm, the lifetime calculated from the estimated transition probability [57] was about 45 hours. Taken the uncertainty of ± 1.0 eV into account this lifetime could vary between $\sim$20 and $\sim$120 hours. The authors admitted that this was almost certainly not the actual half-life of this level, which would instead be determined primarily by the interaction of the electronic structure with the nucleus. First corrections of the lifetime were made in 1998 by theoretical considerations [25], reducing this value to 2–4 hours. Several experimental groups have performed further measurements

of the lifetime of the isomeric state, yielding inconclusive results varying from a few minutes [58] to several hours [59].

The task to observe the decay of the isomeric state was addressed by different groups [21, 60–63] using spectrometry on solid and dissolved ^{233}U samples: They obtained negative results or identified observed ultraviolet photons as α-induced fluorescence of nitrogen molecules [21, 64]. Several theoretical studies have been motivated by the discovery of the low-lying isomeric state of ^{229}Th and the new prospects arising from this approach to a new borderland between atomic and nuclear physics [13], highlighting various topics ranging from production and detection methods [36,40], effects on the α-decay of ^{229}Th [35], nuclear spin-mixing [65], influence of different environments [37] to internal conversion [66] and electronic bridge processes [67,68].

Although no experiment in search for direct observation succeeded, it took until 2005 for the value of E(^{229m}Th) = 3.5 ± 1.0 eV to be revised [69]. Based on newly investigated branching ratios [31,70], differing from the assumption that the excited 29.1 keV and 71.8 keV states decay directly to the isomeric state (see figure 2.8 [16]), the evaluation was extended by including more experimental data and new values of standard γ-energies [71]. Adopting the statistically most acceptable assumption regarding the decay pattern of ^{229}Th, the energy value was shifted to E(^{229m}Th) = 5.5 ± 1.0 eV.

In 2007, a measurement by Beck et al. [72] used a novel NASA x–ray microcalorimeter spectrometer with an energy resolution of only 26 eV (FWHM) to obtain the most accurate value for the isomeric state to date. The 71.82 keV state populated in the α-decay of ^{233}U decays with closely spaced γ-ray doublets to the ground state and the isomeric state respectively (see figure 2.9) that could be resolved with high accuracy.

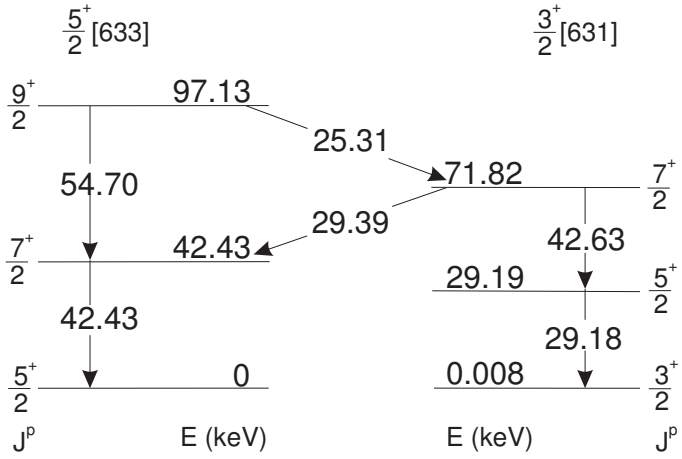

Figure 2.9: Partial level scheme and γ-rays of ^{229}Th [17]

Starting from this 71.82 keV state, the isomeric state is populated via intraband transition of γ-rays with an energy of 42.63 and 29.18 keV whereas the ground state is fed via an interband γ-ray of 29.39 keV to the 42.43 keV state followed by an intraband 42.43 keV transition. Using the relation

$$71.82\,\mathrm{keV} = 29.39 + 42.43\,\mathrm{keV} = 42.63 + 29.18 + E(^{229\mathrm{m}}\mathrm{Th})\ , \tag{2.12}$$

the energy of the isomeric state is found to be

$$E(^{229\mathrm{m}}\mathrm{Th}) = (29.39 - 29.18\,\mathrm{keV}) - (42.63 - 42.63\,\mathrm{keV})\ . \tag{2.13}$$

The energy differences of each doublet are about 200 eV. The Ge detectors used by Helmer and Reich [16] could not resolve these doublets and had to rely on energy differences at least one order of magnitude larger than 200 eV while the HgTe spectrometer used in this experiment could resolve these lines.

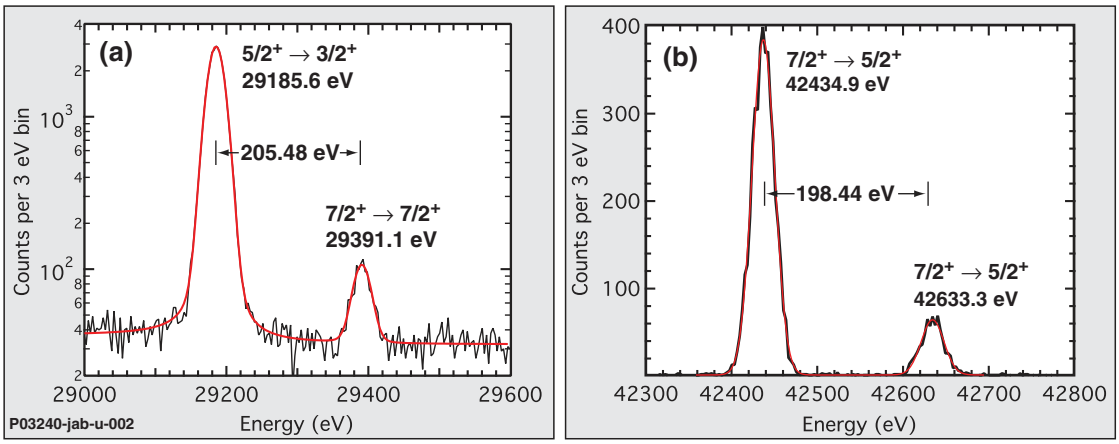

Figure 2.10: Spectra in the 29 and 42 keV regions [17] used to measure the γ-ray doublets (2.13). Black lines represent the data, red lines represent the least-square fitting results.

Finally, a correction had to be implemented in the measured difference in figure 2.10. The unobserved but expected interband branching of the 29.19 keV state to the ground state had to be taken into account which could be estimated accurately from the interband branching ratio of the 71.82 keV level. Using this estimation to add a positive correction of 0.6 eV to the measurement, one obtains

$$E(^{229\mathrm{m}}\mathrm{Th}) = 7.6 \pm 0.5\,\mathrm{eV}. \tag{2.14}$$

Even though this measurement was still an indirect observation of $^{229\mathrm{m}}$Th and the direct observation has still to be done, this value for $E(^{229\mathrm{m}}\mathrm{Th})$ is widely accepted due to the quality of the data. It also explains why all prior observations

had been unsuccessful, since the detectors used in these searches had no sensitivity at 7.6 eV, and clears the way for new methods and experiments in search for a direct observation of the transition between the isomeric state and the ground state of ^{229}Th.

2.2.1 Thorium in a Hydrochloric Acid

First experiments with ^{229}Th were conducted in PTB assuming that the energy of the isomeric state is $E(^{229m}\mathrm{Th}) = 3.5 \pm 1.0$ eV. Since aqueous thorium solutions are transparent in this spectral region, an experiment with 10 kBq of thorium chloride in a 0.1 molar hydrochloric acid was set up. The excitation of the isomeric state ought to be achieved with a high pressure mercury-xenon lamp with a strong light emission in a spectral range around 350 nm.

Multiple aspects had to be taken into account when choosing the type of solution for spectroscopy experiments. While water and hydrochloric acid are transparent at 350 nm, nitric acid is opaque at this wavelength. The ^{229}Th solution available at PTB was a solution of $\mathrm{Th(NO_3)_4}$ and would therefore not be transparent for the spectral region of interest. Additionally, to prevent adsorption of thorium on the windows of the cell, the solution needs to be acidic. To account for these conditions, an ion exchange had been conducted to prepare a one molar hydrochloric thorium solution.

The material of the cell should fulfill different requirements and was hard to determine. Demands for mechanical and chemical stability constrained the choice of material to polymers. Additionally, the polymer has to be luminescence-free to avoid background effects. Most of the tested materials showed long-lasting luminescence effects [73] and only carbon fibre filled PEEK (polyether ether ketone) proved to be insensible for luminescence induced by the mercury-xenon lamp.

Earlier experiments revealed a strong long-lasting luminescence from fused silica windows after irradiation with the mercury-xenon lamp as shown in figure 2.12a. To avoid background radiation from cell windows overlapping the expected signal from the decay of ^{229m}Th in the hydrochloric acid, a double-chambered cell was designed as shown in figure 2.11. The irradiation and detection chambers were equipped with fused silica windows[2] and connected with a channel in the PEEK.

The thorium solution was irradiated in one half of the cell with a light power of 1–2 Watts for about an hour. Afterwards, the solution was decanted from the irradiation chamber to the detection chamber, thus being in a cell that was not illuminated by the lamp. The cell was placed in darkness with an optical setup that focussed the photons emitted from the cell on a photomultiplier. Fused silica filter glasses with different transmission ranges were installed in front of the photomultiplier.

[2] Schott Lithotec Q1-E248

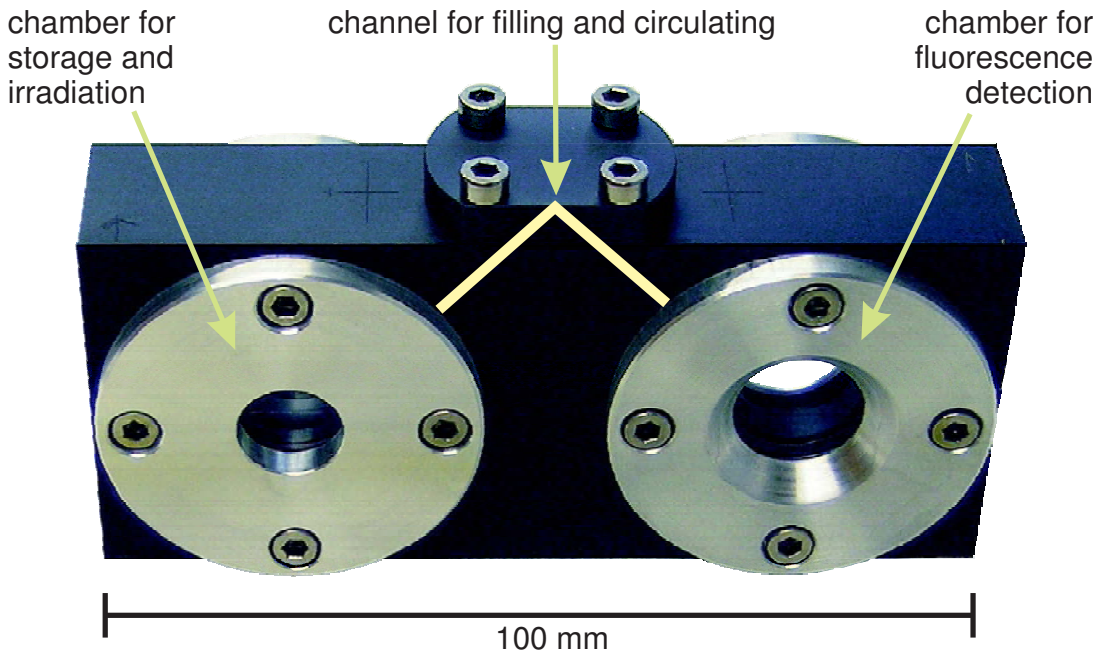

Figure 2.11: The double-chambered PEEK cell used to conduct experiments with a hydrochloric thorium solution.

The results for these measurements are plotted in figure 2.12b. It can be seen that the signal increases in the beginning of the measurement before settling on a constant count rate after about 2–4 hours. The reason for this signal increase is found in small particles of fibrous material forming in the cell a couple of months after filling in the thorium solution. When the solution is decanted from one chamber to the other side, these particle disperse uniformly in the solution and block photons coming from the detection cell. These particles need 2–4 hours for sedimentation and explain the signal rise during this time.

The high count rate of about 700 photons per second is not a result of the irradiation with the mercury-xenon lamp. Measurements with the cell stored in darkness for a week showed the same count rate as the measurements in figure 2.12b, revealing the detected signal to be pure background from the cell.

The high background in the measurements is caused by Cherenkov radiation [74] induced from β-particles in the hydrochloric acid. The path length of about 1 cm of these β-particles lead to the production of multiple photons in the acid. Anyway, after discovering the new value for the isomeric state of $E(^{229\mathrm{m}}\mathrm{Th}) = 7.6 \pm 0.5$ it was clear that no signal could have been seen due to the absorption of occurring photons by the water in the hydrochloric acid.

The recoil experiment described in chapter 3 was designed to overcome the restrictions of providing a resonant broadband light source and allowed to study

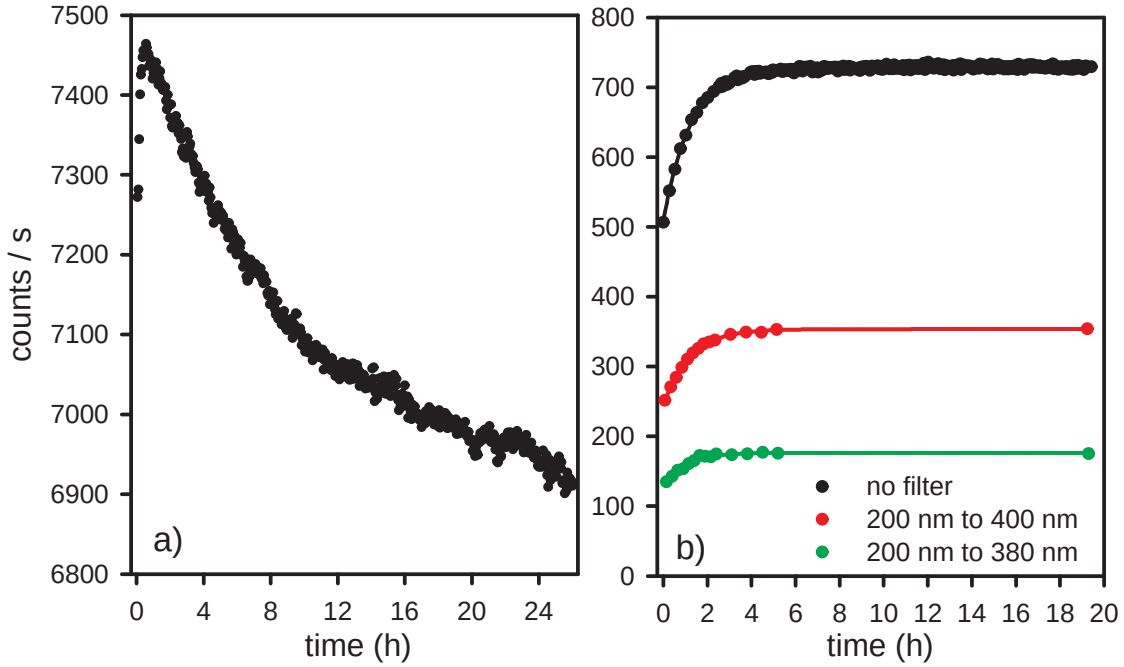

Figure 2.12: a) Signal of a fused silica cell containing 100 kBq of ^{229}Th in a neutral ThCl solution irradiated by a high pressure mercury-xenon lamp. The long-lasting luminescence of the fused silica windows decreases with time to the Cherenkov-induced background of 6900 counts/s. b) Measurements of a 10 kBq hydrochloric ^{229}Th solution with and without reducing the sensitive spectral range with filter glasses in the double-chambered cell.

^{229m}Th in different solid environments. This experiment was free from the absorption of photons in a liquid as well as the production of Cherenkov radiation caused by embedding thorium nuclei in a bulk material or solution. However, Cherenkov radiation has to be taken into account as seen in section 3.2.1 even when handling small samples of ^{229m}Th.

3 Thorium Recoil Nuclei

One of the biggest obstacles of all efforts to observe the photon emitted directly from the nucleus is the fact that prior to observation, the nucleus has to be in the excited state. Since the cross-section of the photon-nucleus interaction as well as the linewidth of the excited state are extremely small, it is very difficult to excite the isomeric state with a broadband illumination. The value of $E(^{229\mathrm{m}}\mathrm{Th}) = 7.6 \pm 0.5\,\mathrm{eV}$ additionally enforces an oxygen free atmosphere for the transmission of the radiation.

The problem of exciting the isomeric state can be avoided if ^{229}Th can already be obtained in the isomeric state. Following the α-decay of ^{233}U, about 2% of the created nuclei are in the isomeric state [70] and will decay to the ^{229}Th ground state under the emission of a 7.6 eV photon if no competing radiationless processes are available. The long sought 7.6 eV photons should be part of the γ-rays emitted in the ^{233}U decay chain, the experimental challenge, however lies in detecting them in the presence of strong α- and β-induced background. Using the α-recoil energy, thorium nuclei can be emitted from a thin uranium source and subsequently implanted into a thin absorber. If this absorber is transparent in the vacuum ultraviolet (VUV), it can be used to observe the photons emitted from the decay of the isomeric state.

This approach evades the excitation of the isomeric state and produces a thorium sample exempt from ^{233}U background at the same time. While other experiments obtaining a sample of freshly produced $^{229\mathrm{m}}$Th from the ^{233}U decay rely on chemical separation methods [63, 75] to clear the uranium, which takes at least 30 min to accomplish, our method allowed to measure 30 s after the absorber was removed from the recoil chamber. The short time span between production and detection of $^{229\mathrm{m}}$Th may grant access to the observation of processes with lifetimes of a few minutes.

3.1 Production and Detection of Recoil Nuclei

The experiment with "fresh" $^{229\mathrm{m}}$Th from a uranium source is executed in two steps as indicated in figure 3.1. The first step is to implant thorium in an absorber. The second step is to remove the absorber from the uranium and place it in front of a photomultiplier to detect the photons emitted from the nuclei. Since the lifetime of the isomeric state depends on the electronic environment of the $^{229\mathrm{m}}$Th nuclei

(see 2.1.4), these two steps should be repeated with different absorber materials such as fused silica and various polymers.

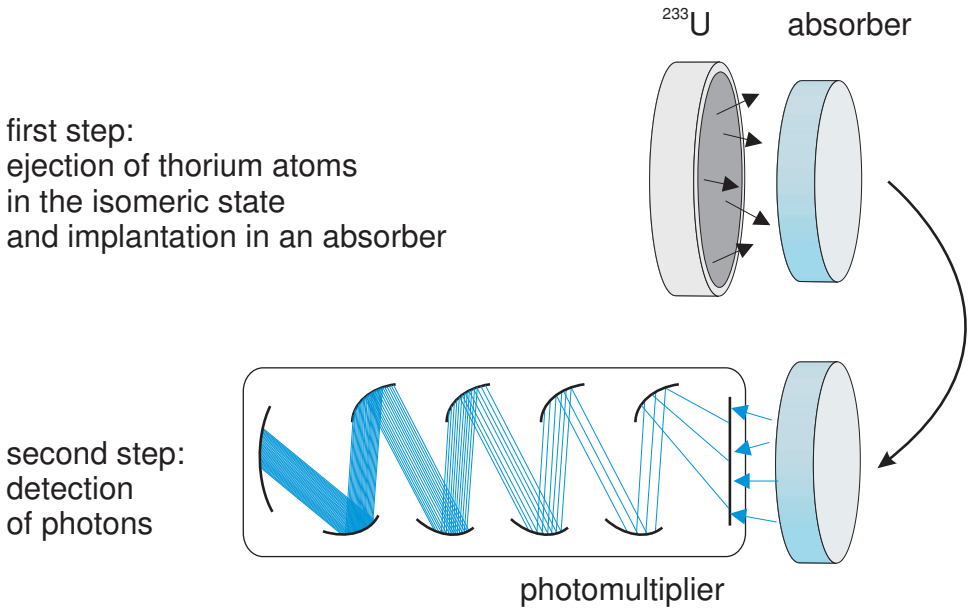

Figure 3.1: Scheme of recoil experiment procedure.

The α-decay of ^{233}U creates α-particles in the range of 5 MeV where the most prominent decay channel emits an α-particle with an energy of 4.91 MeV [76]. Using the law of conservation of linear momentum, the recoil energy is deduced from

$$E_r = \frac{1}{2} m_r v_r^2 = \frac{1}{2} m_\alpha v_\alpha^2 \cdot \frac{m_r}{m_\alpha} \cdot \left(\frac{v_r}{v_\alpha}\right)^2 = E_\alpha \cdot \frac{m_r}{m_\alpha} \cdot \left(\frac{m_\alpha}{m_r}\right)^2 = E_\alpha \cdot \frac{m_\alpha}{m_r} \ , \qquad (3.1)$$

where E_r and E_α denote the energies of the recoil nucleus and the α-particle, m_r, m_α are the masses and v_r, v_α the velocities, respectively. Thus one calculates the recoil energy of the ^{229}Th recoil particle to

$$4.91\,\mathrm{MeV} \cdot \frac{4\,\mathrm{u}}{229\,\mathrm{u}} = 85.76\,\mathrm{keV} \ . \qquad (3.2)$$

If the thorium particles are supposed to be ejected from the uranium layer where they are created, the layer has to be thinner than the range of thorium particles in uranium. The range of the particles can be calculated from the stopping power, which is the average energy loss of the particle per unit path length. In the process, the ionization of the atoms or molecules which the particles encounter on their

path through the material causes a subsequent loss of energy in many small steps. Stopping powers are widely tabulated (e.g. [77]) or can be calculated for different elements in a large number of environments with computer programs [78] and the range $R_U(^{229}\mathrm{Th})$ of thorium recoil particles in uranium is calculated [78] to

$$R_U(^{229}\mathrm{Th}) \approx 11\,\mathrm{nm}\ . \tag{3.3}$$

When a thorium particle is created within a 11 nm thick surface layer, it may be ejected from the uranium into the free space. Since the angular distribution for the α-emission is random, the probability for ejecting a thorium recoil particle increases the closer the point of origin is to the surface. The free path length for a thorium particle in air at normal pressure with the energy according to (3.2) is about $R_{air}(^{229}\mathrm{Th}) \approx 69\mu\mathrm{m}$ [78]. To extend this free path length and allow the thorium to reach an absorber, the thorium transfer ought to be done in vacuum. Since the free path scales reciprocal with pressure, evacuating the environmental pressure to 100 Pa enhances the free path length to

$$R_{air,100\,\mathrm{Pa}}(^{229}\mathrm{Th}) \approx 69\,\mathrm{mm}\ . \tag{3.4}$$

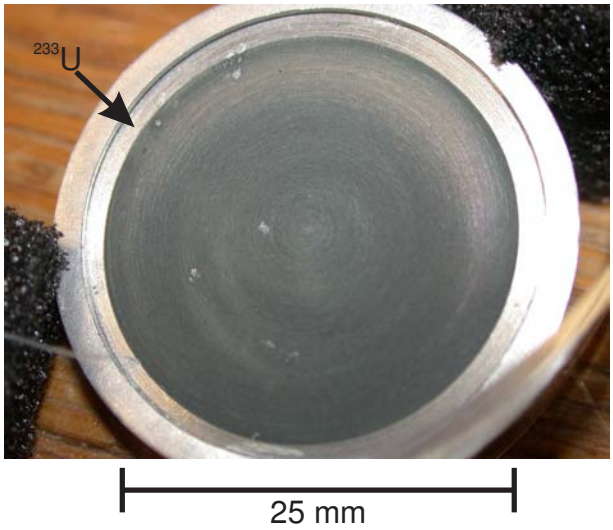

Figure 3.2: Uranium source used to produce $^{229\mathrm{m}}$Th recoil atoms.

To estimate the amount of thorium recoil particles implanted in the absorber, the diameter of the active area is assumed to be 25 mm with respect to the conditions of the experiment. Using (3.3), the volume that has the ability to eject thorium recoil particles is $5.4 \cdot 10^{-12}\,\mathrm{m}^3$. With the uranium density of 18950 $\frac{\mathrm{kg}}{\mathrm{m}^3}$, a mass of 102.3 μg is calculated and the ^{233}U activity is deduced with the half-life of $1.592 \cdot 10^5$ years to

$$A_U = 36508\,\mathrm{Bq} \approx 36\,\mathrm{kBq}\ . \tag{3.5}$$

The absorbers were placed ≈ 3 mm in front of the uranium to assure all ejected ions reach the absorber (compare (3.4)). Since the direction of the ejected α-particle and hence of the recoil particle is random, a maximum of 50% of the produced thorium particles are ejected in the direction of the absorber, assuming the uranium layer is negligible thin. Hence about 18000 thorium atoms per seconds are supposed to be implanted in the absorber. Assuming 2% of these thorium atoms are in the isomeric state, 360 ^{229m}Th atoms can be expected to be accumulated per second.

The uranium used in the experiment was electroplated on a stainless steel disc[1] with an active area of 25 mm diameter as seen in figure 3.2. The activity was 48 kBq and therefore higher than the necessary activity for the maximum ejection efficiency in (3.5) for metallic uranium.

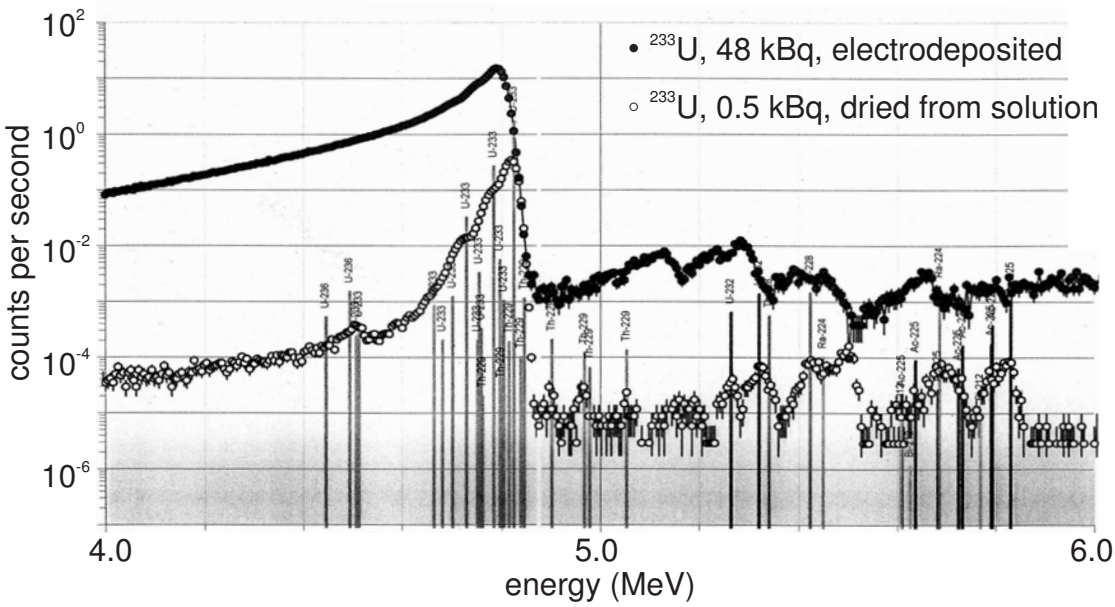

Figure 3.3: α-spectrum of electrodeposited ^{233}U used in the recoil experiments and of a reference ^{233}U source dried on a silicon disk, measured in a grid ionization chamber.

Measurements of the α-particle energies from this uranium in a grid ionization chamber from the radioactivity department of the PTB[2] revealed the energy distribution in figure 3.3. The α-particles loose energy when travelling through solid material, depending on the path length and the stopping power in this material. The projected range of an α-particle in uranium with an energy of 4.9 MeV is

[1] purchased from Eckert & Ziegler Isotope Products Europe GmbH

[2] D. Arnold, M. Ehlers and H. Janßen, Physikalisch-Technische Bundesanstalt, Working group Unit of Activity

8 μm. If the 48 kBq ^{233}U source was metallic uranium, it would have a thickness of 14.5 nm and produced a sharp peak in figure 3.3 due to the projected range of the α-particle being 3 orders of magnitude higher than the ^{233}U thickness. However, according to our α-energy measurement, the lost energy corresponds to a 100 times longer path length through solid material. This leads to the conclusion that the layer is not metallic uranium but heavily soiled with materials used in the electroplating process.

Therefore, the 11 nm thick layer capable of emitting ^{229m}Th nuclei (see eq. (3.3)) only emits 1% of the calculated ^{229}Th flux of equation (3.5). Measurements of the thorium activity of a stainless steel absorber accumulating nuclei for 40 hours confirmed the result of a capture rate of only 1% of the produced thorium nuclei. Therefore, the number of accumulated thorium nuclei in the isomeric state is only 3-4 per second.

The accumulation chamber in figure 3.4 was evacuated by a membrane vane pump to a pressure of 100 Pa. The uranium was fixed in one half of the setup and stored constantly under vacuum. Different absorbers were glued to steel rings and magnetically fixed on the tip of a sliding vane. The vane was applied to the second half of the chamber and this half was evacuated. After opening the valve separating the uranium from the absorber, the absorber was moved towards the uranium and stopped in front of the uranium at a distance of 3 mm.

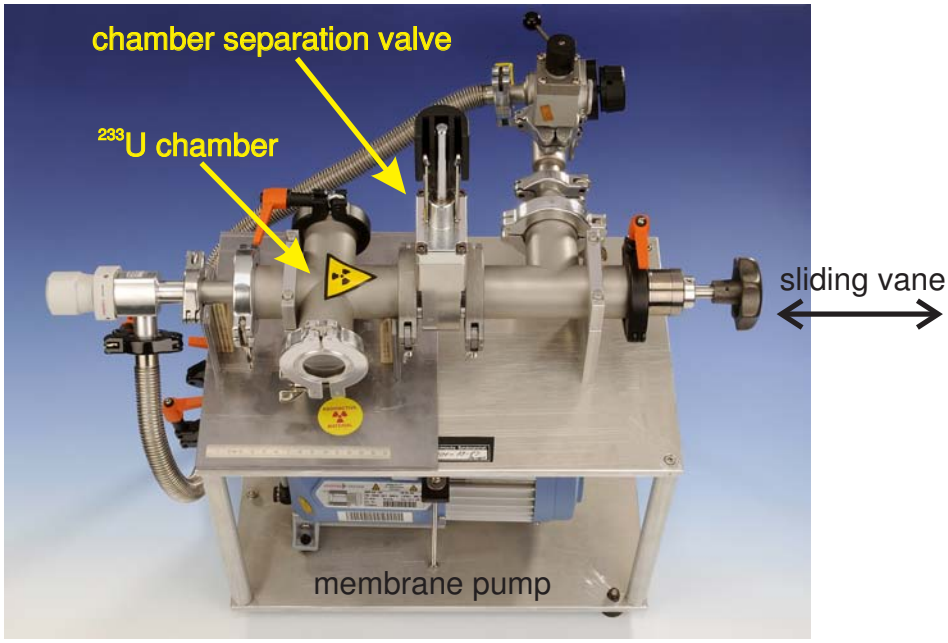

Figure 3.4: Uranium chamber for accumulating thorium recoil particles. The sliding vane is slid in to place the absorber in front of the uranium.

After accumulating thorium ions for several hours, the absorber is removed from the uranium chamber and placed in front of a photomultiplier. The necessary accumulating time depends on the lifetime of the isomeric state which is several orders of magnitude shorter than the lifetime of ^{233}U. This difference in lifetimes soon leads to an equilibrium between the production of ^{229m}Th from ^{233}U and the decay of the isomeric state to the ground state. Therefore it is not necessary to accumulate thorium nuclei for times much longer than the lifetime of the isomeric state [79]. Since the lifetime is not known but is assumed to be in the range of 2–4 h, accumulation times for thorium particles of at least 4 h are generally used.

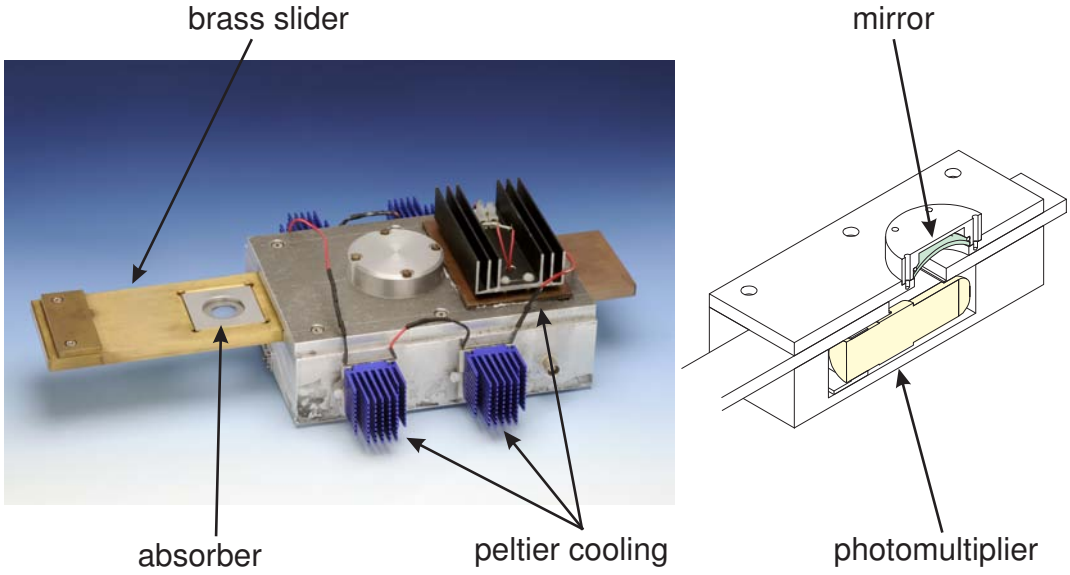

Figure 3.5: Detection box for photons from thorium accumulated on an absorber. Left: photo of the chamber, absorber placed in brass slider. Right: Cut through the detection box, showing the positions of the photomultiplier and the parabolic mirror.

The first used photomultiplier[3] was sensitive for photons in the range of 2–6 eV (since the experiment was started under the assumption of detecting a 3.5 ± 1 eV photon) and was later replaced by a photomultiplier[4] sensitive for 4–10 eV photons. They were mounted in a light-tight aluminum vessel facing a parabolic mirror focussed on the active area (see figure 3.5) of the photomultiplier. The aluminum chamber was cooled with Peltier elements to 13 °C to minimize the dark counts of the photomultiplier to 1–2 counts per second. The absorber was placed in a brass

[3]Hamamatsu R4220P, sensitivity 185 nm to 710 nm, quantum efficiency 25% at 350 nm, active area 8 mm · 24 mm, side-on version, selected for photon counting

[4]Hamamatsu R8486P, sensitivity 115 nm to 320 nm, quantum efficiency 35% at 220 nm, active area 8 mm · 12 mm, side-on version, selected for photon counting

slider that allowed insertion of the absorber in the vessel without illuminating the photomultiplier with ambient light during this process. When pulling in the slider, the absorber was positioned between the photomultiplier and the mirror with the thorium accumulated side 2 mm in front of the active area .

To ensure an oxygen-free atmosphere for the measurements of photons with a wavelength shorter than 180 nm where oxygen would absorb these photons, the aluminum vessel was purged with nitrogen. Prior to the insertion of the ^{229m}Th absorber, a nitrogen flux of 5 l/s was maintained for several minutes, the nitrogen inlet being at the bottom of the vessel and releasing the purged nitrogen through the isolating material of the brass slider. When the vessel was completely filled with nitrogen, the experiment was started and the nitrogen flux was lowered to 0.5 l/s to maintain the nitrogen concentration in the vessel.

The absorber material was glued on a steel ring with ultraviolet hardening glue and the glue was selected with respect to low luminescence background effects. Due to this fastening method, the setup allowed testing of different absorber materials. Tested were borosilicate glass (thickness 0.5 mm), fused silica (thickness 1 mm), CaF_2 (calcium fluoride, thickness 2 mm), PVDF (polyvinylidene fluoride, thickness 50 μm) and PET (polyethylene terephthalate, thicknesses 6 μm and 0.7 μm). The polymer absorbers were selected with respect to their small thickness to minimize luminescence effects from α-particle induced luminescence.

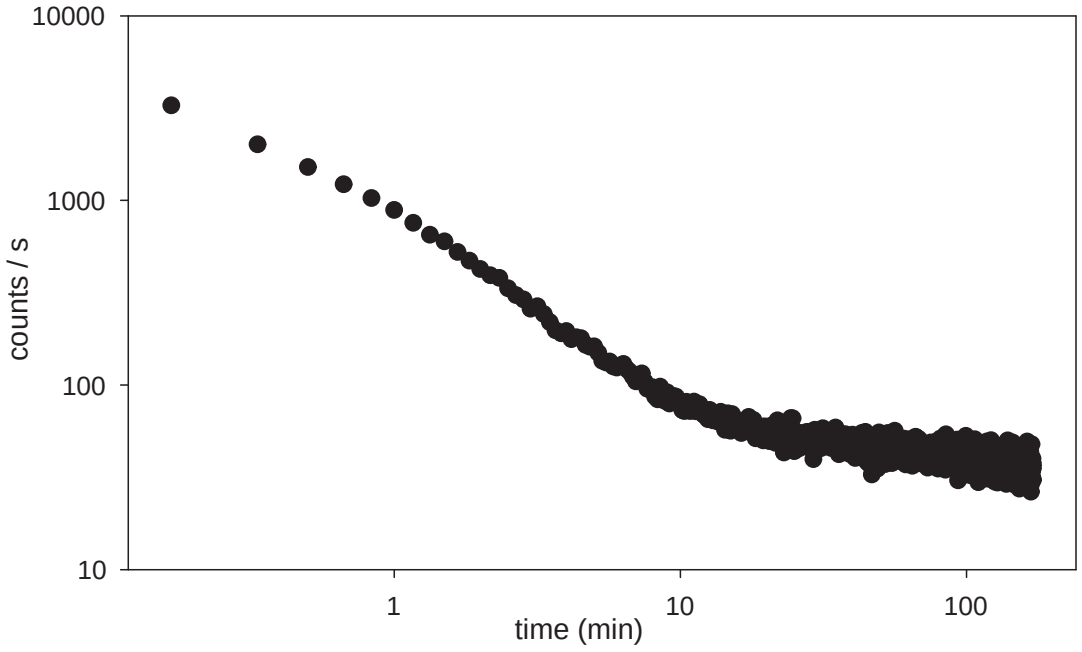

Figure 3.6: Long-lasting photoluminescence signal of a CaF_2 absorber after irradiating the absorber with a 30 W deuterium lamp.

It has been shown in previous experiments [73] that several polymers show long-lasting photoluminescence effects after irradiation with ultraviolet light. In the first test runs, this has been shown for fused silica and CaF_2 and is depicted for CaF_2 in figure 3.6. Hence the absorber transfer from the uranium chamber to the detection box was done in a room only lit with a photographic laboratory light emitting in the red spectrum, reducing the background signals significantly.

3.2 Temporal Decay Curves

Despite the low photomultiplier dark count rate of 1–2 counts per second, background effects from the absorber are the biggest obstacle for the evaluation of the measured luminescence signals. This has been partially accounted for by choosing thin absorbers and avoiding exposure of the absorbers to ultraviolet light. Depending on the half-life of the isomeric state, a capture rate of 3–4 ^{229m}Th nuclei per second from the uranium source could still be observed if the background is low enough.

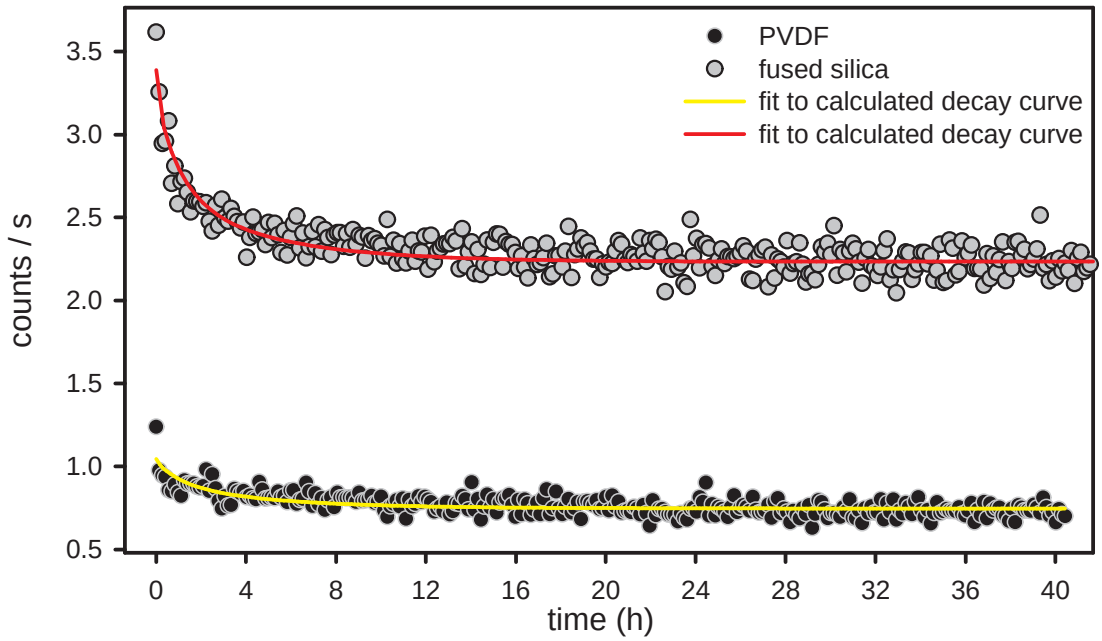

Figure 3.7: Luminescence signal of PVDF (thickness 50 μm) and fused silica (thickness 1 mm) absorbers accumulating thorium nuclei for 7.5 hours. The fitted curves correspond to a signal in the photomultiplier (sensitivity 185 nm to 710 nm) produced by 0.1% of the α- and 0.3% of the β-particles for PVDF and 0.8% of the α- and 0.9% of the β-particles for fused silica, respectively.

Results from the early phase of the experiment with a photomultiplier sensitive from 185 nm to 710 nm are shown in figure 3.7, where every data point represents the average over 100 s. The background in the fused silica absorber is three times higher than in the PVDF absorber, probably due to α- and β-induced luminescence.

Since the photomultiplier that was used in this experiment was not sensitive for the $^{229\mathrm{m}}$Th photon wavelength of 163^{+11}_{-10} nm, the decay curves need to be explained in the next section.

3.2.1 Radioactive Decay Chain Background

All decay signals showed the same nearly exponential behavior right after exposure. To examine the origin of this decay, the whole decay chain of ^{233}U has to be taken into account.

To deduce the amount of all decay products and their α- and β-particle emission, a set of equations has to be solved. The decay of one single radioactive element is described by an easily solved differential equation

$$\frac{dN}{dt} = -\lambda N(t) \ , \qquad N(t=0) = N_0 \ , \qquad N(t) = N_0 \, e^{-\lambda t} \ , \tag{3.6}$$

where N denotes the number atoms in the nuclear parent and λ is the time constant. The activity A is the number of decaying atoms per time

$$A(t) = -\frac{dN}{dt} = \lambda \, N(t) = \lambda \, N_0 \, e^{-\lambda t} = A_0 \, e^{-\lambda t}. \tag{3.7}$$

While this is easily solved for a single element, it becomes computationally intensive for more elements in this decay chain, because the produced daughter element decays itself but is fed by the nuclear parent. In order to obtain the complete decay chain from ^{233}U to ^{209}Bi (which has a half-life of 10^{19} years and can be considered stable), a set of 10 coupled first-order linear differential equations has to be solved. These equations are called Bateman equations [80] in the form

$$\frac{dN_n}{dt} = -\lambda_n N_n(t) + \lambda_{n-1} N_{n-1}(t) \ , \qquad n = 1, 2, \ldots, 10 \tag{3.8}$$

and have the general solution

$$N_n(t) = c_1 e^{-\lambda_1 t} + c_2 e^{-\lambda_2 t} + \ldots + c_n e^{-\lambda_n t} \tag{3.9}$$

with

$$
\begin{aligned}
c_1 &= \frac{\lambda_1\lambda_2\cdots\lambda_{n-1}}{(\lambda_2-\lambda_1)(\lambda_3-\lambda_1)\cdots(\lambda_n-\lambda_1)}N_{10} \\
c_2 &= \frac{\lambda_1\lambda_2\cdots\lambda_{n-1}}{(\lambda_1-\lambda_2)(\lambda_3-\lambda_2)\cdots(\lambda_n-\lambda_2)}N_{20} \\
&\vdots \\
c_n &= \frac{\lambda_1\lambda_2\cdots\lambda_{n-1}}{(\lambda_1-\lambda_n)(\lambda_2-\lambda_n)\cdots(\lambda_{n-1}-\lambda_n)}N_{n0}\ .
\end{aligned}
\tag{3.10}
$$

This general solution can be adapted to the ^{233}U recoil system. The activities of all elements in the uranium is calculated from the age of the source, which was 3 years at the delivery date. Starting from this compound, not only thorium recoil nuclei are captured by the absorber but all nuclei produced from α-emitters present in the uranium source. Since ^{233}U has the lowest α-energy in the neptunium chain (see section 2.1.2) and all other elements existing in the uranium source are lighter than uranium, the probability of their ejection is at least as high as the probability of ejecting thorium nuclei.

Hence the absorber contains a mixture of α- and β-emitters with half-lifes between 4.2 ms (for ^{213}Po) and 14.9 days (for ^{225}Ra) which are at least five orders of magnitude shorter than the lifetime of ^{229}Th, creating a much higher α- and β-flux than an absorber with thorium alone.

The amount of absorbed elements can be calculated with respect to their half-lifes and time in front of the uranium, taking into account the decay of the already absorbed nuclei. The calculated activities of the α- and β-emitters are plotted in figure 3.8.

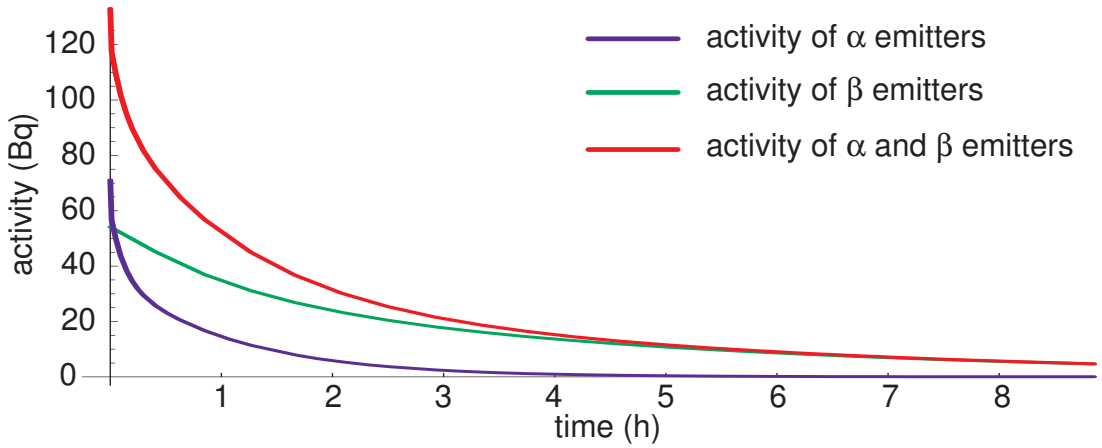

Figure 3.8: Calculated α- and β-emitter activities for an absorber accumulating recoil nuclei for 195 min.

Using the results of the calculated α- and β-activities, a fit to the obtained data can be applied. The fit makes use of the intensity distribution and lifetimes of the calculated α- and β-emission and only adapts the percentage of emitted particles creating a signal in the photomultiplier. The luminescence signal in figure 3.7 can be explained with less than 1% of the α- and β-particles producing a signal in the photomultiplier.

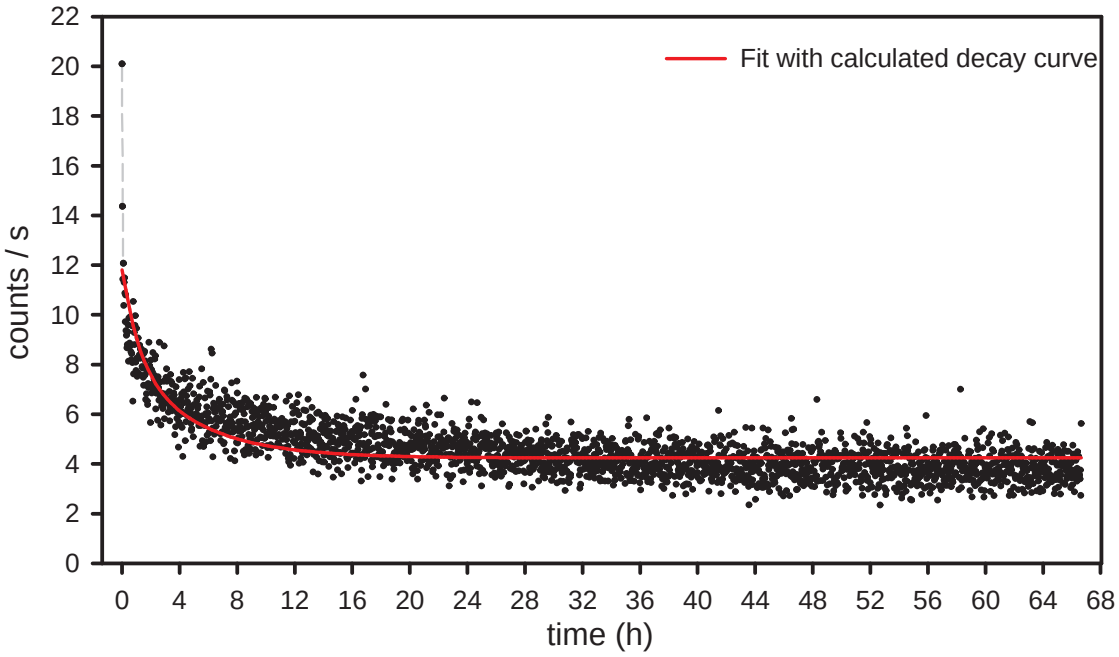

Figure 3.9: Signal from a CaF_2 absorber (thickness 2 mm) and fit with calculated decay curve where 14% of the emitted β-particles produce a signal count in the photomultiplier (sensitivity: 115 nm to 320). Every point represents an average over 100 s.

When using the photomultiplier sensitive for the ^{229m}Th decay as in the CaF_2 absorber signal in figure 3.9, a photon detection probability of 14% for every emitted β-particle is sufficient to fit the observed signal. The CaF_2 was the thickest absorber used in the experiments with a thickness of 2 mm and created a higher background than other samples. Measurements with PVDF in figure 3.10 indicated a much smaller background and signal count rate but had the same qualitative result; the signal can be fitted with β-induced fluorescence.

The difference in count rate between the PVDF and the CaF_2 sample is linked to the sample thickness, where CaF_2 is 40 times thicker than PVDF. The background as well as the signal of the measurements in figures 3.8 and 3.10 scale with this thickness.

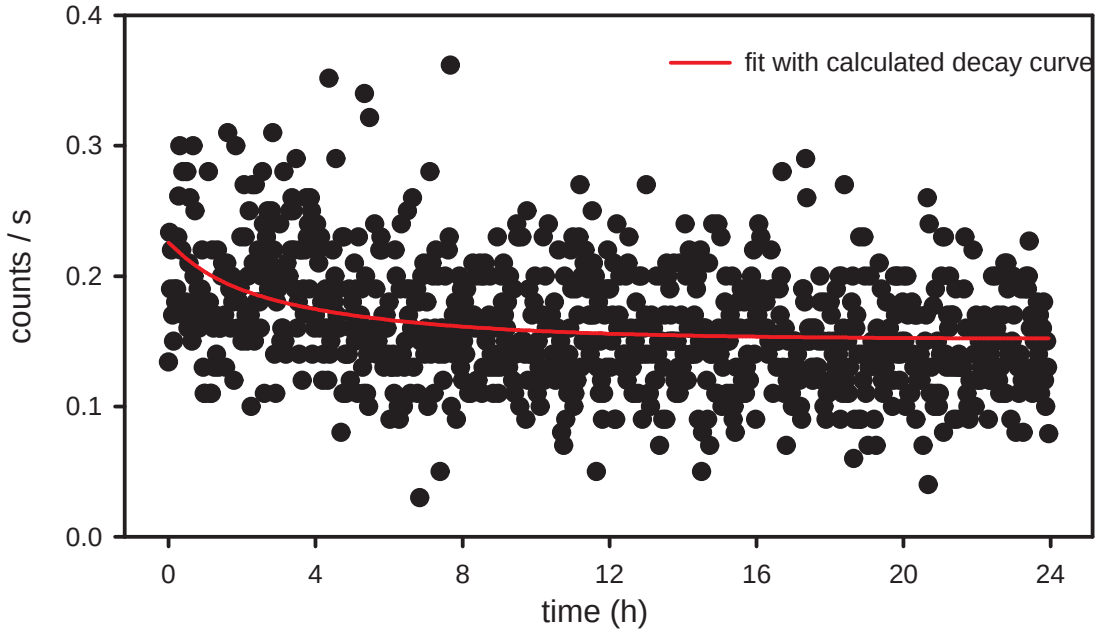

Figure 3.10: Signal of a PVDF absorber (100 s average), fit with 0.1% of the emitted β-particles producing a count in the photomultiplier (sensitivity: 115 nm to 320 nm)

This legitimates the assumption that the background is created in the absorber material by β-particles. The explanation for β-induced fluorescence is without much doubt Cherenkov radiation [74], since the energy of the electrons emitted by ^{213}Bi and ^{209}Pb is high enough to produce significant amounts of Cherenkov radiation in the absorber material.

The spectral energy density of Cherenkov radiation is proportional to $\frac{1}{\lambda^3}$ and the number of emitted photons is therefore proportional to $\frac{1}{\lambda^2}$. This explains the higher conversion rate of β-particles detected with the photomultiplier sensitive in the VUV region for CaF_2. Because fast electrons produced by β-decay can create more than 1 photon in a dense medium, the count rate is increased again with the thickness of the material [81].

However, the fit does not explain the fast decay in the first minutes in figure 3.9 completely. This slightly higher count rate in the first minutes of the absorbers placed in front of the photomultiplier sensitive in the VUV was the only difference to the signals recorded with the photomultiplier not sensitive at this wavelength. To reduce noise in the recorded signal, data point averaging over 100 seconds had to be applied, excluding the possibility of observing fast processes in more detail. Unfortunately, the quality of data does not allow to conclude the direct observation of photons emitted from the isomeric state.

The reason for the missing observation of ^{229m}Th decay photons is not clear. Multiple explanations are possible:

- Since the used uranium source was not a metallic uranium sample and therefore produced only a fraction of the possible thorium nuclei, it may lead to a small signal-to-noise ratio and could have produced an undetectable signal.
- Less than 2% of thorium nuclei may be in the isomeric state (contrary to [82]).
- The wavelength of the photons emitted from the decay of the isomeric state may be shorter than 130 nm and therefore the photomultiplier would not be sensitive for the photons.
- The coupling to the electronic environment of the absorbers or the uranium source may lead to a rapid nonradiative decay of the energy of the isomeric state to the solid.
- The lifetime of the isomeric state may not be in the range of the assumed 2–4 hours but rather in the range of minutes or shorter. A lifetime shorter than 30 seconds could not be detected due to the time needed to transfer the absorber from the uranium chamber to the detection vessel.

3.3 Spectral Analysis

A simpler approach to search for photons emitted from the isomeric state populated in the α-decay of ^{233}U to ^{229m}Th is to measure directly the photons emitted from a uranium source. Due to background radiation effects, spectral selection is necessary to distinguish the photons produced in the decay of the isomeric state. Earlier experiments [21, 60, 62] could not succeed in this task due to the wrong assumption of scanning for a 3.5 eV photon and thus using equipment not appropriate for the detection of a 7.6 eV photon.

A cooperation with the x-ray metrology department of the PTB[5] offered the oportunity to use a VUV-monochromator equipped with a Peltier cooled CCD camera with $1300 \cdot 1340$ pixels . Due to the permitted limit of 10 kBq for ^{233}U in the monochromator, a different uranium source than that in the recoil experiment had to be used. The α-spectrum in figure 3.3 revealed an unusual high contamination of the uranium layer with the solvent used in the electrodeposition process, therefore the new ^{233}U source was produced by drying a uranium solution onto a silicon disc with an activity of 10 kBq.

The acceptance of monochromator setting was $1.5 \cdot 10^{-3}$, the quantum efficiency of the CCD at 160 nm was about 20%. Therefore, the expected signal can be

[5] A. Gottwald and G. Ulm, Physikalisch-Technische Bundesanstalt, Working group UV and VUV Radiometry

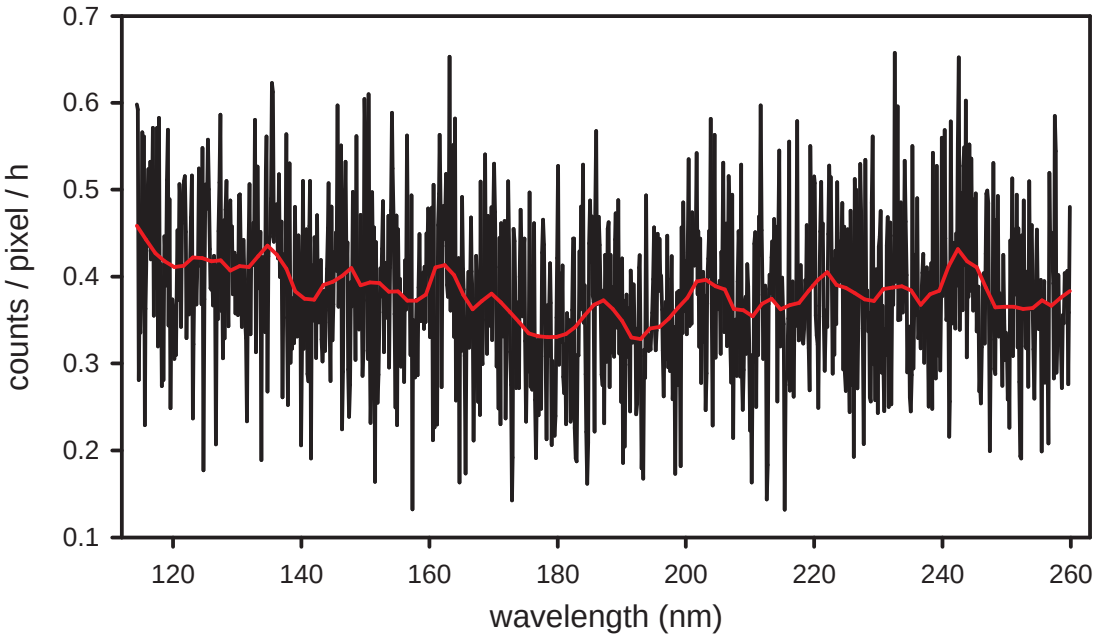

Figure 3.11: Complete average over all measurements, averaging for 500 hours. The observed signal was averaged over 1300 pixels per wavelength.

estimated with an activity of 10 kBq, 2% of the atoms in the isomeric state and emission into a half-space to

$$\text{Signal} = 10\,\text{kBq} \cdot 0.02 \cdot 0.5 \cdot 1.5 \cdot 10^{-3} \cdot 0.2 = 0.06\,\frac{\text{photons}}{\text{s}}\ . \tag{3.11}$$

The slit in front of the monochromator had a width of 2 mm, mapping the photon emission of the isomeric state on a width of 50 pixel of the CCD. The CCD height of 1300 pixel results in expected signal of 0.0033 photons/pixel/h. Long measurement and averaging times are necessary.

We recorded a signal for 500 hours with two different settings for the monochromator, both settings covering a range from 115 nm to 260 nm. Unfortunately, the background noise from the CCD was two orders of magnitude higher than expected, making it impossible to distinguish a signal. The slightly higher count rate in figure 3.11 at 160 nm is well within the statistical uncertainty and does not allow to reasonably conclude a verification of the photons emitted by the decay of the isomeric state.

4 Laser Ablation Ion Production

Thorium has one of the highest known boiling points at 4788 °C [83] and atoms can not be evaporated by standard techniques. Instead of using an atomic oven, a commercially available pulsed nitrogen laser was used to vaporize and ionize thorium in one step by photoablation [84]. The production of $^{232}Th^{+}$ and $^{232}Th^{2+}$ as well as of most metal ions currently used in optical frequency standards or quantum logic clock experiments with ion traps is shown using a time-of-flight mass spectrometer.

The time-of-flight mass spectroscopy is an early arrival in the mass spectrometry family [85] and was prominent in the field during the 1960s. The method was soon displaced by quadrupole instruments with higher sensitivity and mass resolving power, but the most significant reason for the failure of time-of-flight mass spectroscopy was the lack of technologies to facilitate the recording and processing of the mass spectrum in the microsecond time-frame. These instruments are easily obtained and operated nowadays and were used in our experiments to measure the mass-to-charge ratio of various samples.

The time-of-flight experiments described in this chapter were preliminary tests for the ^{229}Th preparation and ionization. The knowledge gained from these experiments was used to produce thorium ions and load them to a radiofrequency trap (see chapter 5).

4.1 Setup and Time-of-Flight Principle

4.1.1 Photoablation

Photoablation is the process of removing material from a solid surface by irradiation with a laser beam. It implies the interaction of a pulsed laser with the sample surface, a sudden rising of the target temperature, the generation of a plasma and the subsequent mass ejection [86]. The laser pulse intensity has to have a higher energy than the ablation threshold intensity [87], which depends on different factors such as wavelength, pulse duration and ablation material. Below this critical value for the laser pulse intensity the number of ions emitted during a laser pulse is zero due to insufficient energy in a pulse to overcome the intermolecular forces within a volume and the dissipative effects of heat conduction and electronic-vibronic energy conversion that remove energy from the illuminated volume [88].

Photoablation is categorized by two different regimes which are distinguished by comparing the laser pulse duration with the characteristic time of electron-phonon interaction. When the laser pulse duration is shorter than this characteristic time (in metal: $\tau_{e-p} \sim$ several picoseconds [89, 90]), the intensities are high enough to break molecular bonds. The ablation threshold is smaller than that of longer pulses and the ablation rate is increased. In contrast, using longer laser pulses in the nanosecond-regime will not break intermolecular bonds. Laser ablation in this regime will transfer the energy of the laser pulse to the solid and first heat the material to the melting point and then vaporize atoms from the surface [91]. During the interaction the main source of energy losses is the heat conduction into the solid target. First experiments with laser ablation and subsequent time-of-flight mass spectrometry [92] or loading of ion traps [93] have been conducted with high-power nanosecond lasers.

The ablation threshold for thorium is not known but can be approximated by comparison with the threshold of other metals that are usually in the range of a few $10^8 \frac{\mathrm{W}}{\mathrm{cm}^2}$ [94, 95] for nanosecond pulses.

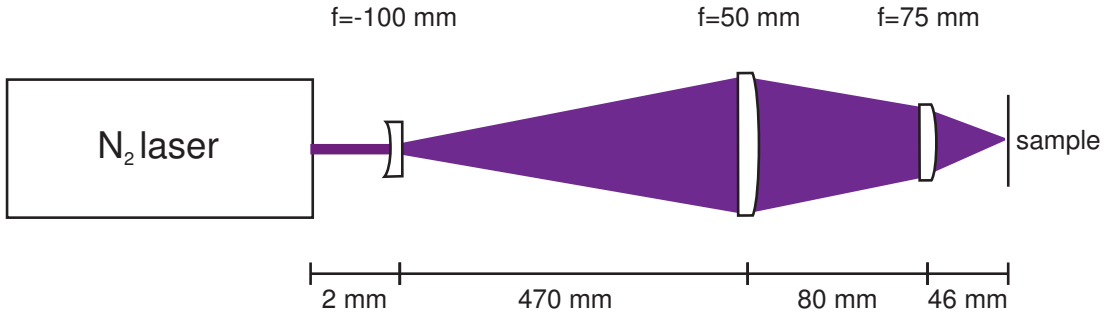

Figure 4.1: Setup of ablation laser system

With the aim to obtain a simple experimental system, we use a nitrogen laser[1] at a wavelength of 337 nm, a pulse energy of 170 μJ, a pulse width of 4 ns and a repetition rate of up to 20 Hz for our experiment. Since the pulse width is longer than the time of electron-phonon interaction, we will ablate ^{229}Th by "thermal" ablation. To obtain intensities higher than the ablation threshold, the nitrogen laser had to be focused from a beam size of $2\,\mathrm{mm} \cdot 8\,\mathrm{mm}$ created by the laser to a spot of $100\,\mu\mathrm{m} \cdot 150\,\mu\mathrm{m}$, using a setup as indicated in figure 4.1. Thus we obtain a pulse intensity of $280 \frac{\mathrm{MW}}{\mathrm{cm}^2}$ and a pulse energy density of $\approx 1.1 \frac{\mathrm{J}}{\mathrm{cm}^2}$, respectively.

[1] SRS NL-100

4.1.2 Time-of-Flight

The essential principle of time-of-flight mass spectrometry is that a population of ions moving in the same direction with identical kinetic energies but different masses m and charges q will have a distribution of velocities which is inversely proportional to $\sqrt{m/q}$. The ions gain their kinetic energy under the stimulus of an electric field and begin their acceleration from rest at the same time and in the same spatial plane normal to the acceleration vector. In the case of nonrelativistic velocities, a time-of-flight experiment can be described with newtonian physics as shown by the following equations.

To achieve a situation where a packet of ions will have the same kinetic energy, a time-of-flight experiment is divided into 4 regions. At first, ions are produced in a *production region*. The ion cloud is then moved by a small electric field to the *acceleration region*. There the ions are sped up in a strong electric field and gain most of their kinetic energy. All having approximately the same energy, they are injected in the field-free *drift region*. The mass-to-charge resolution is mainly obtained in this field-free region due to the constant velocities and thereby different flight times for ions with different mass-to-charge ratios. Finally, after traveling through this region, different arrival times will be observed in the *detection region*.

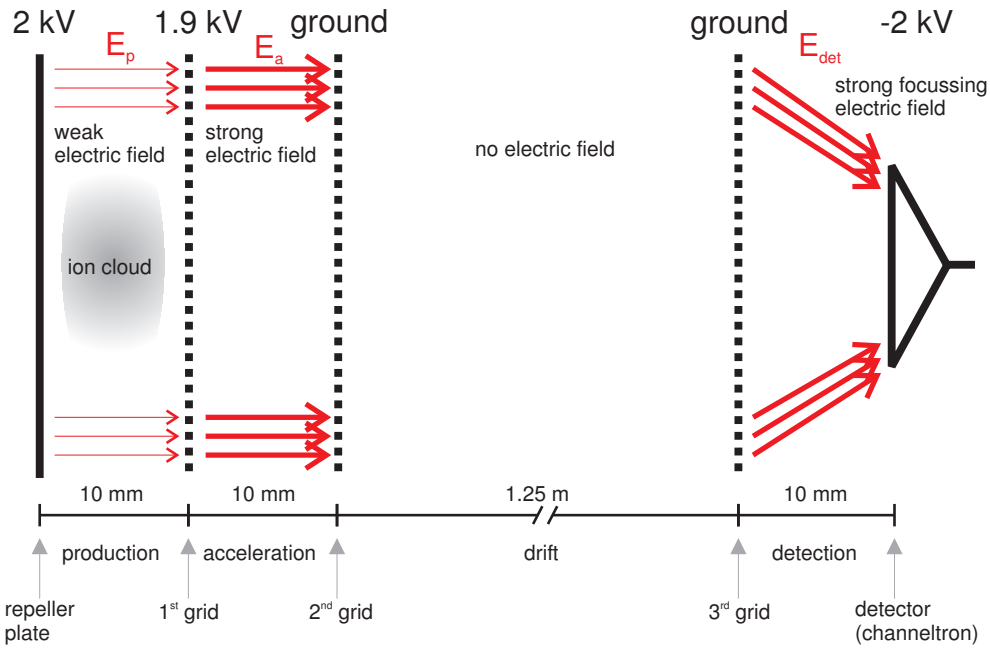

Figure 4.2: Setup of a time-of-flight experiment with voltages used in our experiment

First consider an ion created in the *production region* as indicated in figure 4.2. In the next equations, the indices p, a, d, det correspond to the *production region*, *acceleration region*, *drift region* and *detection region* while F, E, l, t, v correspond to the force, electric field, length of the region, time and velocity in the region denoted by its index. First, for simplicity, the position s_0 where the ion was created and the initial velocity v_o are neglected and it is assumed that the whole force of the electric field F_p acts on the ion. It is accelerated in a small electric field E_p with

$$F_p = qE_p = ma_p \qquad \Leftrightarrow \qquad a_p = \frac{qE_p}{m}. \tag{4.1}$$

The time t_p needed for the ion to reach the first grid is

$$l_p = \frac{1}{2}\frac{qE_p}{m}t_p^2 \qquad \Leftrightarrow \qquad t_p = \sqrt{\frac{2l_pm}{qE_p}} \tag{4.2}$$

and can be used to calculate the ion velocity

$$v_p = \frac{qE_p}{m}t_p = \frac{qE_p}{m}\sqrt{\frac{2l_pm}{qE_p}} = \sqrt{\frac{2qE_pl_p}{m}}. \tag{4.3}$$

The ion enters the *acceleration region* with the velocity v_p and is sped up to v_a, taking the time

$$t_a = -\frac{mv_p}{qE_a} + \frac{m}{qE_a}\sqrt{v_p^2 + \frac{2qE_al_a}{m}} \tag{4.4}$$

to cover the distance s_a between the first and the second grid. The division between a *production region* and an *acceleration region* ensures a nearly identical energy transfer to every ion since the main energy transfer is executed in the *acceleration region*. The ion enters the field-free *drift region* and is not accelerated anymore but only drifts with a velocity $v_d = v_a$ it has picked up from the energy transfer from the electric fields to the kinetic energy E_{kin}. Assuming the electric field to be homogeneous and produced by the potential differences in the *production* and the *acceleration region*, the time t_d the ion needs to cover this region is

$$q\left(E_pl_p + E_al_a\right) = E_{kin} = \frac{1}{2}mv_d^2 \quad \Rightarrow \quad t_d = \frac{l_d}{v_d} = l_d\sqrt{\frac{m}{2q(E_pl_p + E_al_a)}} \tag{4.5}$$

and thus the mass-to-charge resolution scales directly with the length of the *drift region*. In our experiment, the *drift region* had a length of 1.25 m while all other regions had a length of 10 mm. Finally, the ion enters the *detection region* and is accelerated due to the electric field created by the channeltron, taking the time

$$t_{det} = -\frac{mv_d}{qE_{det\|}} + \frac{m}{qE_{det}}\sqrt{v_d^2 + \frac{2qE_{det\|}l_{det}}{m}}, \tag{4.6}$$

to reach the detector, where $E_{det\|}$ denotes the electric field not produced by the detector but the field along the path of the ion. Thus, the complete time t the ion takes to reach the detector is

$$t = t_p + t_p + t_d + t_{det} \sim \sqrt{\frac{m}{q}}. \tag{4.7}$$

For an initial ion cloud with a spatial extension which is small compared to the grids and the repeller plate, the electric field can be considered homogeneous and in a good approximation can be set to $E = \frac{U}{l}$, where U denotes the potential difference in each region. Since the ion velocity is high when reaching the *detection region* (for thorium $\approx 40\ \frac{\mathrm{km}}{\mathrm{s}}$), a good simplification in this region for the calculation is a homogeneous approximation as well in the form $E_{det\|} = E_{det} = \frac{U_{det}}{l_{det}}$.

The general formula for the flight time [96] is

$$t = \overbrace{\frac{\sqrt{2m}}{qE}\left(\sqrt{E_{init} + qEl_0} \mp \sqrt{E_{init}}\right)}^{\text{time in ion source}} + \overbrace{l_d\sqrt{\frac{m}{2\left(E_{init} + qEl\right)}}}^{\text{time in } \textit{drift region}}, \tag{4.8}$$

where l_0 is the distribution of the initial position in the production region, E_{init} corresponds to the initial kinetic energy distribution, $E = E_p + E_a$ and $l = l_p + l_a$. The term $\mp\sqrt{E_{init}}$ denotes the time to turn-around when E_{init} points in the opposite direction of the electric field ($+\sqrt{E_{init}}$) or the shorter time in the electric field when E_{init} points in the direction of the field ($-\sqrt{E_{init}}$). This formula points out all the different effects accounting for the decrease of resolution.

The movement perpendicular to the electric field is not changed in a homogeneous field. This *transverse momentum* causes the ions to spread out in the plane orthogonal to the flight tube. To prevent the ions from hitting the wall of the flight tube, steering plates and einzel lenses are usually used [97]. In our experiment a 15 cm long tube was introduced in the beginning of the *drift region* where the ions are exposed to a inhomogeneous field when entering and leaving the tube. This creates a situation comparable to an einzel lens and can be used to focus the ions on the channeltron.

The pulsed nitrogen laser used in the experiment ensures an accurate temporal and spatial point source. The uncertainties of the *temporal distribution* caused by long ion cloud creation times and of the *initial spatial distribution* arising from spatial extended ion clouds at creation time can therefore be neglected.

In contrast, the *energy distribution* caused by the initial velocity vectors during the ion production can not be disregarded. This effect is closely related to the *initial spatial distribution* due to the widening of the ion cloud in the *production region* when ejecting the ions from the surface in a half-sphere. Ablated ions can have velocities up to 10 $\frac{km}{s}$ [98] and will be ejected in different directions from the surface with a maximal ejected ion flow perpendicular to the sample surface. The

initial velocity vector determines the time the ions stay in the *production region* and the energy they gain in this region. The ions with different energies have a primary focal point where the faster but later ejected ions catch up with earlier ejected but slower ions. Adjusting the grid voltages and spacing to control the location of this point is called *energy focussing* [99] and decreases the influence of this effect if the primary focal point coincides with the detector. The focal point depends on the accelerating voltages and the length of the *drift region*. Adjustments have been done on the voltages during the experiment to minimize the arrival time distribution. The estimated mass error Δm for thorium with flight times $t_{thorium} \approx 37\,\mu s$ in atomic mass units u is

$$\frac{\Delta m}{m} \cong \frac{2\Delta t}{t} \qquad \Rightarrow \qquad \Delta m \approx 5 - 10\,\mathrm{u}\ . \tag{4.9}$$

The time-of-flight mass spectrometry relies on homogeneous fields in the *production* and *acceleration region*. As it will be seen in section 4.1.3, the sample holder for the ablation samples acts as well as the repeller plate for the *production region*. This leads to an inhomogeneous field distribution at the tip of the wires and causes an uncertainty in the mass spectrometer resolution.

The *energy distribution* and the inhomogeneous field distribution in the *production region* account for a reduced sensitivity of our time-of-flight experiment. However, the resolution is still satisfactory to distinguish different elements and charge states.

4.1.3 Experiment Conduction

The ablation samples were rods of different materials with a length of 5 mm and a diameter of 1 mm. They were placed in a holder with 4 mm vertical spacing between the samples in a vacuum cube (see figure 4.3). Evacuating the cube to a pressure of 10^{-6} Pa establishes the conditions necessary for a time-of-flight experiment (see section 4.1.2). The ablation sample could be chosen by moving the laser and all lenses up and down in parallel (see figure 4.3). Focussing on the target and alignment along the sample was solely done with the f=75 mm lens. This system was used for ablation tests of different metals and thorium samples prepared after various procedures (see section 4.2).

The channeltron[2] with a gain of 10^7 was operated at a voltage of -2000 kV. The signal was converted to a voltage using a transimpedance amplifier and was measured with a digital oscilloscope[3]. A small fraction of the ablation laser beam was detected by a photo diode and triggered the start of the oscilloscope. This photodiode was used as well to measure the relative laser intensities.

[2]Burle 5901 Magnum electron multiplier
[3]Tektronix TDS520A storage oscilloscope

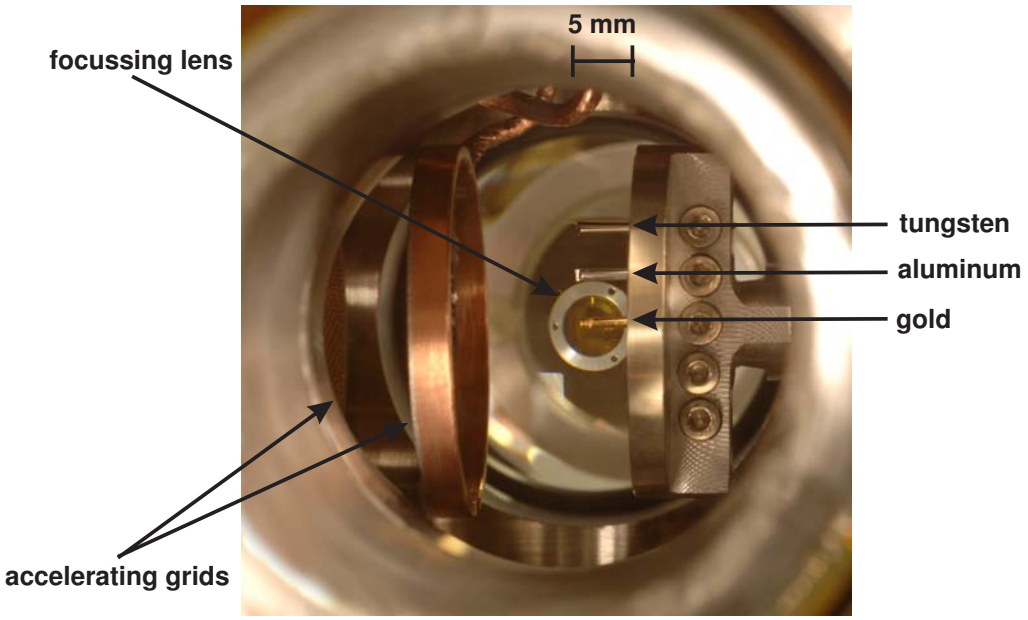

Figure 4.3: Zoom into the *production region* of our time-of-flight experiment with installed tungsten, aluminum and gold samples

The sample rods were mounted in a stainless steel holder that could hold up to 5 different samples. The sample holder had a diameter of 25 mm and was simultaneously used as repeller plate. This way the samples itself had a potential difference of $\approx$ 100 V to the first grid. The grids were made from copper with an open aperture of 87% and brazed on copper rings with a diameter of 25 mm. The sample holder and the first and the second grid were mounted in the center of a vacuum cube with 70 cm edge length. Two windows were mounted in the ablation laser axis, three openings were used for high voltage feedthrough while the last opening was connected to the flight tube. The third grid, similar to the grids in the flight tube, was placed in a small tube at the end of the flight tube. It was recessed in this small tube and mounted 10 mm in front of the channeltron, making the flight tube completely field free by grounding the grid. The distance between the second and the third grid was 1.25 m in this construction.

4.2 Thorium Sample Preparation

The experiments conducted in the time-of-flight setup are supposed to answer two questions. At first, the conditions for laser ablation with the N_2-laser of different materials in general have to be investigated. The yield of singly and doubly

charged ions as well as the oxide formation probability and the effect of surface contamination has to be determined. Thereafter, conditions for producing ^{229}Th ions from a solution with regard to ion trap loading need to be examined.

Nearly all tested elements were metals and available as 1 mm thick rods. These rods were cut to a length of ≈ 10 mm to fit into the sample holder where ≈ 5 mm of the rods were inside the sample holder to fix the wires. All materials were cleaned with acetone to remove surface contaminations. The tested silicon samples were wafers that were cut and clamped in a phosphorus bronze sheet that could be mounted in the sample holder.

Tests for the thorium yield have been conducted with a ^{232}Th wire[4] as well as with a thorium solution[5]. Due to the high activity of ^{229}Th it is not possible to obtain or handle a solid ^{229}Th sample. While a 1 mm thick and 1 cm long rod of ^{232}Th has an activity of 750 Bq and can be handled without shielding, a wire of ^{229}Th with the same dimensions had an activity of 1.3 GBq and is therefore highly dangerous. The usage of small amounts of ^{229}Th is inescapable and will be available at the PTB as a solution with about the same concentration[6] as the ^{232}Th solution used in the experiments. The chemical properties of ^{229}Th and ^{232}Th are the same and allow risk free tests of laser ablation of ^{232}Th from a solution.

The dissolved ^{232}Th samples should satisfy different demands. On the one hand, the thorium solution should be easily applied and precisely placed to the substrate. On the other hand, the substrate should either resist the laser ablation by the N_2-laser or the produced ions should not be stored in the linear Paul trap described in chapter 5.

Tested substrates for ^{232}Th that could not be ablated by the N_2-laser due to higher required laser powers than available for cracking internal bonds were PTFE (polytetrafluoroethylene) and Macor glass-ceramics. Metal substrates were aluminum and titanium, that can be ablated but not be stored due to the trapping conditions, and gold, that can be ablated and stored (see section 5.4, figure 5.11). Additionally, silicon was tested as a substrate, being the only non-metal material that could be ablated.

Two different methods for applying the ^{232}Th solution on the substrates were tested, galvanic coating and drying out the solution. Galvanic tests were unsuccessful due to unknown factors as choosing the adequate anode material or the dissolution composition. Tests for electroplating thorium on a gold cathode produced a black veil on the surface where only a very small amount of thorium ions could be detected. Additionally, galvanic coating requires a higher amount of dissolution than drying out a drop on the surface and does not allow to specify the position of the coating but produces a layer on the whole substrate.

[4] Thorium wire, 1.0 mm thickness, 99.5% ^{232}Th, purchased from Goodfellow

[5] Th AAS standard solution, ^{232}Th 1 mg/ml, $Th(NO_3)_4$ in 5% HNO_3, purchased from Alfa Aesar

[6] $Th(NO_3)_4$ in 0.1 mol/l HNO_3, 384 kBq/g

Drying out the solution worked for different materials. A single drip of solution, that corresponds to approximately 10 μg of ^{232}Th was applied with a thin pipette to the tip of the material. For soft metals like aluminum the tip of the substrate was flattened to support an evenly drying. Prior to the dripping of the solution, all materials were cleaned with acetone. The aluminum substrates were treated with a sodium hydroxide (NaOH) solution to remove the sapphire (Al_2O_3) layer on the surface. No difference was detected in the time-of-flight experiments for Al substrates treated and untreated with NaOH, most likely due to the fast reaction rate of the aluminum with the oxygen in the air and the subsequent reforming of a visible tarnished Al_2O_3 layer within a few seconds.

During the drying process, the samples were heated to $\approx 50\,°C$ to accelerate the vaporization of the water in the aqueous solution. When the solution was completely dried out, the substrate was either used directly in the TOF experiment or aftertreated by placing it on a heating plate at 400 °C for about 30–60 s or in a Bunsen burner flame for 3 s. The heating in a bunsen burner is known as flaming pyrolysis [100, 101] and causes a chemical transformation from the nitrate into an oxide. Both heating methods were conducted to achieve higher adhesion forces between thorium and the substrate. While the flaming pyrolysis lead to blackened surfaces with an unstable thorium yield, heating the substrate on the plate produced a thin white veil and increased the thorium yield by one order of magnitude as shown later in this chapter in table 4.1.

4.3 Ablation of Thorium Ions

A typical time-of-flight signal is shown in figure 4.4. Using (4.7), it is possible to distinguish different masses and charge states. The amount of produced thorium ions can be estimated by integrating the signal curve and is in the range of 10^4–10^5 ions. By applying a countervoltage in the *production region* and increasing this voltage until no ions can be detected on the channeltron, a maximum energy of 90 eV of ablated thorium ions is derived.

The analysis of the TOF signal of an ablated thorium wire shows a signal of Th^+ with the maximum of the peak in good agreement with the calculated predictions. A Th^{2+} signal is clearly seen as well, but no evidence of Th^{3+} at $\approx 19\,\mu$s is found. This is observed as well for other metals, where singly and doubly charged ions could be observed but triply charged ions were never detected (see table 4.2).

The desorbed surface layers are visible at $\approx 10\,\mu$s and the picture is repeated in ablation measurements of every tested material. The peaks for water, nitrogen and oxygen are clearly visible and distinguishable since the mass error (4.9) scales with the mass and therefore sharper peaks for lighter molecular ions are created. At about 4 μs the peak for H_2^+ is visible, which is exceptionally small in the measurement in figure 4.4 and usually matches the height of the nitrogen peak.

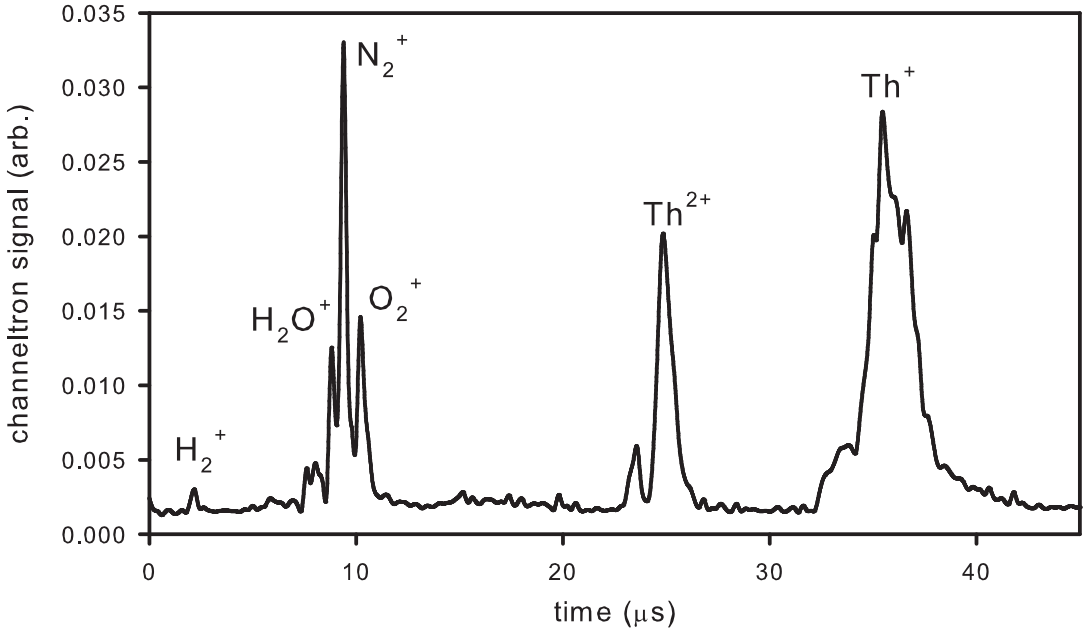

Figure 4.4: Characteristic time-of-flight measurement of an laser ablated Th wire.

Since the linear Paul trap presented in chapter 5 is not stable for oxygen and lighter elements, the minimization of these contaminations was not necessary and the focus of the measurements was on the optimization of the laser ablation and production of heavy ions.

The used N_2-laser is close to the ablation threshold as it was mentioned in section 4.1.1. By lowering the laser power, it was possible to get closer to the ablation threshold and eventually produce laser pulses than could not cause any laser ablation at all. The results for the laser power dependence of thorium are shown in figure 4.5.

The laser power dependence was tested for gold and thorium. The results of gold are similar to the plotted graph for thorium, but the influence on the production of doubly charged ions can only be observed for thorium since no Au^{2+} was observed in the experiments. The laser power was measured with an attenuated fraction of the laser beam from the photodiode signal used for triggering the time-of-flight experiment. This way, only relative measurements of the laser power were possible. The absolute numbers in figure 4.5 are calculated based on these relative measurements and assume a loss of 10% of the laser power at the coated lenses and the uncoated fused silica window. The number of detected ions were normalized to the number of Th^+ with full laser power.

The detected ablation threshold for Th^+ was $\approx 85 \frac{\mathrm{MW}}{\mathrm{cm}^2}$ and for $Th^{2+} \approx 130 \frac{\mathrm{MW}}{\mathrm{cm}^2}$, which were the lowest powers where ions could still be detected. The reduction of

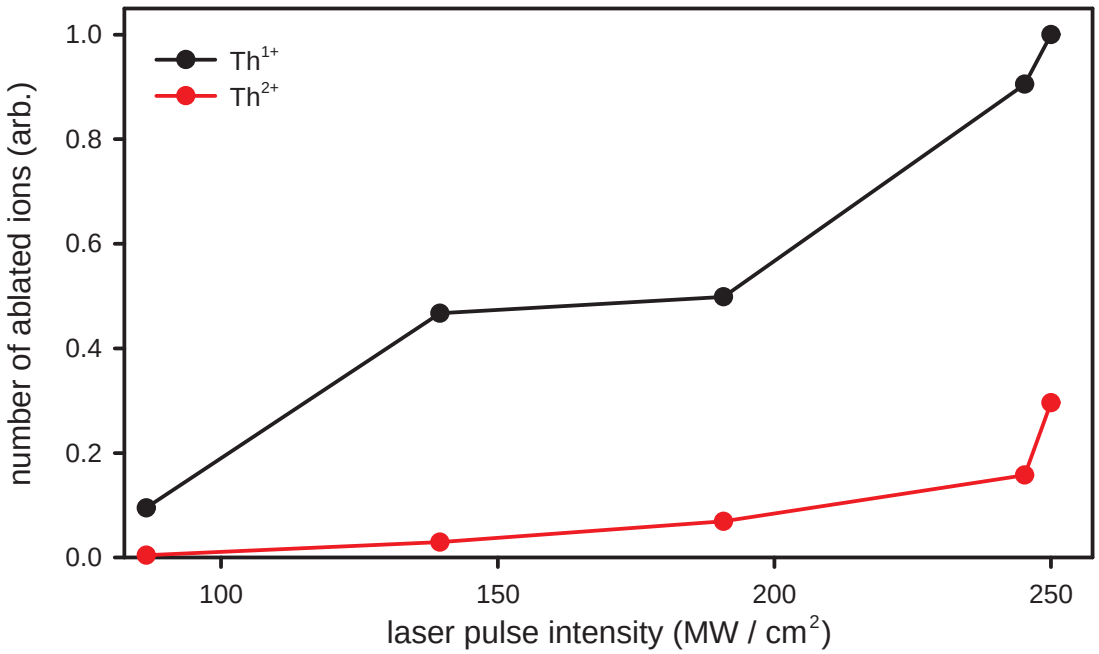

Figure 4.5: Normalized graph of ablation laser power dependence, yield of Th^+ at maximum power was set to 1.

produced Th^{2+} is already 50% when decreasing the laser power from 250 $\frac{MW}{cm^2}$ to 245 $\frac{MW}{cm^2}$ while the diminution for Th^+ is 10% for this laser power decrease. This indicates as well that the necessary laser power for producing Th^{2+} is higher than for Th^+. The curves provide an indication that using higher laser powers will lead to higher ion yields for both Th^+ and Th^{2+}. Since the capacity of the linear Paul trap that is loaded by laser ablation is limited and the ion trap is supposed to be loaded with singly charged ions, it is not clear if the increase production of Th^{2+} when using higher laser powers would interfere with the loading of Th^+ ions.

The tests for ablation of thorium from a solution are summarized in table 4.1. As mentioned in section 4.2, $^{232}Th(NO_3)_4$ was tested on different surfaces. The yields for drying the solution without treatment and heating and flaming the dried solutions are compared.

Different properties are important when producing ^{229}Th ions from a nitrate solution for the loading of a Paul trap; the amount of produced ions, the ratio of $^{229}Th^+$ to $^{229}ThO^+$ and the number of shots on the same spot that produces thorium ions before it is necessary to ablate from a different part of the substrate. Note that for every metal substrate, metal ions from the substrate could be detected as well.

Galvanic coating was only tested on gold and aluminum. Both elements were immersed in 5% nitric acid and 1 mg/ml of ^{232}Th with different cathode materials

substrate	drying (50 °C)	flaming	heating (400 °C)	galvanic
aluminum	200	2000	1000	100
silicon	100	1000	800	
titanium	5	1000		
tantalum	1000	0		
gold	500			0
Macor	0	5		
PTFE	5			
glass fiber	0			
graphite	0			
fused silica	0			
stainless steel	0			

Table 4.1: Number of shots on the same spot producing thorium for different coating methods of $Th(NO_3)_4$ on different surfaces.

and the coating was done at 2 V and a current of 100 mA maintained for 5–10 minutes. The cathode material with the best chemical properties was gold, all other materials (stainless steel, tantalum, copper) corroded in the acid. No thorium was found on the galvanic treated gold anode. It was possible to detect thorium on the aluminum anode, but the amount of thorium ablated per shot was very weak. Due to the small amount of detected ions, the uncontrollable area of the coating and the high amount of thorium solution necessary for galvanic coating, this method was not followed and therefore not considered for further tests for different substrate materials.

When drying the solution on different substrates, every substrate was cleaned with acetone before treatment and heated to approximately 50 °C to decrease the time necessary for evaporating the nitric acid. The amount of produced thorium ions per laser pulse was similar for substrates with the highest yields and Al, Si, Ta, Ti, Au would produce $\approx 10\%$ of the amount of Th^+ ablated from the thorium wire with the first laser pulse. The amount of Th^+ decreases with every shot and the maximum number of pulses on the same spot where thorium could still be detected is listed in table 4.1. Even if the flaming pyrolysis produced samples with a thicker thorium layer where thorium could be ablated longer, the ratio of Th^+ to ThO^+ is better for samples heated on a heating plate, where most of the detected ions are Th^+ ions and in the flaming pyrolysis most of the detected ions were ThO^+ ions. Additionally, even if the substrates were held in a clean flame for only 2–3 seconds, the surface showed sooted regions.

As seen in table 4.1, heating the substrate on a heating plate or in a flame increased the total thorium yield substantially, with tantalum being the only ex-

ception where thorium could solely be detected when it was dried on the surface at low temperature.

The material showing the best properties for laser ablation of a dried thorium solution from a surface was aluminum that was heated to approximately 400 °C for one minute. It produces a big amount of aluminum ions as well but since these ions have a weight of 27 u, they cannot be trapped in the linear Paul trap and therefore will not disturb the trap. The light weight of aluminum is one of the biggest advantages over gold and tantalum with a weight of 197 u and 181 u, respectively. They will produce metal ions in the stable regime of the Paul trap and can therefore be trapped. Aluminium will not possess this disadvantage.

4.3.1 Laser Ablation Ion Production of different Metals

The most important elements nowadays used in ion trap experiments were tested and the results and yields for the different charge states as well as the oxides are noted in table 4.2. PTFE and Macor are not included in the table since no ions could be detected. When testing Macor with a dried $Th(NO_3)_4$ solution, it was observed that the whole material could be lighted with the laser and the ceramics was glowing blue. This points out the scattering of the laser light in the Macor and indicates that the ablation was not successful due to the distribution of the laser energy in a big volume and therefore not reaching the ablation threshold in the Macor or the dried thorium on the surface.

at. no.	element		1+	oxide 1+	2+	oxide 2+
13	aluminum	Al	0.51			
14	silicon	Si	0.80			
20	calcium	Ca	4.73			0.98
29	copper	Cu	1.06			
38	strontium	Sr	1.44	2.98		0.20
42	molybdenum	Mo	0.58		0.10	
49	indium	In	1.79			
70	ytterbium	Yb	0.80	5.45		0.32
73	tantalum	Ta	0.74			
74	tungsten	W	0.37			
79	gold	Au	0.58			
90	thorium	Th	1.00		0.27	

Table 4.2: Relative ablation strengths of different elements and ionization states, normalized to the yield of Th^+, J=250$\frac{MW}{cm^2}$.

Considering ablation in the nanosecond-regime a thermal process related to heating, neglecting differences in absorption, heat conductivity and surface roughness,

it is appropriate to plot the dependence of the ablated material from the evaporation heat. Figure 4.6 shows a possible way to subsume the results for all ablated materials.

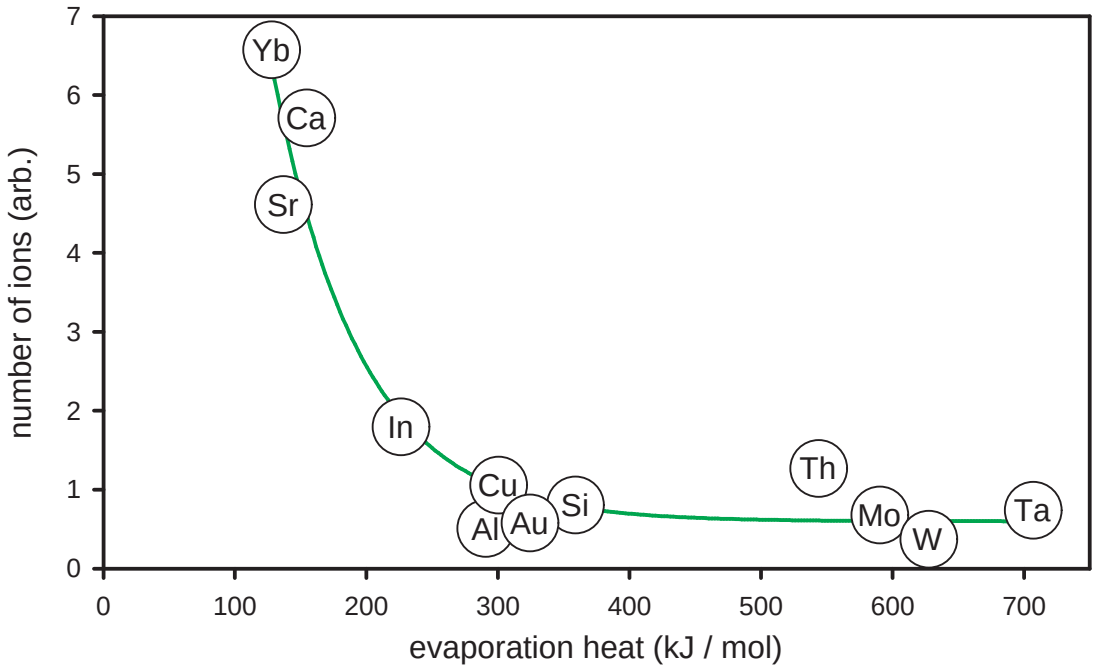

Figure 4.6: Overview of the amount of all ablated ions including oxides and doubly charged ions and their boiling temperatures.

For this graph, the amount of all detected ions including doubly charged ions and ionized oxide molecules were summed to obtain a total number for the amount of detected ions. It can be seen that metals with a lower evaporation heat (and thus lower boiling temperature) have a higher yield of ablated ions. When comparing figure 4.6 with table 4.2 it can be noticed that the tested metals with a lower heat of evaporation, namely ytterbium, strontium and calcium, are the ones producing a high amount of oxides and hence figure 4.6 is only correct direct after focussing the ablation laser on a new spot. The total amount of these ions decreases when cleaning the surface as seen in figure 4.8 and will adapt to the yields of all other metals in this process. Furthermore, it can be seen that the laser ablation works for metals in a wide range of evaporation energies and the method can therefore be used to produce ions without the need for high temperatures in an atomic oven. Silicon as the only tested semiconductor could be ablated as well while PTFE needs higher laser intensities to break the molecular bonds.

4.3.2 Oxidized Samples without prior Surface Treatment

The composition of the detected ions showed a high share of oxides for Sr and Yb as shown for strontium in figure 4.7. The used metal samples were heavily oxidized due to exposure to air and usually have to be handled in a protective gas atmosphere to avert the formation of oxide layers. The black curve denotes the detected signal right after focussing on a new spot of the Sr sample. The amount of detected SrO^+ ions is twice the amount of Sr^+ ions. Doubly charged SrO^{2+} ions are detected as well, but no evidence of non-oxide doubly charged Sr^{2+} is found.

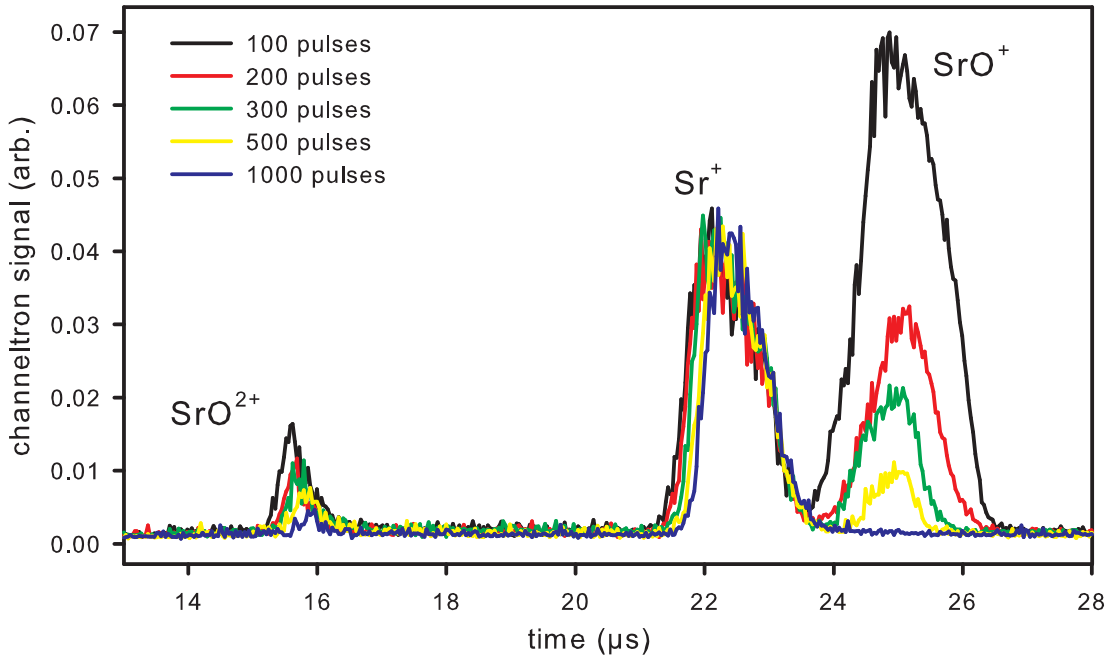

Figure 4.7: Removal of strontium oxide with multiple shots on the same spot.

Repeated laser pulses on the same spot decrease the amount of detected SrO^+ and SrO^{2+} ions significantly until no oxide ions are detected after approximately 1000 shots in the case of strontium. The amount of ablated Sr^+ is nearly constant in this process and corroborates the belief that the oxide ions are ablated directly from the surface of the metal and are not produced during the ablation process in the created plasma.

Figure 4.8 shows the number of oxide ions in the produced ion ensemble and the dependence of the number of laser pulses on the same spot for strontium and ytterbium. Both metals can be cleaned from the oxide layer effectively without adjusting the focal point of the laser. The reason for the higher amount of pulses necessary to clean the strontium surface completely than necessary for ytterbium can very likely be found in the high reaction rate of strontium with oxygen. It

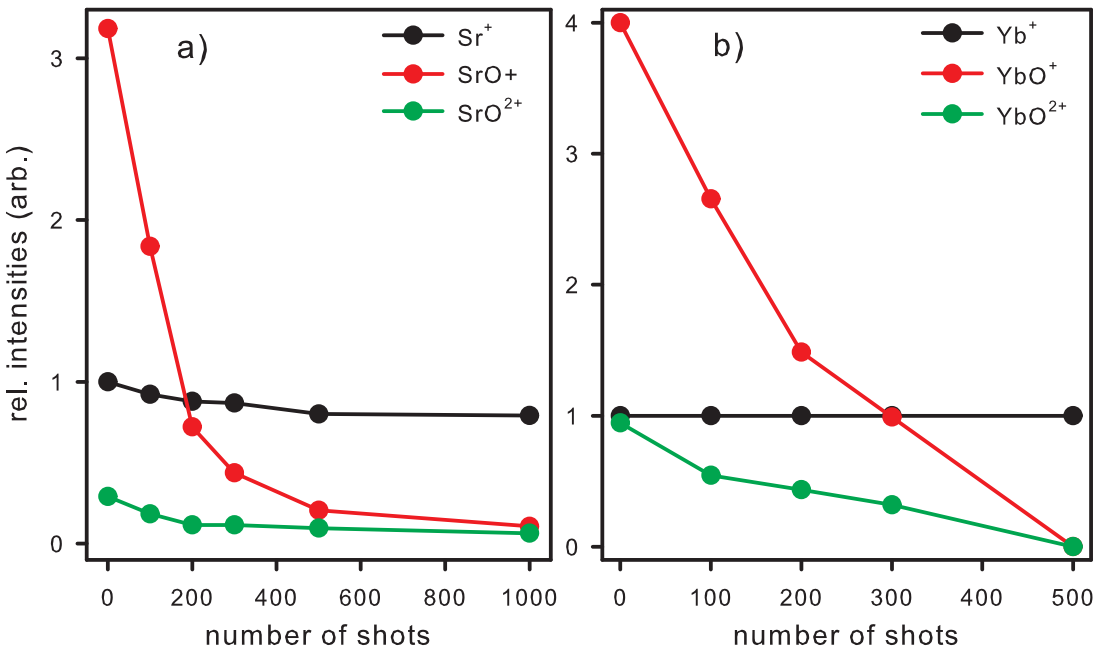

Figure 4.8: Ion and oxide ion concentration of a) strontium and b) ytterbium. Both metal surfaces can be cleaned by repeated laser pulses on the same spot until the oxide layer is completely removed.

creates a clearly visible white film of SrO on the surfaces when stored in an oxygen containing atmosphere. The higher reaction rate of Sr compared to Yb creates a SrO layer that is thicker than the YbO layer and more laser pulses are necessary for strontium to remove this layer than for ytterbium.

The approach of cleaning the surface with multiple laser ablation pulses prior to an actual experiment is an effective method to investigate and load ion traps with highly reactive elements. Usual experiments with strontium require careful cleaning and handling procedures in an protective gas atmosphere to prevent the material from forming an oxide layer when exposing it to air. When using laser ablation for loading an ion trap with strontium, the setup can be prepared without the precautions and Sr^+ can be produced after removing the surface layer by laser ablation.

5 Thorium in a Linear Paul Trap

In 2007, the γ-spectroscopy measurements of Beck et al. determined the energy of the isomeric state at 7.6 $\pm$ 0.5 eV (2.14) and thus shifted the range for expected photons produced in the decay to the ground state from the near ultraviolet to the vacuum ultraviolet (VUV) region. This value was higher than the ionization energy for Th^+ and as well higher than the band gap in all thorium compounds. Hence it it necessary to develop a new scheme for excitation of ^{229m}Th and detection of the produced photons. Working with thorium ions in vacuum is a promising approach.

Storing ^{229}Th in a ion trap avoids all the restrictions of earlier experiments. Whilst a Penning trap [102] overlaps a static quadrupole field and a static homogeneous magnetic field, a Paul trap [103] relies exclusively on an alternating high frequency electric quadrupole field to trap ions. Due to the expected small excitation rate (see section 2.1.3) and the small resonance width of the isomeric state (see section 2.1.8), it is beneficial to trap many ions for spectroscopy experiments. Since a Penning trap requires a strong magnetic field inducing a Zeeman splitting to the electron shell [104] and therefore forbids undisturbed measurements, a linear Paul trap was set up for spectroscopy experiments with ^{229}Th.

The production of Th^+ ions by laser ablation necessary for operating a radiofrequency trap has been described in chapter 4. We designed a linear Paul trap, loaded and stored up to 10^5 ions and performed laser spectroscopy on the strong resonance line of Th^+ at 401.91 nm.

5.1 The Linear Paul Trap

The operation principle of a radio frequency ion trap is explained in a wide range of books (e.g. [105]) and articles (e.g. [106]). This chapter will focus on the essential characteristics of a Paul trap and emphasize the attributes of a linear radiofrequency (RF) trap.

To confine ions in an electric field in vacuum with harmonic particle movements, a quadrupole potential in the general form

$$\phi(\boldsymbol{r}) = \frac{U}{2r_0^2}(\alpha_1 x^2 + \alpha_2 y^2 + \alpha_3 z^2) \tag{5.1}$$

is necessary, where U is the voltage, r_0 is the distance from the center to the electrodes and $\boldsymbol{r}^2 = x^2+y^2+z^2$ in cartesian coordinates. In a charge-free space, the

Laplace equation $\Delta\phi(\boldsymbol{r}) = 0$ enforces the condition $\Sigma_i \alpha_i = 0$. While the solution $\alpha_1 = \alpha_2 = 1$, $\alpha_3 = -2$ results in a three-dimensional quadrupole potential, a two-dimensional quadrupole potential as needed for a linear Paul trap is created by choosing $\alpha_1 = 1, \alpha_2 = -1, \alpha_3 = 0$. The resulting shapes of the quadrupole potential are compared in figure 5.1.

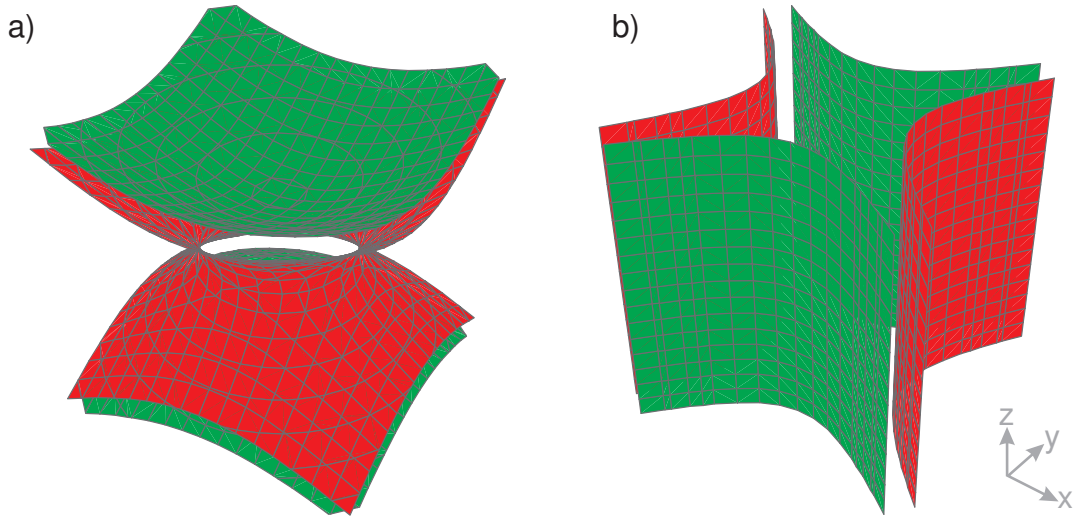

Figure 5.1: Equipotential surfaces of a static a) three-dimensional and b) two-dimensional quadrupole potential. Repulsive surfaces are marked in red, attractive in green.

Even though this two-dimensional potential is attractive in one dimension, it is repulsive in the second dimension and therefore excludes the possibility of obtaining an ion trap by using only static electric fields. However, if the quadrupole potential is periodic in the form

$$\phi_{xy}(x, y, t) = (U_{DC} + U_{RF} \cos \Omega t) \frac{x^2 - y^2}{2r_0^2} \tag{5.2}$$

with U_{DC} and U_{RF} being the static DC voltage and the amplitude of the time-dependent RF voltage respectively, a dynamic trapping in the x- and y-direction can be achieved by alternating repulsive and attractive electric forces. This principle of a linear Paul trap is adapted from the electric quadrupole mass filter [107]. The electrode configuration creating this dynamic quadrupole entrapment is shown in figure 5.2.

When choosing the correct parameters and initial conditions, the ion is trapped inside the x-y-plane but not along the z-axis. In order to achieve trapping along this still field-free axis, further changes are inevitable. This can be done with different configurations, for example adding electrodes to this third axis or closing

opposing quadrupole electrodes at the end. Because this would block the optical access along this axis, we have chosen a configuration known as a segmented linear Paul trap as shown in figure 5.2. The radiofrequency is applied to all segments but is superimposed with an additional electric field produced by a voltage U_{EC} in the end segments, reducing the trapping region to the middle section.

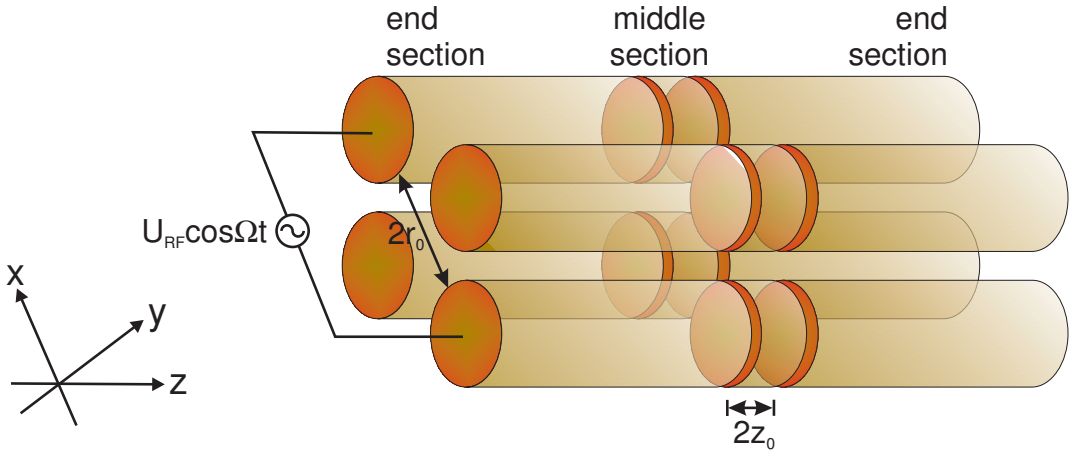

Figure 5.2: Sketch of a segmented linear Paul trap. r_0 and z_0 are the lengths from the Trap center to the end of the electrodes.

The static potential produced by this additional voltage U_{EC} can by approximated using a multipole expansion. The dipole term cancels out in this expansion due to the symmetry of the electrodes and the quadrupole term is the dominant one. When the length of the middle section is sufficiently long, the potential can be treated as harmonic in the trap center and higher orders of the expansion can be neglected [108]. This creates an axial potential $\phi_z(\boldsymbol{r})$ that is superimposed with the radial potential $\phi_{xy}(x, y, t)$ and the complete linear trap quadrupole potential $\phi(\boldsymbol{r}, t)$ reads

$$\phi(\boldsymbol{r}, t) = \phi_{xy}(x, y, t) + \phi_z(\boldsymbol{r}) = \phi_{xy}(x, y, t) + \frac{\kappa U_{EC}}{z_0^2}\left(z^2 - \frac{x^2 + y^2}{2}\right) , \qquad (5.3)$$

where $\kappa\,(< 1)$ is a geometrical factor and z_0 denotes the distance along the z-axis from the trap center to the end electrodes. The parameter κ represents the quadratic expansion coefficient of the multipole expansion and depends solely on the geometry of the trap. The approximation for the axial potential is comparable to the axial confinement created in a static three-dimensional quadrupole potential, where the solution of the general form (5.1) leads to the parameters $\alpha_1 = \alpha_2 = -1$ and $\alpha_3 = -(\alpha_1 + \alpha_2) = 2$.

The equations of motion for an ion with mass m and charge e in a potential $\phi(\boldsymbol{r},t)$ are calculated easily from this potential using $F(\boldsymbol{r},t) = -e\nabla\phi(\boldsymbol{r},t)$:

$$m\frac{\mathrm{d}^2}{\mathrm{d}t^2}x + e\left(\frac{(U_{DC} + U_{RF}\,\cos\Omega t)}{r_0^2}\right)x - e\,\frac{\kappa U_{EC}}{z_0^2}x = 0 \tag{5.4a}$$

$$m\frac{\mathrm{d}^2}{\mathrm{d}t^2}y - e\left(\frac{(U_{DC} + U_{RF}\,\cos\Omega t)}{r_0^2}\right)y - e\,\frac{\kappa U_{EC}}{z_0^2}y = 0 \tag{5.4b}$$

$$m\frac{\mathrm{d}^2}{\mathrm{d}t^2}z + e\frac{2\kappa U_{EC}}{z_0^2}z = 0\ . \tag{5.4c}$$

This set of equations can be a transformed in the form of a Mathieu equation, that is well-known in mathematical physics [109]. Introducing dimensionless parameters one obtains for the equations of motion

$$\frac{\mathrm{d}^2}{\mathrm{d}\tau^2}u + (a_u + 2q_u\,\cos 2\tau)\,u = 0\ , \qquad u = x, y, z \tag{5.5}$$

with the stability parameters

$$a_x = \frac{4e}{m\Omega^2}\frac{U_{DC}}{r_0^2} - \frac{4e}{m\Omega^2}\frac{\kappa U_{EC}}{z_0^2} \tag{5.6a}$$

$$a_y = -\frac{4e}{m\Omega^2}\frac{U_{DC}}{r_0^2} - \frac{4e}{m\Omega^2}\frac{\kappa U_{EC}}{z_0^2} \tag{5.6b}$$

$$a_z = \frac{8e}{m\Omega^2}\frac{\kappa U_{EC}}{z_0^2} \tag{5.6c}$$

$$q_x = -q_y = \frac{2e}{m\Omega^2}\frac{U_{RF}}{r_0^2} \tag{5.6d}$$

$$q_z = 0 \tag{5.6e}$$

$$\tau = \frac{\Omega}{2}t\ . \tag{5.6f}$$

In order to achieve stable ion trapping, it is necessary to find solutions of the Mathieu equation with bounded amplitudes for $\tilde{u} = x, y$. The stability of this solution is characterized by the parameters $a_{\tilde{u}}$ and $q_{\tilde{u}}$ and does not depend on the initial conditions. Since the Mathieu equations are independent in x- and y-direction, the $(a_{\tilde{u}}, q_{\tilde{u}})$-plane is divided into stable and unstable regions for both directions. To obtain overall stability we have to focus on the overlapping region of x- and y-stability. The first stability region is plotted in figure 5.3 and has stable solutions for $|q_{\tilde{u}}| < 0.908$ [110] at $a = 0$.

To deduce the frequencies of the ion motion inside the trap, the general solution of the Mathieu equation

$$u(\tau) = \sum_{n=-\infty}^{\infty} c_{2n,u}\left(A_u\,e^{\imath(\beta_u+2n)\tau} + B_u\,e^{-\imath(\beta_u+2n)\tau}\right) \tag{5.7}$$

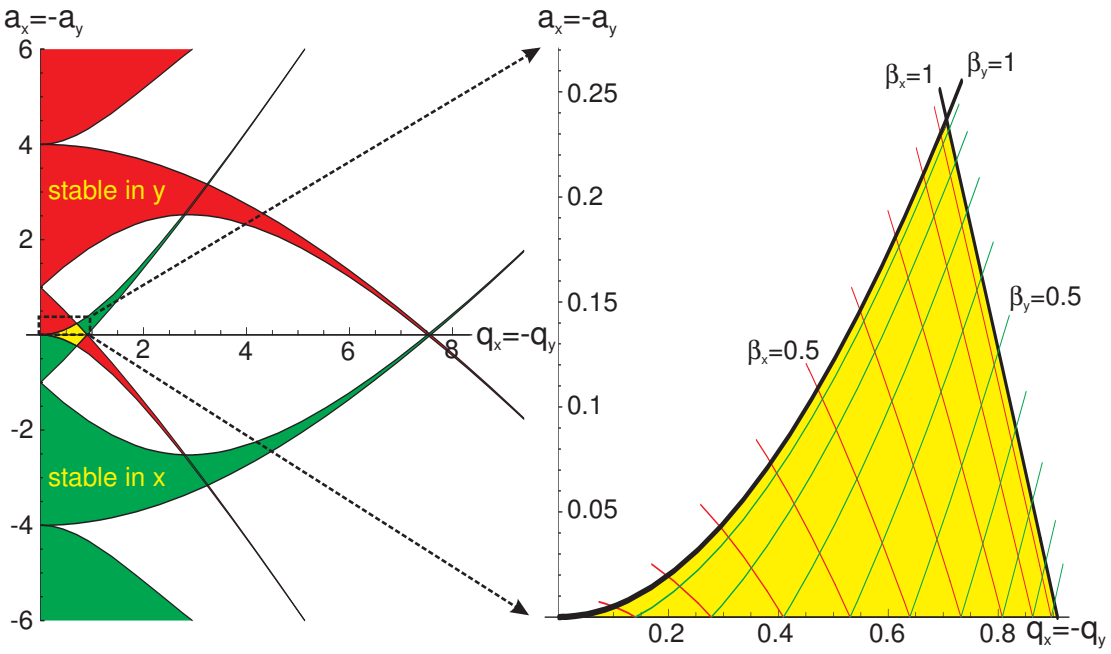

Figure 5.3: Overall stability diagram for the two-dimensional quadrupole field (with $U_{EC} = 0$) and zoom into the lowest region for simultaneous stability in x- and y-direction.

is needed. While the β_u and $c_{2n,u}$ are functions of a_u and q_u, the A_u and B_u depend exclusively on the initial conditions. The stable solutions as shown in figure 5.3 are obtained when β_u is a real number, hence from (5.7) the frequency spectrum

$$\omega_{n,u} = (\beta_u + 2n)\,\frac{\Omega}{2}\,, \qquad\qquad n = 0, \pm 1, \pm 2, \ldots \tag{5.8}$$

is determined.

A good approximation for the ion motion is known as the adiabatic solution, where only the first order solutions ($n \in \{0, \pm 1\}$) of the series expansion for $\omega_{n,u}$ are taken into account. Since the adiabatic solution disregards higher order terms, it is only a good approximation for small values $|a_u| < q_u < 1$. Equation (5.7) can be simplified by combining (5.6f), (5.8), $c_{-2,u} = c_{2,u} = \frac{-q_u\, c0,u}{4}$ [102] and $\rho_u = c_{0,u}\sqrt{A_u^2 + B_u^2}$ [105] to

$$u(t) = \rho_u \cos\omega_{ps,u}t \left(1 - \frac{q_u}{2}\cos\Omega t\right) \tag{5.9a}$$

$$= \underbrace{\rho_u \cos\omega_{ps,u}t}_{\text{secular motion}} - \underbrace{(\rho_u \cos\omega_{ps,u}t)\,\frac{q_u}{2}\cos\Omega t}_{\text{micromotion}} \tag{5.9b}$$

$$= u_{sec}(t) \qquad + u_{micro}(t)\,, \tag{5.9c}$$

Equation (5.9b) can be separated into a fast oscillation driven by the trap driving frequency Ω, called micromotion, and a slow motion with the secular frequency

$$\omega_{ps,u} = \frac{\Omega}{2}\beta_u \tag{5.10}$$

around the trap center. The secular parameters β_u are derived from equation (5.7) by comparison of coefficients as a continuous fraction and can be approximated in the adiabatic solution for small $|a_u|$ and q_u [104] to

$$\beta_u \cong \sqrt{\frac{q_u^2}{2} + a_u} \qquad \Rightarrow \qquad \omega_{ps,u} = \frac{\Omega}{2}\sqrt{\frac{q_u^2}{2} + a_u}\ . \tag{5.11}$$

The secular motion can be treated as a motion in a pseudopotential $\Psi(\boldsymbol{r})$ created by the time-averaged quadrupole potential. Thereby, the secular frequency $\omega_{ps,u}$ can be interpreted as the frequency of a harmonic oscillator in a static effective potential created by averaging over one period $\frac{2\pi}{\Omega}$ of the quadrupole potential $\phi(\boldsymbol{r}, t)$ [111]. The equations of motion then read

$$\frac{\mathrm{d}^2}{\mathrm{d}t^2}u = -\omega_{ps,u}^2 u = -\frac{e}{m}\frac{\mathrm{d}}{\mathrm{d}u}\Psi(\boldsymbol{r}) \tag{5.12}$$

and lead to the well known solution of the potential of a harmonic oscillator. The pseudopotential can be deduced from (5.12) to

$$\Psi(\boldsymbol{r}) = \frac{m}{2e}\left(\omega_{ps,x}^2 x^2 + \omega_{ps,y}^2 y^2 + \omega_{ps,z}^2 z^2\right)\ . \tag{5.13}$$

The depth of this pseudopotential can then be expressed as the work that is needed to move an ion from the center of the trap to the end u_0 of the electrode:

$$D_u = -e\int_0^{u_0}\frac{\mathrm{d}\Psi(\boldsymbol{r})}{\mathrm{d}u}\mathrm{d}u = -\frac{m\omega_{ps,u}^2 u_0^2}{2}\ , \qquad u_0 = \begin{cases} r_0 & u = x, y \\ z_0 & u = z \end{cases}\ . \tag{5.14}$$

It is possible to derive the values for the secular frequencies $\omega_{ps,u}$ using (5.11) and the stability parameters a_u and q_u in (5.6). While the movement of the ion along the z-axis is solely caused by the potential produced by the voltage U_{EC} in the end segments, the secular frequencies along the x- and y-axis depend on U_{RF}, U_{DC} and U_{EC}. The radial secular frequencies will be degenerated for $U_{DC} = 0$:

$$\omega_{ps,x} = \sqrt{\frac{e^2\,U_{RF}^2}{2m^2\,\Omega^2\,r_0^4} + \frac{eU_{DC}}{mr_0^2} - \frac{e\kappa U_{EC}}{mz_0^2}} = \sqrt{\tilde{\omega}_{ps,x}^2 - \frac{\omega_{ps,z}^2}{2}} \tag{5.15a}$$

$$\omega_{ps,y} = \sqrt{\frac{e^2\,U_{RF}^2}{2m^2\,\Omega^2\,r_0^4} - \frac{eU_{DC}}{mr_0^2} - \frac{e\kappa U_{EC}}{mz_0^2}} = \sqrt{\tilde{\omega}_{ps,y}^2 - \frac{\omega_{ps,z}^2}{2}} \tag{5.15b}$$

$$\omega_{ps,z} = \sqrt{\frac{2e\kappa U_{EC}}{mz_0^2}}\ , \tag{5.15c}$$

where $\tilde{\omega}_{ps,u}$ denotes the secular frequency in a linear mass spectrometer [107], that is to say a two-dimensional Paul trap without U_{EC} offset in the trapping region. The radial components of the end section potential have to be added to the two-dimensional quadrupole potential and lead to a decrease of the radial secular frequencies and a weakening of the radial pseudopotential.

The complete pseudopotential can be derived from (5.13) and (5.15) to

$$\Psi(\boldsymbol{r}) = \frac{e\,U_{RF}^2}{4m\,\Omega^2\,r_0^2}\frac{x^2+y^2}{r_0^2} + \frac{U_{DC}}{2}\frac{x^2-y^2}{r_0^2} + \frac{\kappa U_{EC}}{2}\frac{2z^2-x^2-y^2}{z_0^2} \tag{5.16}$$

in a form closely related to (5.3) but is noted by the ion as a static potential.

The maximum density ρ_{ion} of ions that can be stored inside the trap is reached when the space charge potential created by the ion cloud and given by the Poisson equation equals the pseudopotential depth [104]. Using (5.13) and the space charge density $\rho = -e\rho_{ion}$ for positive ions, the relation

$$\Delta\Psi(\boldsymbol{r}) = \frac{m}{e}\left(\omega_{ps,x}^2 + \omega_{ps,y}^2 + \omega_{ps,z}^2\right) = -\frac{\rho}{\epsilon_0} = e\frac{\rho_{ion}}{\epsilon_0} \tag{5.17}$$

is obtained. Applying the secular frequencies (5.15) to equation (5.17), the ion density

$$\rho_{ion} = \frac{\epsilon_0 \cdot U_{RF}^2}{m \cdot \Omega^2 \cdot r_0^4} \tag{5.18}$$

is calculated. The influence of U_{DC} and U_{EC} cancels out since these values do not change the overall potential depth but only deform the pseudopotential and the resulting shape of the ion cloud.

It was originally common practice to shape the inside surfaces of the trap electrodes to approximate, as far as possible, the hyperbolic equipotential surfaces shown in figure 5.1. This was mainly done in order to simplify the theoretical predictions of the field distribution. It was early recognized that any electrode geometry which produces a saddle point in the equipotential surfaces would have the quadratic potential in the neighborhood of that point in a good approximation of the form derived in this chapter [112].

Strictly speaking, the derived equations apply only to a single ion. For multiple trapped ions the Coulomb interaction has to be taken into account. When cooling the ion cloud to a temperature where their kinetic energy is lower than the energy from the Coulomb interaction, a quasi-crystalline structure would be formed, adding additional lattice vibrations to the equations of motion [113]. Since the temperature in our experiment is decreased by buffer gas cooling (see section 5.2.1 and figure 6.5) to temperatures orders of magnitude higher than the temperature for forming a quasi-crystalline structure, the influence of Coulomb crystals is negligible and the Coulomb interaction is only important in equation (5.18) for the calculation of the maximum number of ions that can be stored inside the trap.

5.2 Experimental Setup

The principle of ion traps developed in section 5.1 and the experiments for thorium ion generation in chapter 4 needed to be adapted to a setup that allows to create, store and detect thorium ions. To establish a stable and undisturbed storage of an ion cloud and prevent the ions from chemical reactions with oxygen or other compounds, working in ultra-high vacuum and designing the setup for a pressure of at least 10^{-8} Pa is necessary. The properties of the thorium experiment are described in the following subsections.

5.2.1 Ion Trap and Vacuum System

The segmented Paul trap is constructed to store as many ions as possible and is therefore large compared with other linear Paul traps. The middle section for storage of the ions is 20 mm with an overall length of the three segments of 160 mm as shown in figure 5.4. The long end sections are necessary to provide an access for the ablation laser as explained later in this section. The ratio between electrode

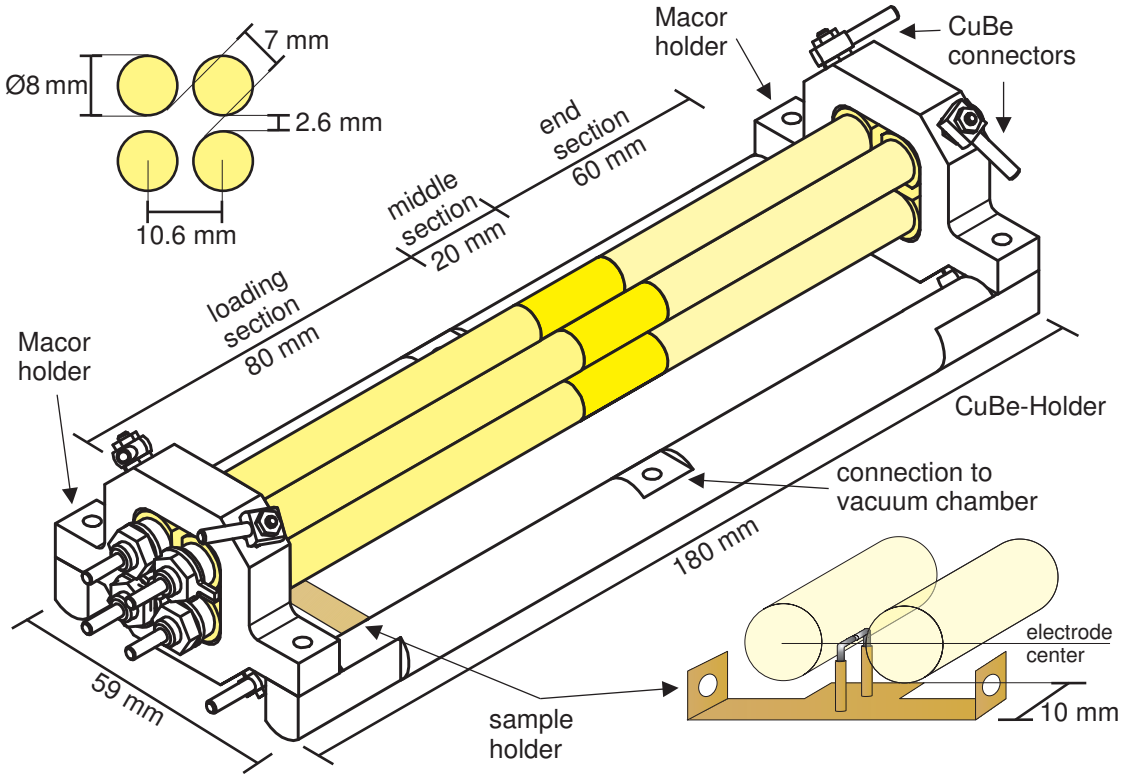

Figure 5.4: Design of the linear Paul trap and the sample holder. All dimensions in mm.

radius r_e and trapping region radius r_0 was chosen to

$$\frac{r_e}{r_0} = 1.147 \tag{5.19}$$

to ensure the best approximation to a quadratic RF potential in the x-y-plane [114].

The trap electrodes are made of copper-beryllium[1] (CuBe) and consist of three parts as shown in figure 5.5. The inner part with a length of 180 mm forms the middle section and provides the support for the loading and the end section electrode sleeves. Insulating spacers are made from Macor and placed close to the middle section and on the end of the middle part to fix the sleeves in their position. The inner part of the sleeves has an edge that forms an inset to hold the Macor and the sleeves in place. By applying a matched edge to the Macor spacer, the distance between middle and outer sections could be controlled and was adjusted to be 0.1 mm. This double-edge construction completely hides the Macor in the outer sleeves and avoids exposure of any insulating material to the trap center.

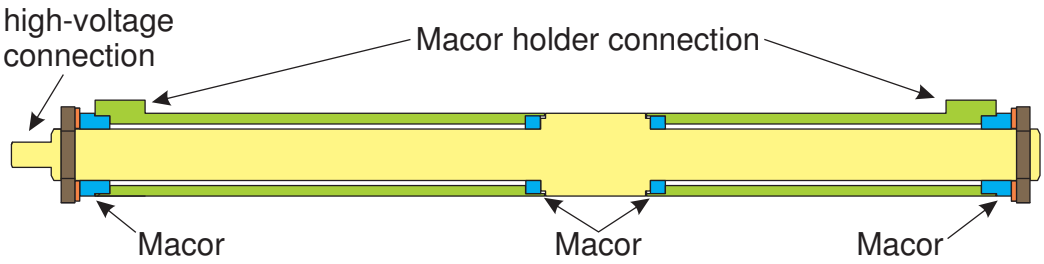

Figure 5.5: Design of an electrode.

The outer electrodes are held in place with titanium nuts screwed in threads on the end of the inner part that presses against the outer Macor spacers. This way, the middle part is completely insulated from the outer electrodes. A small outfacing hole at the end of the outer electrodes allows evacuating the hollow space in the sleeve. An extension on one side of the electrode provides the high-voltage connection to the middle section. Therefore, no wire connections are necessary to be mounted directly to the middle section, leaving the electric field in the middle section undisturbed.

The electrodes are mounted on Macor holders at both ends of the trap. Different curvatures of the Macor holder and the electrodes assure identical adjustment in the corners of the Macor holder by adduction with a CuBe setscrew to the corners of the Macor holder to support the electrodes on two lines. The high-voltage connectors are mounted on the other side of this setscrew as indicated in figure 5.4. The Macor holders are mounted on two copper-beryllium rods which are attached to the vacuum chamber in the middle of the rods. Using the same CuBe material

[1] CuBe 2 Pb W.Nr. 2.1248. CW 102.C, purchased from Brush Wellmann Gmbh

for the electrodes and the Macor holder connections assures the same coefficient of thermal expansion during the heating and cooling process of the vacuum chamber for all parts of the ion trap and protects the trap from thermal induced tensions during this process.

The ablation targets are installed in a sample holder that can hold two different 1 mm wire samples. The sample holder is fixed with insulating Macor spacers on the copper-beryllium holders and is connected to an external power supply to have the opportunity of adding a DC offset. The ablation laser is focused from the opposite side of the trap and the laser beam passes through the gap between the upper electrodes. To increase the ablation surface, the samples are bend 90 degrees to face each other (see figure 5.4), placing the ablation surface on the centerline between the lower electrodes. The position of the sample holder is chosen with respect to the viewports mounted in the vacuum chamber. The flanges for the calcium fluoride and the fused silica windows on top required a spacing that enforced the loading section length of 80 mm and the mounting of the sample holder at the end of the loading section.

The high-voltage supply connections are 1.2 mm thick silver-coated copper wires mounted sufficiently far away from the trap and the chamber surfaces to minimize the stray capacitance. Near the connectors to the trap they are shielded with ceramic isolators to protect the wires from short-circuits as seen in figure 5.6.

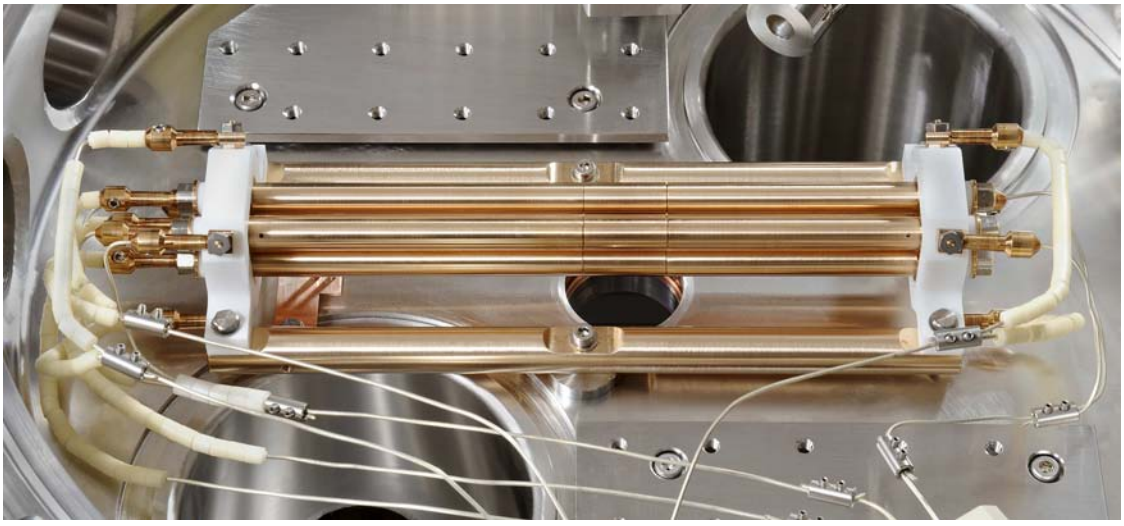

Figure 5.6: Linear Paul trap with connections.

The vacuum chamber is designed to provide six viewports for laser interaction with the ion cloud. Additional six feedthroughs are necessary for the electrical connection of all parts of the trap, the channeltron[2] and the pressure gauge. The

[2]Burle 5901 MAGNUM electron multiplier for pulse counting

height of the chamber is chosen with respect to the focussing length of the ablation laser (see figure 4.1) and the need for small distances between the trap center and the photomultiplier imaging setup (see section 6.1). The bottom of the chamber additionally needs connections for the turbomolecular pump, the NEG (Non-Evaporable Getter) pump[3] and the buffer gas inlet. The chosen design has an inner diameter of the vacuum chamber of 325 mm with a height of 46 mm as shown in figure 5.7. The chamber is made from stainless steel[4] with a very low permeability to avoid magnetic field influences on the trap.

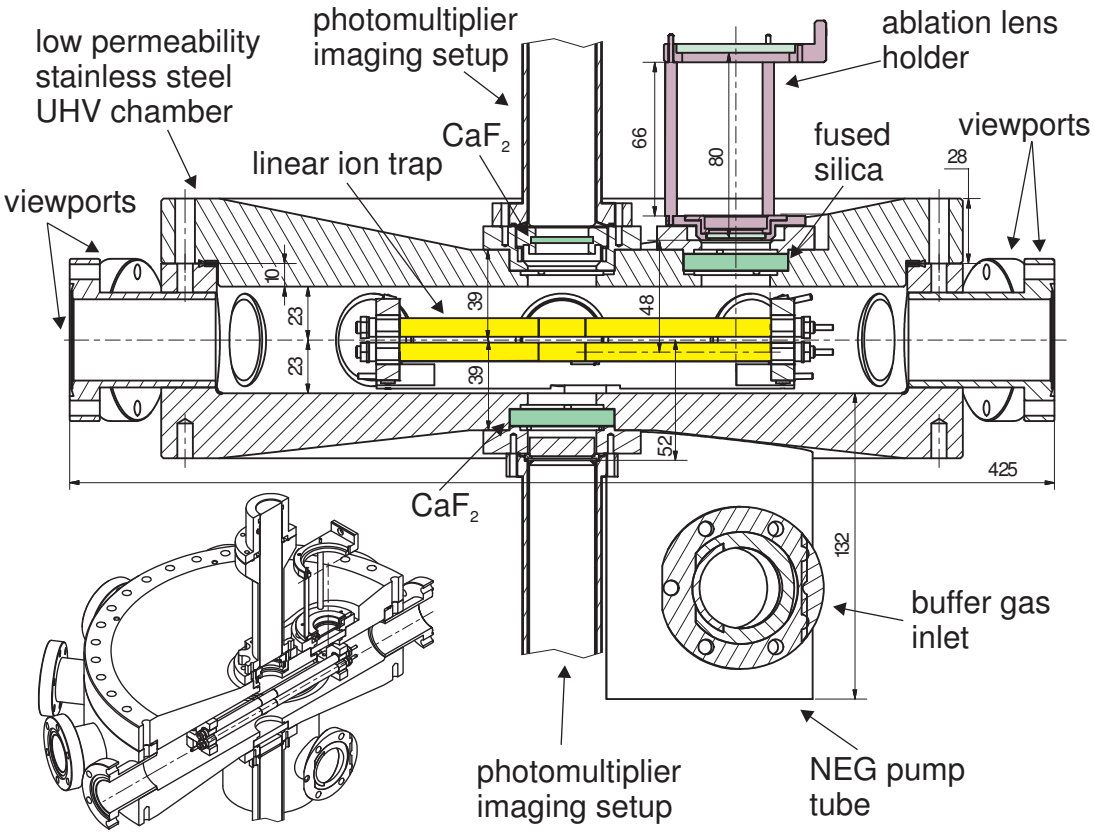

Figure 5.7: Ultra-high-vacuum chamber for the linear Paul trap.

The two feedthroughs along the trap axis are equipped with Brewster angle viewports[5], the residual four viewports are made from fused silica[6]. Three electrical

[3]CapaciTorr D 400-2, CF35, ZrVFe alloy composition

[4]stainless steel, material 1.4429-ESU, vacuum tempered, residual permeability $\mu_r \leq 1.004$, custom-made product purchased from Reuter Technologies

[5]quartz Brewster windows, purchased from Bomco, Inc.

[6]Vacom fused silica spectrosil 2000 viewport, uncoated, non-magnetic, metal-braced, aperture 38 mm

feedthroughs are mounted next to each other on one side of the chamber and provide the high-voltage driving frequency as well as the DC offset voltage for segments of the linear trap (see figure 5.10). The remaining flanges are equipped with an electric feedthrough for low voltages, a high-voltage feedthrough for the channeltron power supply and a cold-cathode pressure gauge[7], respectively. All these flanges have CF35 connections. The top of the chamber, containing a CaF_2 window and the fused silica window for the ablation laser beam, is closed with a CF300 seal.

The fused silica (aperture ⌀ 33 mm) and the calcium fluoride (aperture ⌀ 23 mm) windows on top and on the bottom of the chamber are mounted in especially designed deepenings in the chamber to obtain the closest possible distance to the trap. They are sealed with helicoflex[8] seals that can be used in direct contact with a glass surface.

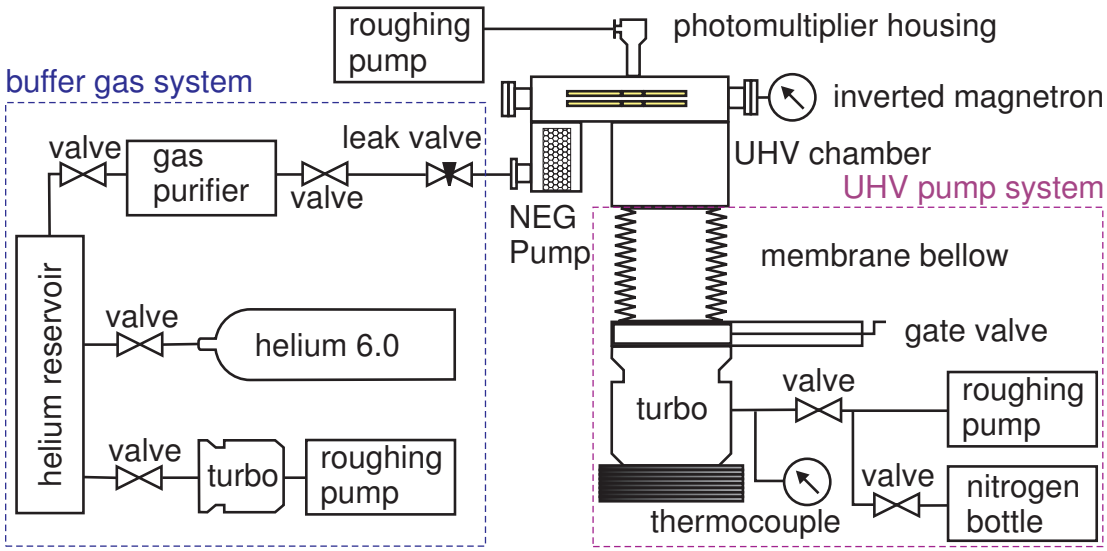

Figure 5.8: Vacuum system for the ultra-high vacuum chamber

The turbomolecular vacuum pump[9] is connected to the bottom of the chamber with a CF100 flange. To decouple the vibrations of the turbo pump from the chamber, a membrane bellow is installed in between the chamber and the pump. To maintain proper decoupling, the height of the turbo pump was adjusted to the neutral position of the membrane bellow. The turbomolecular pump had to be mounted on steel plates with a weight of 100 kg to prevent the turbo pump from being drawn upwards and squeezing the membrane bellow. The pump is connected

[7]Varian Inverted Magnetron Gauge for UHV
[8]Helicoflex-HNV-100-30.00-34.88-2.44-Cuivre, delta-shaped, purchased from Garlock France
[9]Varian Turbo-V 551 Navigator, base pressure $< 10^{-8}$ Pa

to a roughing pump[10] and a nitrogen supply for oxygen-free flooding of the chamber prior to opening.

The NEG pump is a getter pump especially designed to remove impurities like water and hydrogen from a vacuum chamber but does not bind any noble gas. It is installed in a flange designed for this pump and works without power supply after activation by heating to 450 °C. The getter material does not interact with the helium used as a buffer cooling gas and allows to improve the final pressure by two orders of magnitude to a pressure of 10^{-8} Pa. The inlet for the buffer gas is positioned at the bottom of the NEG pump flange to allow the helium to sweep along the NEG pump during the inflow of the gas and being cleaned in this process.

The buffer gas system is build to provide a clean helium supply and a constant pressure and flux of the buffer gas. To ensure this, a helium reservoir is built that can be pumped with a turbomolecular pump to a pressure of 10^{-6} Pa. After evacuating a 30 l tube working as the reservoir, it is filled with clean helium[11]. The helium passes to a flow-through gas purifier[12] that is connected with a swagelok sealed stainless steel tube to a sapphire leak valve[13] at the NEG flange as shown in figure 5.8.

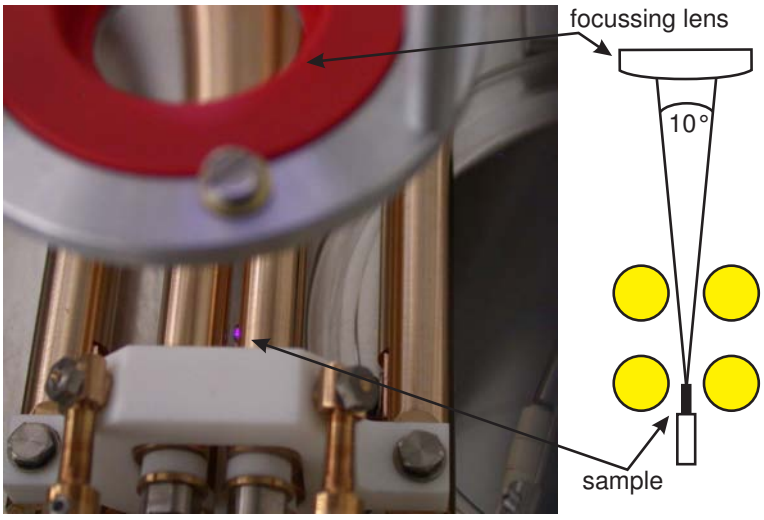

Figure 5.9: Laser ablation of a thorium sample at atmospheric pressure.

First adjustments of the ablation laser were done on the open vacuum chamber where ablation could easily be observed as a violet spot on the sample as seen in figure 5.9. Due to the longer optical path of the laser in the fused silica window in the top of the chamber, the focal point of the lens had to be readjusted after

[10] Varian DS 302 rotary-vane pump, ultimate total pressure $2 \cdot 10^{-1}$ Pa
[11] helium 6.0, purity > 99,9999%
[12] Pure Gas Products MC1-902FV
[13] Varian model 951-5100, controllable leak down to $2 \cdot 10^{-8}$ Pa-liter/s

the chamber had been closed. This luminescence was visible under vacuum as well and was therefore used for adjusting the ablation laser.

The focusing lengths for the N_2-laser were determined in chapter 4 and are shown in figure 4.1. Since the ablation window was mounted on top of the vacuum chamber, an adjustable ablation lens holder was mounted above this windows, deflecting the N_2-laser beam 90 degrees into the vacuum chamber as shown in section 6.1 in figure 6.2.

5.2.2 Electronic Setup for Storage and Detection

According to (5.2) and (5.6d), the choice of radiofrequency depends on the maximum obtainable amplitude and the aimed q-factor. The optimum trapping conditions for the highest density of trapped ions are faced with competing effects [115]. While the maximum number of trapped particles increases with the potential depth (5.25), the amplitude of the micromotion (5.9b) increases at the same time and leads to a higher loss of trapped ions. Hence, the maximum ion number is expected in a region around the center of the stability diagram in figure 5.3 and ought to stay at $q \approx 0.4$. The high-voltage power supply was checked up to 1.2 kV but was usually set to an RF amplitude of 900 V. Setting the working point to this q-factor and RF amplitude, the frequency for the storage of ^{232}Th corresponds to

$$f = \frac{\Omega}{2\pi} = \frac{1}{2\pi}\sqrt{\frac{2e \cdot U_{RF}}{m \cdot r_0^2 \cdot q}} \approx 2\,\mathrm{MHz}\ . \tag{5.20}$$

With these values the ion density ρ_{ion} deduced in (5.18) can be calculated to

$$\rho_{ion} = \frac{\epsilon_0 \cdot U_{RF}^2}{m \cdot \Omega^2 \cdot r_0^4} \approx 5 \cdot 10^{14} \frac{1}{\mathrm{m}^3}\ , \tag{5.21}$$

hence the expected storage capacity in the middle section is approximately $5 \cdot 10^5$–$1 \cdot 10^6$ ions.

The driving frequency was generated with a function generator[14] and preamplified with a high frequency amplifier[15]. With a ferrite[16] toroid transformer, the voltage of the preamplifier was increased by a factor of more than 40. The input of the transformer was matched to the 50 Ω output of the preamplifier. The complete electrical scheme is shown in figure 5.10. For computer control of all DC potentials, a buffered USB-D/A-converter was used.

[14] Agilent 33210A arbituary function generator

[15] Kalmus Wide RF Amplifier, Modell 112 C, 1-120 MHz, 25 Watts, 45 dB gain

[16] NiZn ferrite, outside diameter 90 mm, inside diameter 50 mm, thickness 13 mm, purchased from National Magnetics Group

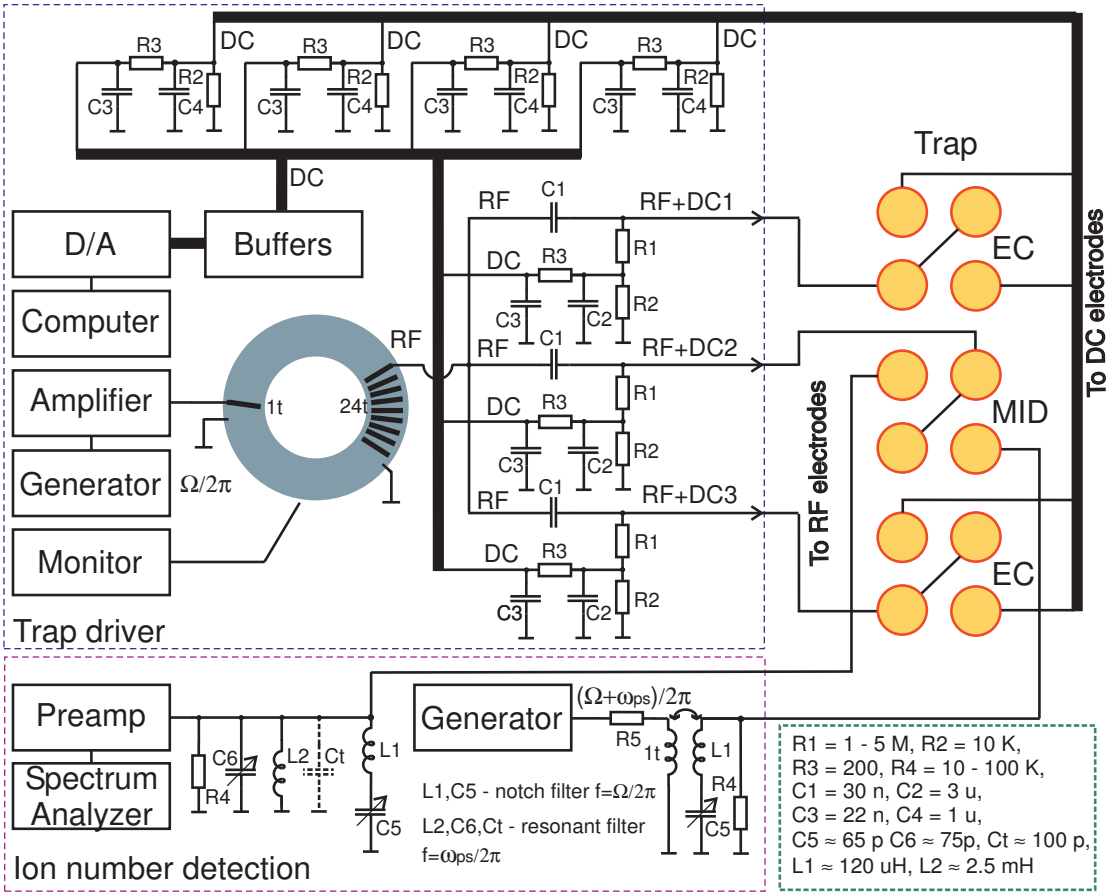

Figure 5.10: Complete electrical scheme for the trap drivers and the electronic detection of the induced secular motion for the linear Paul trap.

For the electronic detection it is necessary to determine the expected pseudopotential frequencies. The axial secular frequency $\omega_{ps,z} = \omega_z$ in (5.15c) calculates with the given parameters and a maximal geometry factor $\kappa = 1$ to

$$f_z = \frac{\omega_z}{2\pi} = \frac{1}{2\pi} \cdot \sqrt{\frac{2e \cdot \kappa \cdot U_{EC}}{m \cdot z_0^2}} = 45.9\,\mathrm{kHz}\ , \tag{5.22}$$

where $U_{EC} = 10$ V. The secular frequency $\tilde{\omega}_{ps}$ without static DC offset applied to the electrodes (implying $\tilde{\omega}_{ps,x} = \tilde{\omega}_{ps,y} = \tilde{\omega}_{ps}$) and $U_{RF} = 700$ V is

$$\tilde{f}_{ps} = \frac{\tilde{\omega}_{ps}}{2\pi} = \frac{1}{2\pi} \cdot \sqrt{\frac{e^2 U_{RF}^2}{2m^2\Omega^2 r_0^4}} = 212.5\,\mathrm{kHz} \tag{5.23}$$

and the radial secular frequency is according to (5.15a)

$$f_{ps} = \frac{\omega_{ps}}{2\pi} = \frac{1}{2\pi} \cdot \sqrt{\tilde{\omega}_{ps}^2 - \frac{\omega_z^2}{2}} = 209.9\,\text{kHz} \ . \tag{5.24}$$

The excitation of the ion cloud was done on a secular frequency sideband with the frequency $\Omega + \omega_{ps}$ to obtain a better signal-to-noise ratio than with the excitation directly with ω_{ps} [116]. The induced voltage from resonantly excited ions can be detected at ω_{ps} as shown in figure 5.10.

With the frequency (5.24), the pseudopotential well in radial direction (5.14) can be calculated to

$$d_r = \frac{m \cdot \omega_{ps}^2 \cdot r_0^2}{2} = 26\,\text{eV} \tag{5.25}$$

and indicate the maximal DC voltage that can be applied to two opposing middle electrodes before losing the ions.

5.3 Resonant Electronic Detection

Several different methods exist to characterize ion traps. The electronic detection [102, 105, 117] is a nondestructive method that can be used to study the trapping of ions without emptying the trap by exiting the ions resonantly. The resonant ejection of ions relies on the same principle but ejects the ions from the trap and counts them in a channeltron. Since measuring the secular frequencies is the main objective of the resonant ion ejection in this section, the complete channeltron detection scheme will be demonstrated in section 5.4. The feasibility of counting ions with a channeltron after they are released from the trap is sufficient to understand the ideas presented in this section.

At a RF amplitude of $U_{RF} = 900$ V and $a = 0$, the trap can have stable solutions for singly charged ions heavier than molybdenum with a mass of 96 u. The q-factor of molybdenum would be $q_{Mo} = 0.89$ and be right at the border of the stable regime at $|q| < 0.908$ [110]. For comparative measurements, a gold sample with the atomic mass of 197 u was installed in parallel to a thorium sample in the sample holder. Gold has a q-factor of $q_{Au} = 0.45$ at $U_{RF} = 900$ V and is well within the stable regime.

To verify the calculations for the secular frequency (5.24) and prepare the setup for the electronic detection on a secular frequency sideband of the trap frequency, a resonant excitation end ejection has been conducted with gold and thorium.

The ions oscillate with the frequency ω_{ps} in the trap. An energy transfer to the ions can therefore be achieved by applying this secular frequency to the DC electrodes. When the resonance conditions are fulfilled, the trapped ions will be excited resonantly, thus increasing the amplitude of the micromotion until they

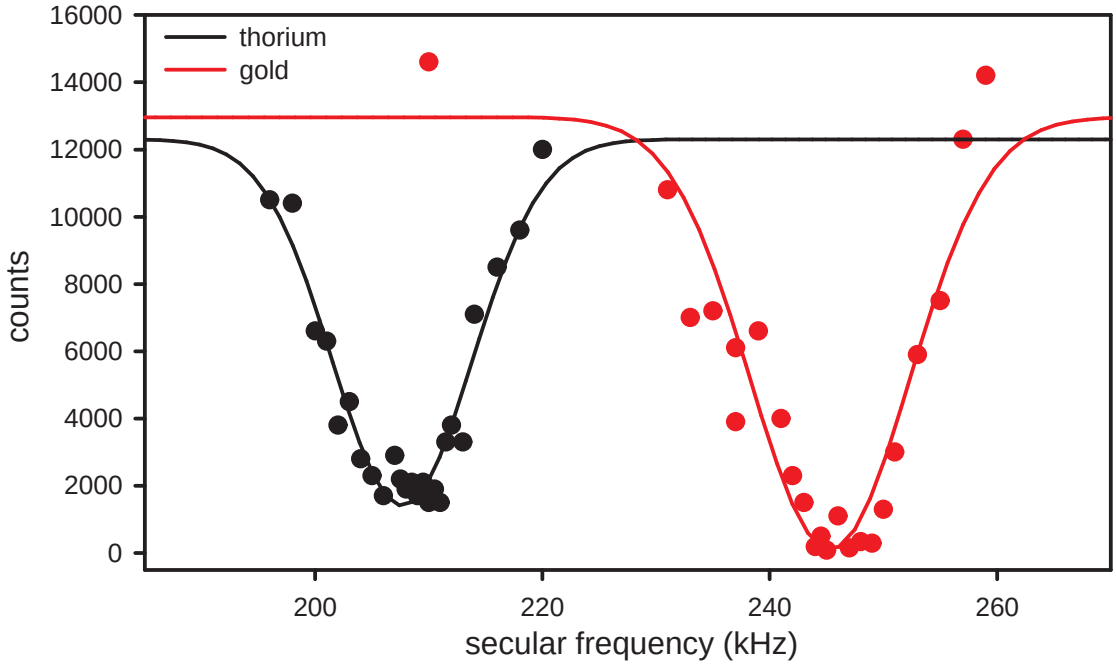

Figure 5.11: Resonant extraction of Au and Th ions.

finally are lost for trapping, either by being ejected from the trap or hitting the electrodes.

The measurements for Au and Th are shown in figure 5.11. After the trap was filled with ions, a signal with a frequency in the range of the expected secular frequency and an amplitude of 250 mV was applied to one electrode. The signal had to be maintained for at least 10^5 cycles to enable the resonant transfer of the energy to the ions. After 10^5 periods, the secular frequency signal was switched off and the amount of ions stored in the trap was measured with the channeltron detection, thus representing one data point in figure 5.11. The disadvantage of the method is the fact that the trap has to be refilled with ablated ions for every measurement point. However, the frequency of the resonant ejection by secular frequency excitation could be measured with an uncertainty of 1 kHz.

According to (5.23), the secular frequency scales linearly with the driving voltage U_{RF}. Measurements of the secular frequency were conducted for thorium for different RF amplitudes as shown in figure 5.12, where each data point represents a complete measurement run similar to figure 5.11. The linear dependence of U_{RF} is clearly observed. This measurement can be used to verify the calculated secular frequencies of $f_{ps,\,Th} = 209.9$ kHz and $f_{ps,\,Au} = 247.7$ kHz at $U_{RF} = 700$ V.

In contrast to the resonant ejection, where the determination of the number of stored ions was done with the channeltron by emptying the trap, detecting the ions inside the trap with the electronic detection does not eject the ions from the

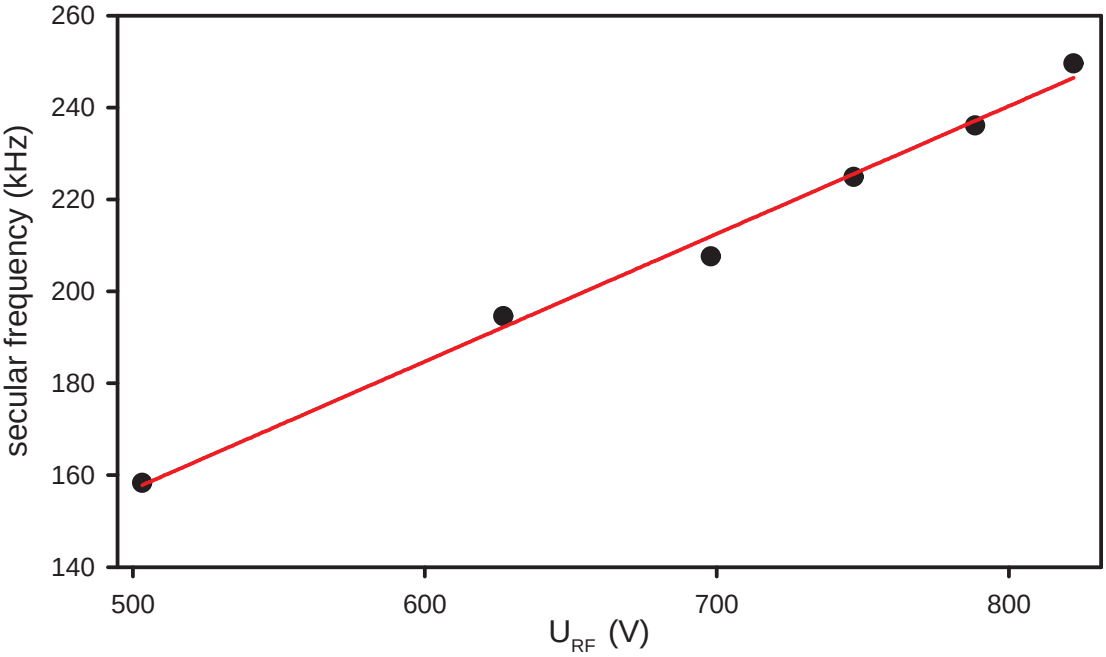

Figure 5.12: secular frequency as a function of Trap Voltage

trap. The ions are excited resonantly with the secular frequency applied to one electrode as shown in figure 5.10 and the signal is detected as a pickup signal in the second DC electrode. Since the second DC electrode works as an antenna tuned to ω_{ps}, a current will be induced from the ions oscillating at ω_{ps} as well as it would be induced from the first electrode if it was stimulated with the secular frequency. For an undisturbed measurement the frequency $\Omega + \omega_{ps}$ is applied to the generator electrode as a sideband of the RF driving frequency and excites the ions on this secular frequency sideband. The detection at ω_{ps} is then free from the voltage applied to excite the ions and the signal-to-noise-ratio is increased. The detection circuit consists of a notch filter for removing interfering voltages of the RF and a resonant filter that is tuned to ω_{ps} and takes the capacitance of the trap into account. Behind these filters, the signal is amplified and detected with a spectrum analyzer.

The detection was conducted at a fixed frequency and the fine adjustment to the secular frequency was done by changing the a-parameter of the trap with an additional DC voltage in the middle electrodes. This way, the adjustment to the resonance frequency could be done more sensitivly than by changing the sideband frequency and no changes in the resonant and notch filters for the ion detection scheme were necessary. A typical signal for thorium is seen in figure 5.13.

An excitation with $\Omega + \omega_{ps} = 2\pi \cdot 1.991\,\mathrm{MHz} + 2\pi \cdot 206\,\mathrm{kHz}$ with an amplitude of 100 mV and $U_{RF} = 685$ V was applied to measure the signal in figure 5.13.

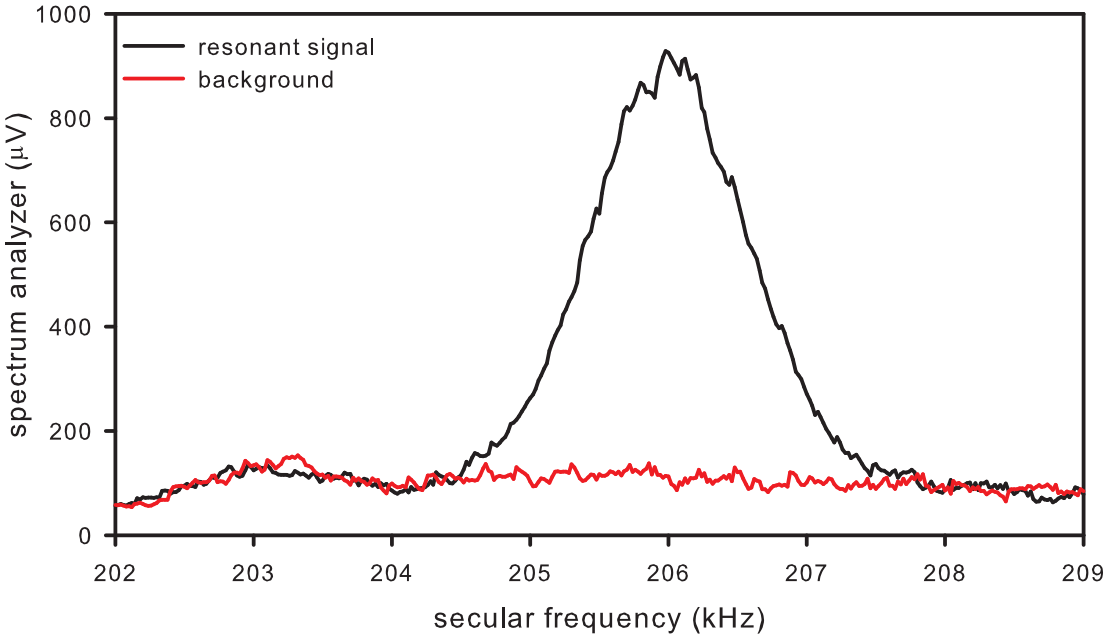

Figure 5.13: Thorium signal with electronic detection at $U_{RF} = 685$V.

The DC offset was adjusted to 3.3 V where the signal could clearly be seen. The buffer gas pressure was 0.1 Pa to ensure an efficient damping. The amplitude of 100 mV is close to the amplitude of 250 mV applied for the resonant extraction in figure 5.11. The ions are not extracted from the trap because the energy is applied to the sideband $\Omega + \omega_{ps}$ and thus the energy used to excite the ions at ω_{ps} is much smaller.

The signal from the electronic detection could be used to estimate the number of ions N in the trap via the induced current I with

$$I = \frac{N \cdot e \cdot \omega_{ps}}{2} \ . \tag{5.26}$$

With formula (5.26) an ion number of $8{\cdot}10^4$ ions is calculated. Since this expression is based on the maximum ion excursion, it will provide the minimum number of ions and it can safely be assumed that at least 10^5 ions are stored inside the trap.

The difference to the destructive channeltron detection is obvious. While the grid in front of the channeltron only applies a preferential direction for the ion movement while the RF is decreased and therefore does not ensure that all ions are detected by the channeltron, the electronic detection picks up a signal from all ions without emptying the trap. A quantitative comparison of the ion numbers detected by electronic detection and the channeltron detection used in 5.4 reveals a five times lower detection efficiency for the ion detection with a channeltron.

5.4 Ion Detection with a Channeltron

Several characterizations of the linear Paul trap were executed with the channeltron to detect the ions after release from the trap. The disadvantage of the channeltron detection is the loosing of ions inside the trap, because the ions have to be removed from the trap and have to be accelerated towards the channeltron opening. After every detection, it is necessary to reload the trap with ions. The advantage is the simple setup and the reliability of the detection method which is independent from the knowledge of the secular frequency as necessary for the electronic detection in section 5.3 or the laser excitation of the ions with the exact transition wavelength as done in section 6.2.

5.4.1 Channeltron Setup

The channeltron[17] for the ion detection is mounted perpendicular to the trap axis on a small breadboard and facing the middle section in about 30 mm distance from the trap as seen in figure 5.14. Because the ions have to pass between two electrodes to reach the channeltron, an attractive field is necessary to enable the ions to pass this gap. The channeltron will produce a strong field due to the operating voltage of 2.4 kV which could in principle serve for this purpose. To enable undisturbed trapping, this field needs to be shielded and thus can not be used to extract ions. The field of the channeltron is shielded by a grid[18] in front of the channeltron and combines these two objectives. During the trapping, this grid is grounded and shields the linear trap from the influence of the channeltron. For detection, the grid potential is switched on to 1 kV with a fast high-voltage commutator[19]. The field of the grid is then used to accelerate ions in the direction of the grid. The ions will pass the grid and are detected by the channeltron behind the grid.

Because the potential depths (5.25) and along the z-axis are in the order of about 10–50 eV (depending on the trapped element and U_{RF}), switching on the grid potential is insufficient to extract the ions from the trap. For detection, the potential depth has to be decreased until the field produced by the grid is strong enough to accelerate the ions in the direction of the grid and the ions can overcome the trapping potential. This is done by decreasing the driving voltage U_{RF} with a linear ramp from storage conditions to 0 V within 100 ms. The grid potential is switched on at the beginning of the ramp and triggers a multiscaler[20] card for the data acquisition. When the superposition of the potential produced by the grid and the pseudopotential in the trap is dominated by the grid voltage, the ions are accelerated towards the grid and detected in the channeltron.

[17] Burle 5901 MAGNUM electron multiplier for pulse counting, gain factor 10^7
[18] stainless steel, open aperture 88%
[19] Behlke HTS 41-06-GSM, push-pull transistor switch, rise time 10 ns
[20] Ortec MCS-Pci

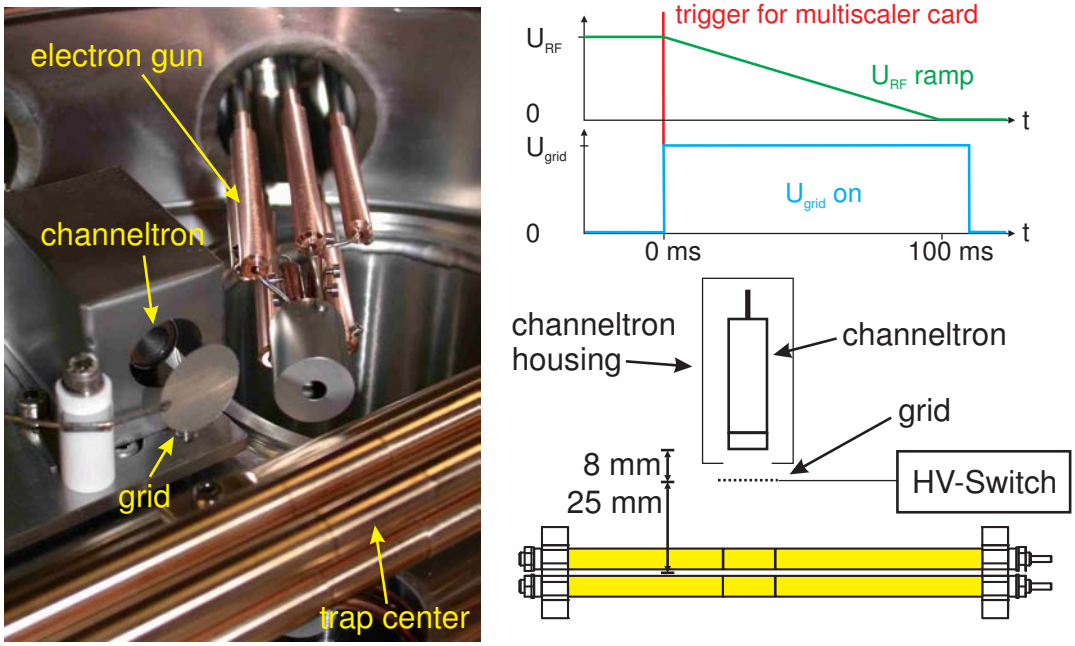

Figure 5.14: Channeltron detection setup.

In this configuration, the multiscaler card works as a miniature mass spectrometer. The decrease of U_{RF} while maintaining the driving frequency decreases the q-factor as well as the potential depth for the trap, which is different for particles with different masses. Turning on the grid voltage at the beginning of the ramp, a constant force is exerted to the ion cloud until they eventually get accelerated towards the channeltron. Due to the nonzero a-factor (5.6a), the instability region is reached at different voltages for particles with different masses and results in a complete exhaustion of the trap. This procedure allows to separate particles with different masses as well as detecting the amount of stored particles.

The channeltron pulses were intensified with a fast amplifier[21]. The computer input and output was achieved with an digital/analog converter[22] and was controlled with a Labview[23] programm that could control and detect the photon counting unit (described in chapter 6), the RF amplitude, the trigger for the ablation laser, the channeltron signal and the DC offsets.

[21] Ortec VT 120 fast preamp, bandwidth 1-300 MHz
[22] DataTranslations DT 9834-4-4-16-BNC
[23] National Instruments, Labview 7.6, Graphical user interface development system

5.4.2 Ion Trap Characterization

The detection efficiency depends strongly on the grid voltage as seen in figure 5.15 for identical loading and storing conditions. The weaker the grid field, the more thorium ions are leaving the trap in different directions, because the influence of the grid is smaller at the side of the trapping region and less ions are focussed on the channeltron.

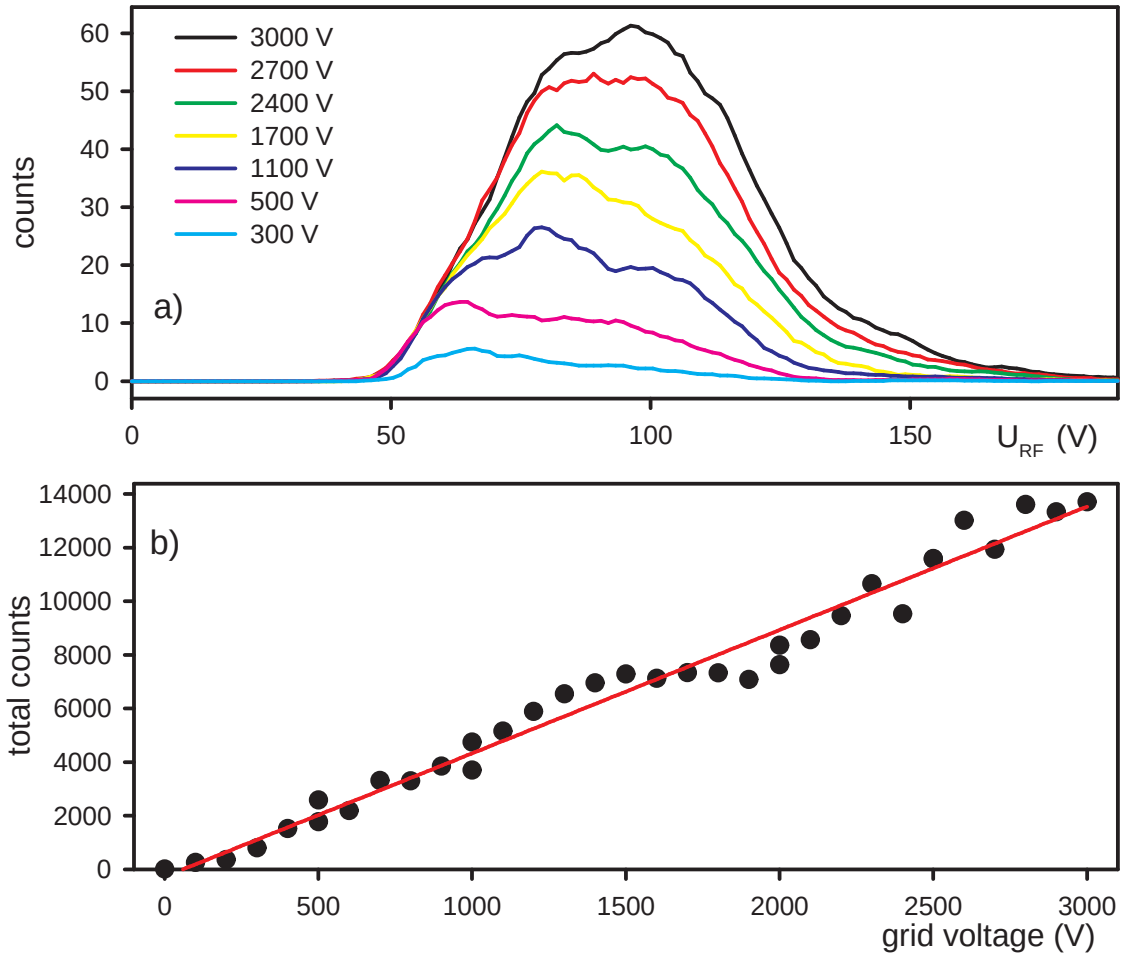

Figure 5.15: a) Detected ion counts for different grid voltages at $P = 7 \cdot 10^{-8}$ Pa. b) Grid potential dependent detection efficiency.

The measurements in figure 5.15a can be used as well to determine the geometry factor κ of the trap. While the detection of ions starts earlier (and thus at higher U_{RF}) for higher grid voltages due to the stronger force applied to the ions, the last ions are always detected at approximately the same trap voltage U_{RF}. At this point, the q-factor of the trap enters the instability region, causing a total loss of all ions left in the trap. Solving (5.6a) for κ, the geometry factor $\kappa \approx 0.3$ is

calculated. Calculations and measurements for similar trap designs [108, 118] lead to geometry factors of $\kappa = 0.325$ and $\kappa \approx 0.31$ and are within the uncertainty of our measurement of $\kappa \approx 0.3$ for our ion trap.

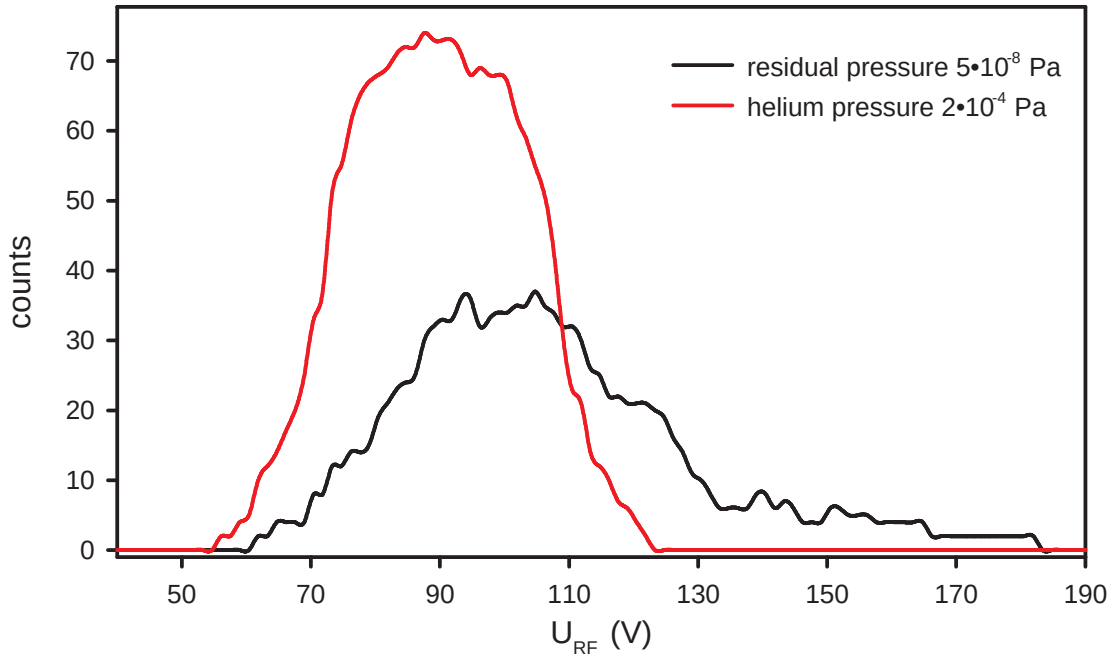

Figure 5.16: Influence of buffer gas cooling after 3 s storage time.

The influence of the buffer gas cooling is shown in figure 5.16. Collisions between the thorium ions and the helium atoms transfer the kinetic energy to the buffer gas and decrease the temperature of the trapped ions. When the ion mass is larger than that of the buffer gas, a damping term is introduced to the equations of motion and the ions are cooled [119]. To ensure a good damping, helium is used due to its small mass and its inert gas properties [120].

The buffer gas cooling works already efficiently at a pressure of $2 \cdot 10^{-4}$ Pa. As seen in figure 5.16, the maximum of the peak shifts to later detection times and therefore lower energies. Integrating the measured counts shows a count rate for buffer gas cooling of 11000 ions, which is approximately two times higher than the amount of 6000 detected ions in the uncooled case. The narrowing of the detection curve and the missing of earlier detected higher energetic ions prove a working buffer gas cooling with helium. As a result, more atoms can be trapped due to less collisions with the trap electrodes.

A dependency for the loading efficiency of the ion injection position is expected and the efficiency is assumed to be higher for ions being created closer to the trap center. Experiments with 3 different sample positions have been conducted, where the samples were installed in the middle between the electrodes as seen in figure 5.4

as well as 2 mm higher and 2 mm lower than this position. When installing the samples closer to the center of the trap, a higher count rate is observed, likewise a lower count rate is observed for samples installed further away from the trap center. As a disadvantage, the higher sample position caused interferences with the trap field and the ion capture rate was not stable. A stable ion trapping could be achieved for samples installed in the middle position and thus the sample height was maintained in the middle between the electrodes.

Determining the loading efficiency dependence of the potential depth was done by measuring the total number of counts at different RF amplitudes. The curve in figure 5.17 can be explained by taking the laser ablation velocity distribution into account. As mentioned in section 4.1.2, the velocity distribution of the ablated ions fits to a Maxwell-Boltzmann distribution on a particle beam [98].

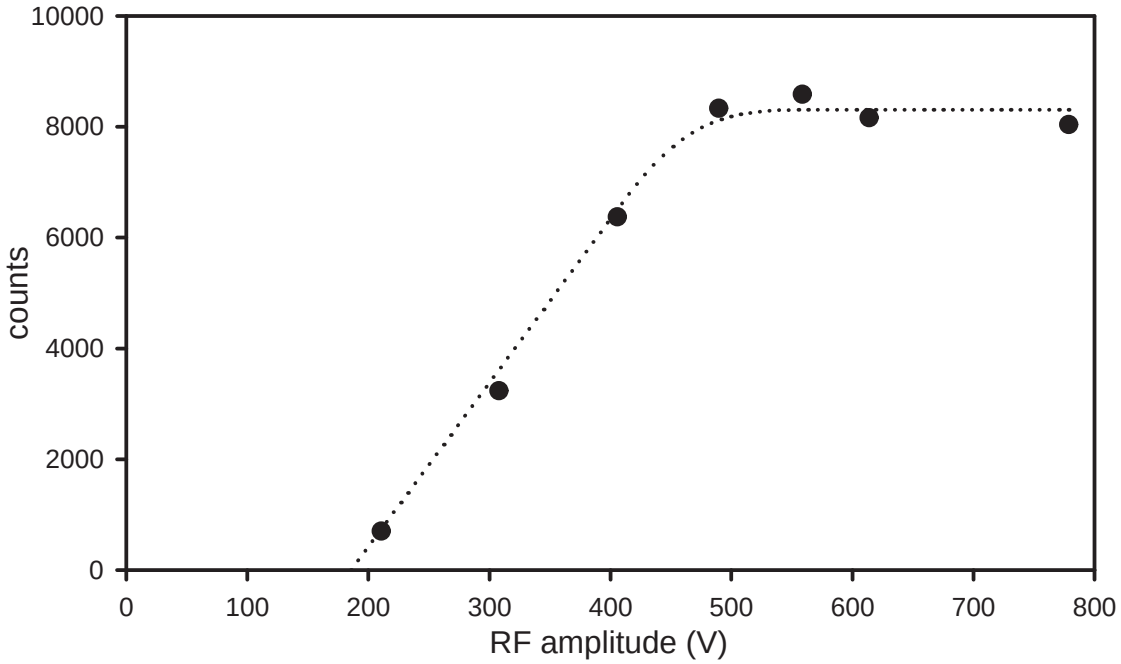

Figure 5.17: Ablation during increasing of trap voltage.

At small U_{RF} amplitudes, no ions are trapped and a capture threshold at around $U_{RF} = 200$ V is observed. The initial energy of the ions created by laser ablation is higher than the potential depth at small U_{RF} amplitudes and averts ion trapping at small trap driving voltages. For thorium, the extrapolated threshold value of $U_{RF,0} = 186$ V corresponds to $q = 0.08$ and a potential depth of $d_r = 1.8$ eV.

When reaching the capture threshold, the potential depth reaches the point were slow ions in the velocity distribution can be trapped. When the trap voltage is increased, more ions with higher velocities can be trapped due to the deeper potential depth. As a result, the velocity distribution is divided into a part of slow

ions that can be trapped and a part of ions that are still too fast for trapping. The border between these two part shifts to higher velocities with increasing RF voltages, thus trapping more ions as seen for $200\,\mathrm{V} < U_{RF} < 500\,\mathrm{V}$ in figure 5.17.

At $U_{RF} \approx 500$, a q-factor of $q \approx 0.2$ and a potential depth of $d_r = 13$ eV is calculated and the stored ion number does not increase with higher U_{RF} amplitudes. With the capture threshold value of $d_r = 1.8$ eV, the velocity boundaries for trapped ions can be derived to

$$1200\,\frac{\mathrm{m}}{\mathrm{s}} < v_{ablation} < 3300\,\frac{\mathrm{m}}{\mathrm{s}}\,. \tag{5.27}$$

This value is significantly lower than the initial energy of approximately 90 eV detected in chapter 4 for ablated thorium ions. Therefore, the determination of velocity boundaries for ion trapping is caused by the trap itself and does not imply that no faster ions are produced. Two effects may be responsible for this observation. On the one hand, ions having a high velocity may leave the trap in a time shorter than a cycle of the driving frequency and thus cannot be stored in the trap pseudopotential. On the other hand, the axial confinement for $U_{RF} > 500$ may be weaker than the radial confinement and therefore hinders trapping of faster ions.

5.4.3 Phase Dependence

The theory for the stabilization of charge carriers in a quadrupole field predicts a phase dependency of the trapping RF field and the loading efficiency [117, 121]. The ions that are supposed to be trapped must have a secular motion with an amplitude smaller than the radius r_0 of the field producing electrodes. The theory calculates a minimal secular motion amplitude and therefore maximum trapping efficiency for ions created at maximal field amplitudes.

Ion traps were generally loaded by processes much slower than the radiofrequency Ω, for example by ionizing atoms by electron bombardment. The long timescales of these processes averted a phase dependent loading efficiency measurement and did not allow a justification or refutation of the theory. In contrast, laser ablation loading of a linear Paul trap loads ions on the nanosecond timescale and is therefore capable of measuring the phase dependent loading efficiency.

The influence of the phase dependency is supposed to be prominent for high q-factors [117] and a-parameters [121]. It is relatively small for the chosen set of parameters of $q = 0.4$ and $a = 0$ in figure 5.20 but still ought to be observable. However, no phase dependence has been detected as it can be seen in the red curve. Measurements for $q = 0.2$, $q = 0.3$ and $q = 0.4$ have been conducted and lead to similar results. The red measurement points represent the number of counts detected with the channeltron under identical conditions. The timing of the ablation laser had a jitter of about $3\,\mu$s that made it impossible to trigger it on

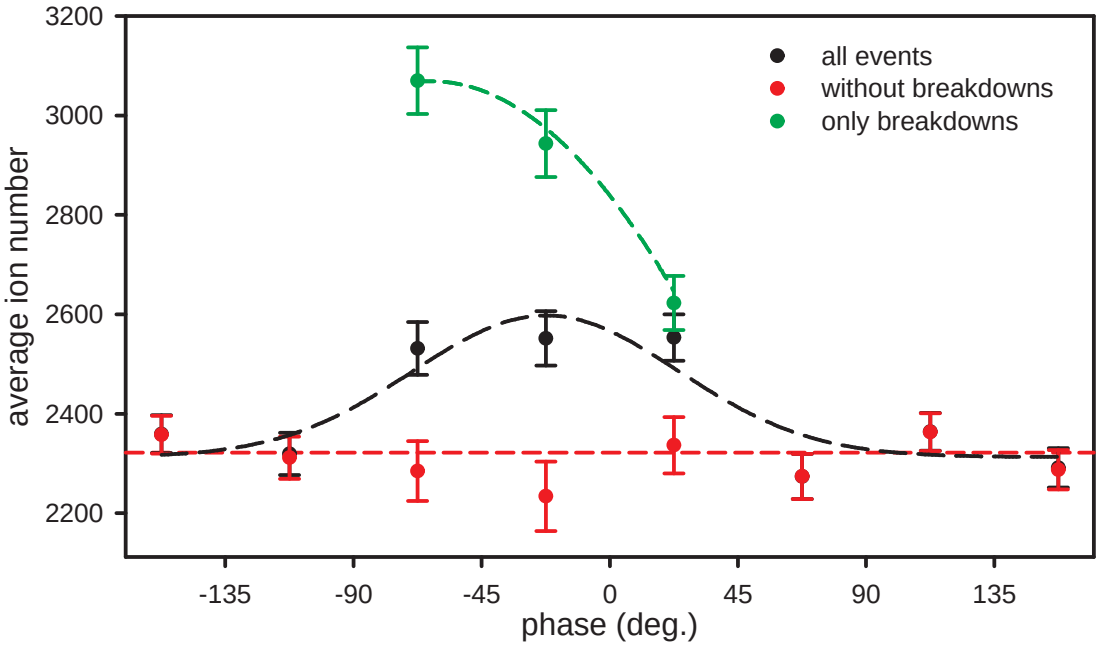

Figure 5.18: Averaged number of loaded ions versus phase of RF field during ablation, averaged over 45 ° wide bins, U_{RF} maximum at 0 °.

the phase. Instead, the phase of the RF field has been measured for every ablation shot and the count rate was averaged over 45 ° wide bins.

The green curve in figure 5.18 represents all measurements that were not conducted under normal conditions. The difference in these measurement points is the occurrence of a breakdown of the radiofrequency field. The loading efficiency is about 20% higher than in the case without breakdowns. In these breakdown, it was observed that the voltage in the electrodes decreases to small values during the ablation pulse as seen in figure 5.19. The electrons and the ion cloud produced by the laser ablation create a plasma with high conductivity between the electrodes. This enables a gas discharge that leads to a breakdown of the electric field inside the trap [122]. A typical U_{RF} breakdown is shown in figure 5.19 and shows the synchronous ablation pulse and RF breakdown.

The gas discharge ceases with the expanding ion cloud and causes the RF amplitude to recover, thus reestablishing the electric field and the pseudopotential in the trap. The timescale of this breakdown is about 5–10 cycles of the driving frequency or about 3–5 μs, respectively. For laser ablation with higher laser powers (28 mJ/pulse compared with 170 μJ/pulse for the N_2-laser in this experiment), breakdowns of the RF driving frequency to less than 1% of its maximum value for more than 50 cycles have been reported [123]. The duration of the breakdown

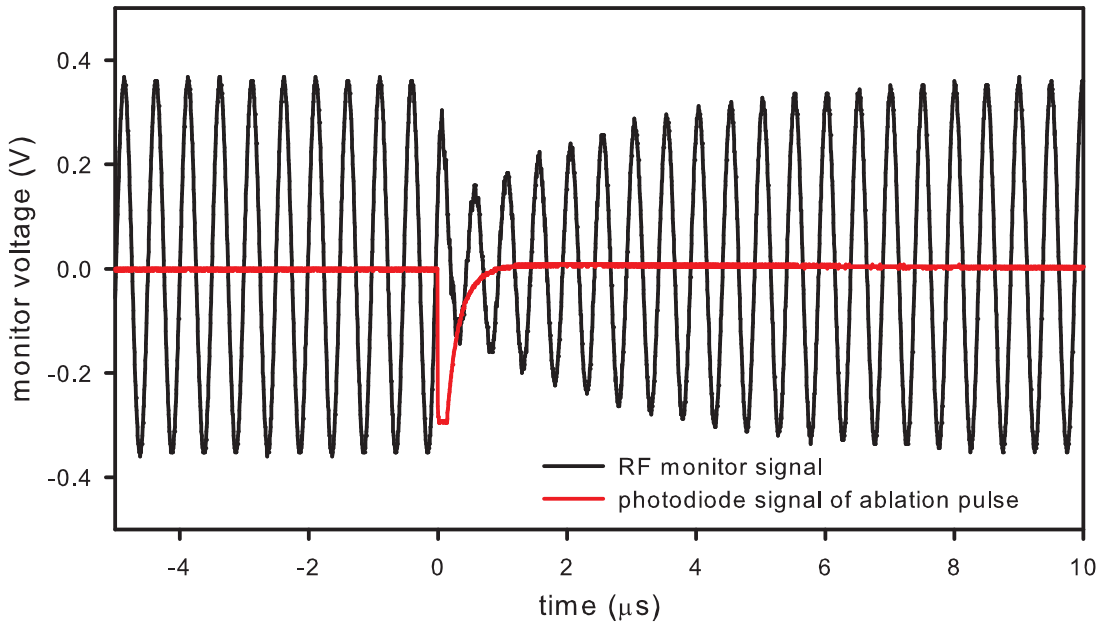

Figure 5.19: Breakdown of RF driving voltage during ablation pulse.

is three orders of magnitude longer than the ablation pulse length of 4 ns. This behavior did not occur every time ions were ablated but was phase dependent.

As seen in figure 5.20, gas discharges were correlated with the phase of the RF driving voltage and occurred only near the maximum of the sinusoidal RF driving signal. The graph denotes the measurement of the amplitude in the period after the ablation pulse. It can be seen that the gas discharge did not appear with every ablation pulse around 0°. The reason is the amount of electrons necessary for a gas discharge which was not always reached by the ablation laser. The probability for a discharge was highly increased by new focussing of the laser on the ablation target after an observed absence of a discharge with the right phase conditions. This increased the amount of produced ions and electrons and the RF breakdown probability.

No gas discharge is seen at 180°, although the RF voltage is at its maximum as well. This indicates that the discharge is caused by fast moving electrons, which are repelled when the phase of U_{RF} corresponds to negatively charged electrodes.

Phase dependent loading efficiency measurements have been reported before [124] without observation of RF breakdowns, explaining the increased loading efficiency with the hindering of the ion movement from outside of the trap to the trap center when the ions are created at phase conditions with counteracting forces from the trap center. This is not the case in our measurements. Experiments have been conducted, where the profile of the driving voltage in figure 5.19 was induced by

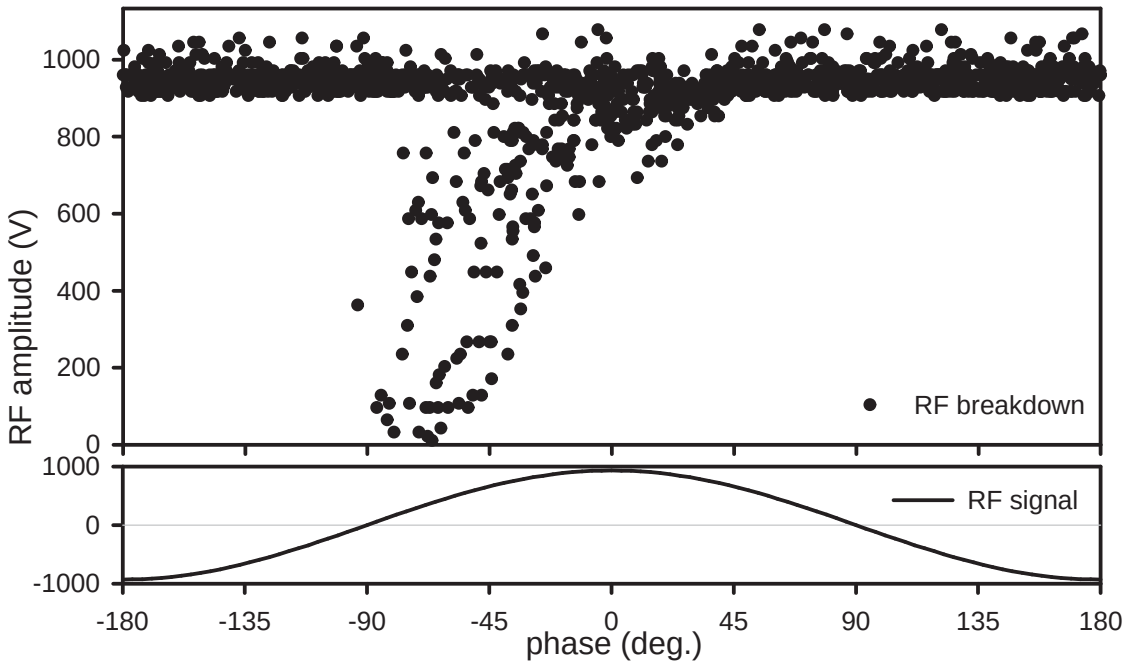

Figure 5.20: Amplitude of RF field during ablation

using a fast switchable attenuator. No increased loading rate has been observed. Hence, the reason for the higher ion number in figure 5.18 for measurements with RF breakdowns is found in an increased ion production rate correlated with the gas discharge. The discharge occurs between the RF electrodes and the sample holder and supports the ion formation by electron collision ionization of neutral thorium atoms in the laser ablated plasma.

Without these gas discharges and the subsequent higher ion production rate, a phase dependence was not monitored.

6 Laser Excitation of Th^+

For the detection of ^{229m}Th the establishment of an efficient fluorescence detection is essential. Additionally, the first step of the two-stage excitation (outlined in section 2.1.7) requires a fixed level that can be excited and detected reliably. Both objectives — fluorescence detection and intermediate level excitation — are realized in this chapter with the 401.9 nm resonance line.

The problem for the excitation of Th^+ is the complicated level structure. Several low-lying metastable levels intercept the laser excitation. The level scheme for the strongest resonance line at 401.9 nm is known [125] and shown in figure 6.1. Several metastable levels between the ground state and the 24873 cm^{-1} level [126] will disrupt the laser excitation, because the metastable levels do not couple to the 401.9 nm excitation laser due to the large detuning.

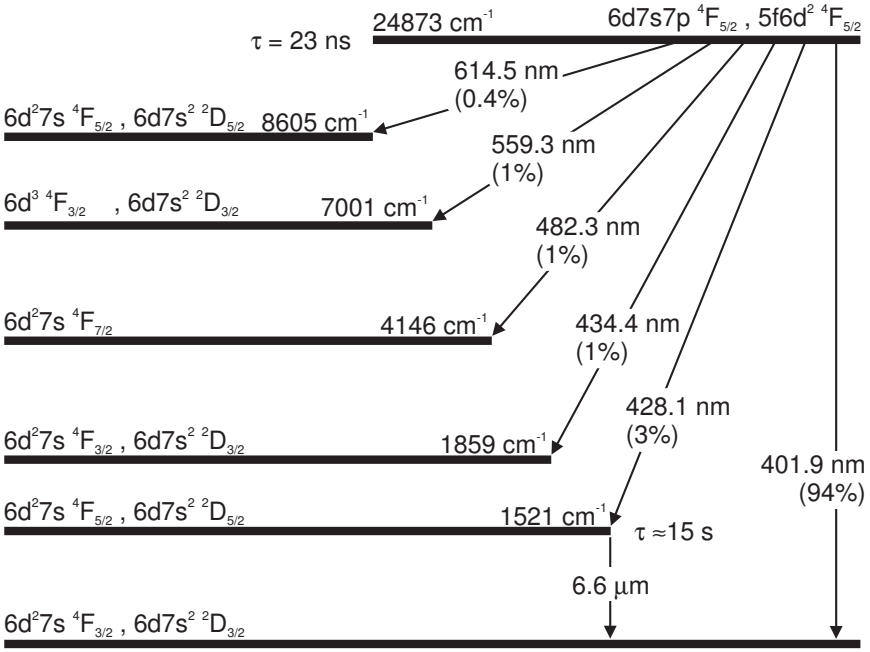

Figure 6.1: Level scheme for the excitation of the $^{232}Th^+$ resonance line at 401.9 nm.

One way to depopulate the metastable states and maintain a continuous excitation of the 24873 cm^{-1} is the usage of repumping lasers. Since five additional

laser were necessary, conducting experiments in this setup would be a complicated and hopeless endeavor. A more promising way is the depopulation by collisional quenching with a helium buffer gas [127, 128].

Buffer gas quenching is the reduction of the lifetime of a level due to collisions with helium atoms. The depopulation is usually radiationless because the energy is directly transferred to the helium atoms. In the case of thorium, the buffer gas will reduce the lifetimes of metastable states in figure 6.1 that are populated by the decay of the 24873 cm^{-1} level. These dark states are otherwise lost for the excitation of the ground state with the 401.9 nm line. The buffer gas depopulates these states faster than their natural lifetime would predict and therefore increases the amount of ions available for laser excitation. Experiments with buffer gas quenching of populated metastable levels after the excitation of the 17122 cm^{-1} level of Th^+ have been conducted [129] and proved an increased detection rate due to collisional quenching.

Single mode diode lasers are available for the 401.9 nm line. The branching ratio of the excited state with a 94% transition probability to the ground state is very favorable for buffer gas quenching experiments. All experiments were conducted with ^{232}Th which has no nuclear spin and therefore shows no hyperfine structure as ^{229}Th. However, the fine structure is the same and thus ^{232}Th can be used for laser spectroscopy, excitation experiments and detection of lines necessary to excite ^{229}Th.

6.1 Optical Setup

To excite the strong thorium resonance line, an external cavity diode laser[1] (ECDL) at 402 nm was used. The wavelength was measured by a Fizeau-interferometer-based wavelength meter[2] and adjusted to a resonance line by hollow-cathode lamp[3] spectroscopy. The 401.9 nm transition in the thorium hollow-cathode lamp was excited with the chopper modulated blue laser radiation and the optogalvanic-signal was detected with a lock-in amplifier. The strongest thorium line was observed at 401.912 9 nm air wavelength and a frequency of 745.699 36 THz, respectively and is in good agreement with the literature value of 401.912 89 nm [130]. After confirming the ECDL to be tuned to the thorium line, the radiation was transferred to the vacuum chamber and passed along the z-axis of the trap to excite the thorium ions.

The setup for the two-photon excitation of the thorium ions necessitated a second, tunable laser light source. A modelocked Ti:Sapphire laser[4] with ps–operation

[1] Toptica DL 100, maximum output power 15 mW
[2] Ångstrom HighFinesse Wavelength meter WS-7
[3] Photron hollow cathode lamp P858, filled with thorium
[4] Coherent Mira 900

and an output power of 1 W was used, pumped by a single-mode diode pumped solid-state laser[5] at 532 nm with 8 W output power. In this setup, the Ti:Sa laser was tunable from 750–850 nm. The output was frequency doubled and tripled using a second harmonic generation (SHG) and sum frequency generation (SFG) crystals[6], creating a tuneable 375–425 nm and 250–285 nm beam.

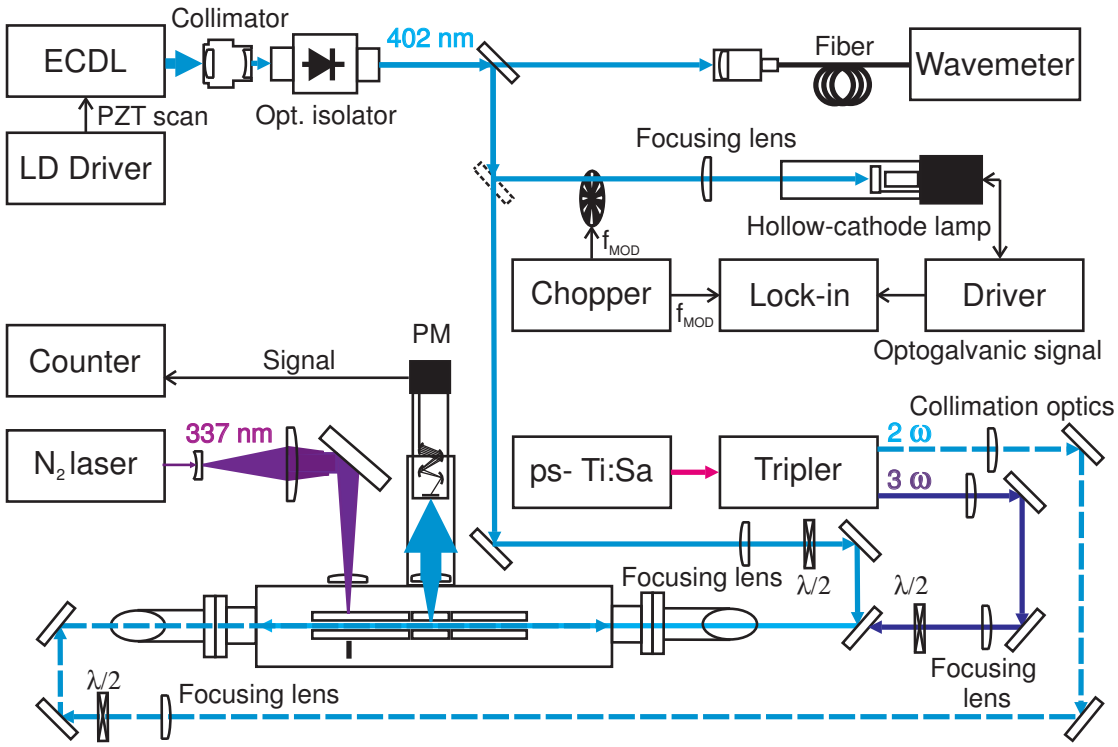

Figure 6.2: Optical setup for the excitation of the 401.9 nm line and the two photon excitation with the frequency doubled and tripled Ti:Sa laser emission

The fluorescence detection was accomplished with head-on photomultipliers[7] with different peak sensitivities. The setup allowed either mounting the photomultipliers directly in front of the CaF_2 windows or using an imaging scheme in front of the photomultipliers to focus on the middle section. In both mounting options it was possible to mount optical filters in the optical path.

To obtain a possibility for the direct detection of photons emitted from the decay of the isomeric state in the VUV range, the photomultiplier has to be installed in a low pressure atmosphere because radiation with a wavelength shorter than

[5]Coherent Verdi V8
[6]Photop TP-2000B
[7]Hamamatsu R6836, sensitivity 115 to 320 nm, Hamamatsu R7459, sensitivity 160 to 650 nm

180 nm is absorbed by oxygen. A pressure of 100 Pa ensures a residual oxygen concentration low enough to transmit the photons to the photomultiplier. This can be achieved with a roughing pump. The housing of the photomultiplier sensitive from 115 nm to 320 nm is sealed with viton rings and has a connection for a roughing pump. The housing is directly mounted on the CaF_2 flange to obtain a light tight and short connection.

The photomultiplier for the optical detection was operated in pulse counting mode. A discriminator[8] was used to convert the photomultiplier pulses to TTL pulses that were recorded by a counting unit[9]. Additionally, the TTL pulses could be detected in parallel with a multiscaler computer card[10].

6.2 Fluorescence Detection

Using the setup shown in figure 6.2, it was possible to excite the thorium ions with a blue ECDL on the strongest line. Figure 6.3 shows the fluorescence signal of the 401.9 nm line.

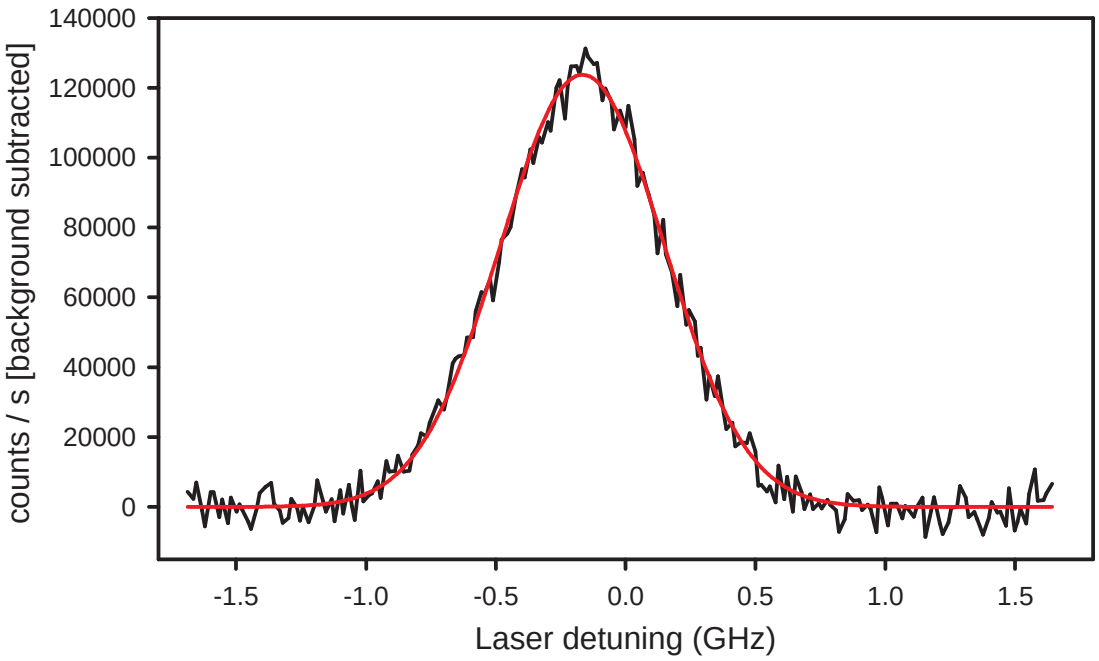

Figure 6.3: Optical detection of the strongest Th^+ line at 401.9 nm.

[8]Hamamatsu C9744 Photon Counting Unit
[9]Hamamatsu C8855 Photon Counting Unit
[10]Ortec MCS-Pci

The observation of the resonance line is already a result of collisional quenching and depopulation of the metastable levels. The pressure of 0.1 Pa ensures a sufficient collision rate for collisions between the helium atoms and the thorium ions. Without the presence of a buffer gas, no fluorescence could be detected.

The temperature dependent Doppler broadened line for different buffer gas pressures is plotted in figure 6.4. To derive the temperature of the ions, the velocities v of the ions have to be calculated according to the Maxwell-Boltzmann distribution

$$f(v)\mathrm{d}v = \frac{1}{\sqrt{2\pi\frac{k_B T}{m}}} e^{-\frac{mv^2}{2k_B T}} \mathrm{d}v \tag{6.1}$$

$$= \frac{1}{\sqrt{2\pi\frac{k_B T}{m}}} e^{-\frac{m\lambda_0^2(\nu-\nu_0)^2}{2k_B T}} \lambda_0 \,\mathrm{d}\nu = S(\nu)\lambda_0 \,\mathrm{d}\nu \;, \tag{6.2}$$

where k_B is the Boltzmann constant, m is the ion mass, $v = \lambda_0 (\nu - \nu_0) = \lambda_0 \Delta\nu$ with $\mathrm{d}v = \lambda_0 \mathrm{d}\nu$, T is the temperature, $S(\nu)$ is the spectrum, ν_0 is the frequency and λ_0 the wavelength of the transition [131].

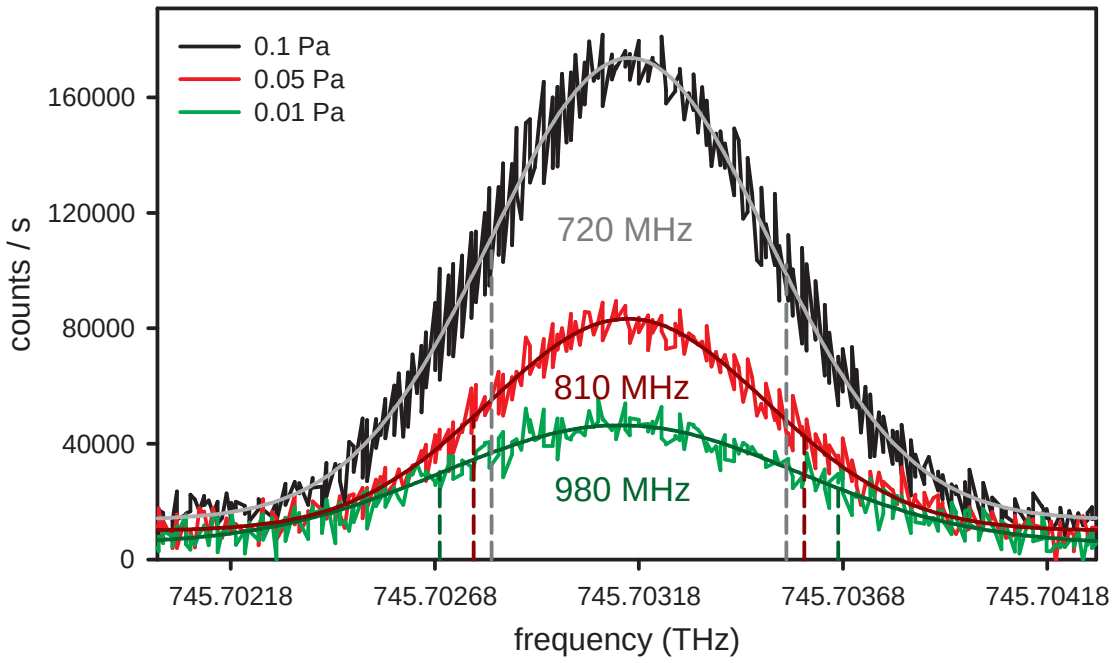

Figure 6.4: Doppler width reduction for different buffer gas pressures.

The full width at half maximum (FWHM) can be calculated from equation (6.2) with the condition $\frac{1}{2}S(\nu_0) = S(\nu_0 \pm \frac{\triangle\nu_{\mathrm{FWHM}}}{2})$ [132] to

$$\triangle\nu_{\mathrm{FWHM}} = \sqrt{\frac{8k_B T \cdot ln\,2}{m\lambda_0^2}} = \sqrt{\frac{8k_B T \cdot ln\,2}{mc^2}}\,\nu_0 \;. \tag{6.3}$$

It can be seen from equation (6.3) that the FWHM scales with $\sqrt{T}$. This can be used to calculate the temperature of the ion cloud and plot the buffer gas pressure dependence of the temperature shown in figure 6.5, using the formula for the temperature derived from equation (6.3):

$$T = \frac{mc^2}{8k_B \cdot ln\,2} \cdot \left(\frac{\Delta\nu_{FWHM}}{\nu_0}\right)^2 . \tag{6.4}$$

It is shown that T reaches approximately room temperature at a pressure of 0.1 Pa.

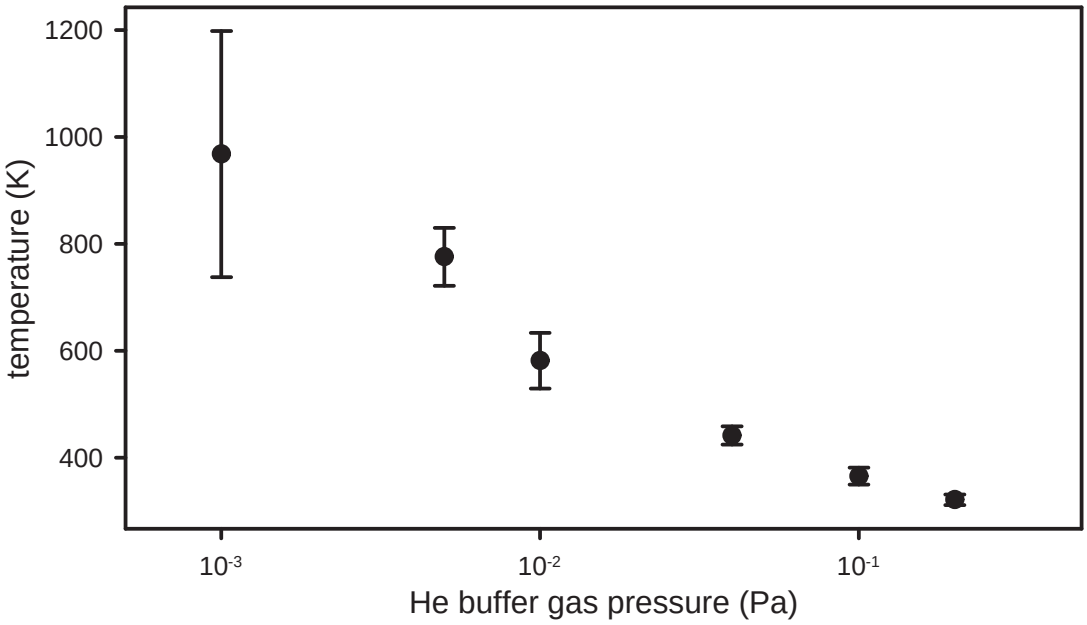

Figure 6.5: Temperature of Th^+ ions versus buffer gas pressure.

Formula (6.4) is correct if the lifetime τ fulfills the condition $\frac{1}{2\pi\tau} \ll \Delta f_{FWHM}$, which means that for long-living excited states, the Lorentz profile of this state can be neglected. The lifetime of the excited state is 23 ns [126] and thus the natural linewidth is $\frac{1}{2\pi\tau} \approx 7$ MHz. This is small compared to the linewidth of 400 MHz in figure 6.3 and the condition can be considered as fulfilled. The natural linewidth is comparable with the Doppler broadening at temperatures below 0.1 K and has to be considered when applying laser cooling techniques.

The relative temperature difference can be calculated as well from the peak height of the signal. At the transition frequency ν_0, the maximum A of the peak is

$$A = S(\nu_0) = \frac{1}{\sqrt{2\pi\frac{k_B T}{m}}} . \tag{6.5}$$

The calculation of the temperature can therefore be achieved by either measuring the height (6.5) or the FWHM (6.3) of the signal.

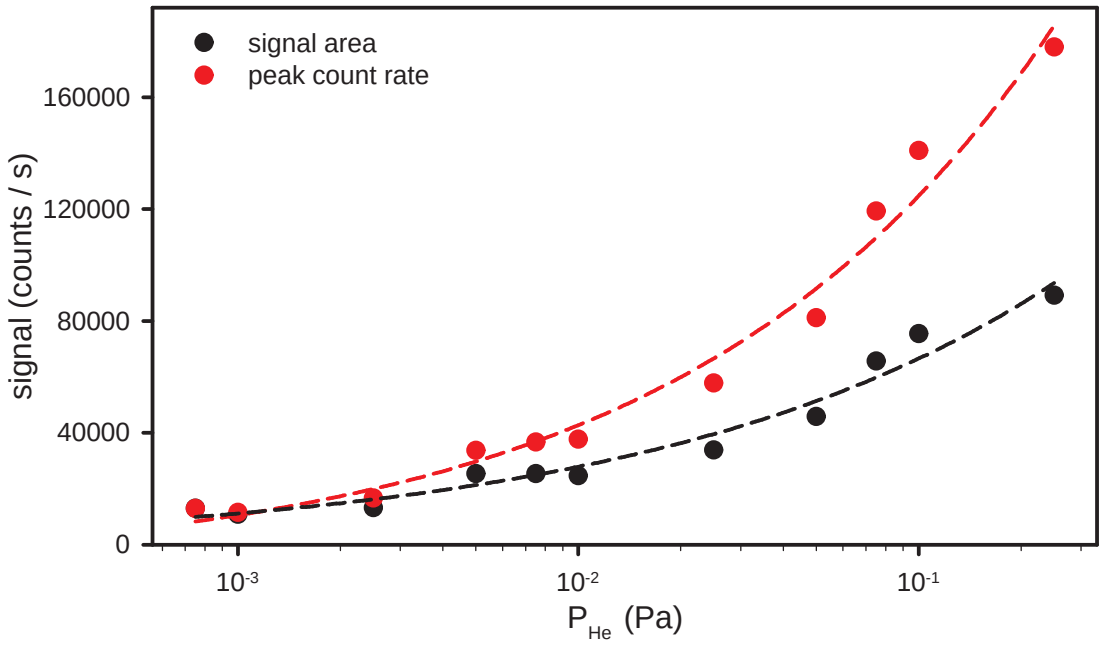

Figure 6.6: Fluorescence count rate dependence of He buffer gas pressure.

The signal area is a quantity for the number of photons that are scattered from each ion. If the buffer gas pressure would only cool the ions, the peak count rate as a quantity for the temperature would increase but the area under the Doppler curve would remain constant. As it can be seen in figure 6.6, the amount of scattered photons increases for higher pressures. This is explained by a higher collision rate between buffer gas atoms and thorium ions and a subsequent higher depopulation rate of the metastable states. Hence, higher buffer gas pressures serve two purposes at the same time — cooling the ions and increasing the quenching rate. When increasing the buffer gas pressure by two orders of magnitude from 10^{-3} Pa to 10^{-1} Pa, the quenching rate increases by a factor of five. This increase is in good agreement with previous measurement of the buffer gas quenching rate in a three-dimensional Paul trap [129].

To calculate the lifetime reduction of the lowest metastable state due to collisional quenching, the quenching rate $\Gamma = 10^{-12}\frac{cm^3}{s}$ for helium [127] has to be taken into account. Using the estimated natural lifetime τ_{nat} of the 1521 cm^{-1} state according to the transition rate A [133]

$$A = \frac{2\pi \cdot e^2 \cdot h}{9\epsilon_0 \cdot m_e^2 \cdot c^2 \cdot \lambda^3} = 0.0628\,\frac{1}{s} \qquad \Rightarrow \qquad \tau_{nat} = \frac{1}{A} \approx 15\,\mathrm{s}\ , \tag{6.6}$$

the reduced lifetime τ of the state can be estimated to

$$\frac{1}{\tau} = n \cdot \Gamma + \frac{1}{\tau_{nat}} \qquad \Rightarrow \qquad \tau \approx 50\,\mathrm{ms} \tag{6.7}$$

with a particle density of $n = 2.4 \cdot 10^{13}\ \frac{1}{\mathrm{cm}^3}$ at a pressure of 0.1 Pa. This reduction of the lifetime is an important part of obtaining a cyclic excitation of the 24873 cm^{-1} state with a single diode laser.

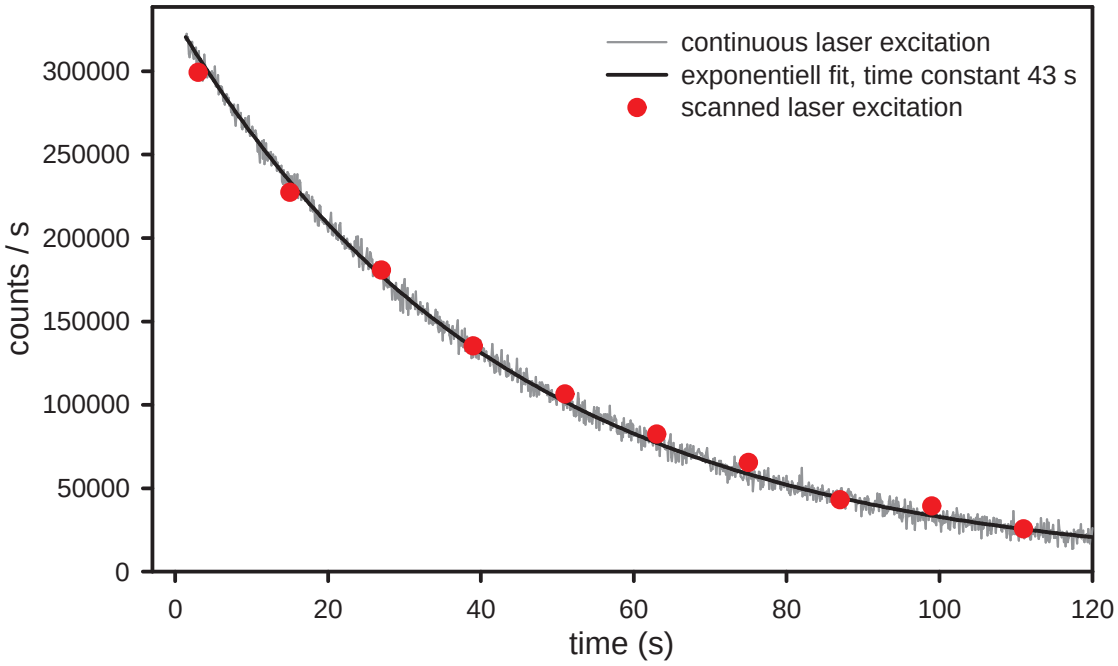

Figure 6.7: Fluorescence count rate for laser radiation with a fixed wavelength tuned to the excitation wavelength and scanned laser radiation every 12 s.

It was observed that the fluorescence signal decreases with time. Since the observed time constant was $\tau < 1$ min and ions could still be observed by channeltron detection after 30 min of storage time, the interaction of the ion cloud with the laser radiation is hindered by a different effect than ion loss. To observe the timescale of this effect, the laser was tuned to the excitation wavelength and the time-dependent changing of the signal was observed. This is marked as continuous laser radiation in figure 6.7. The exponential fit results in a time constant $\tau \approx 43$ s. The time constant prolonged up to 85 s with improvement of vacuum by pumping for two months. For the experiments reported here, the vacuum system had not been baked.

The explanation of the signal decrease is found in the formation of thorium oxide ions. Th^+ has a very high probability of forming oxide molecules and therefore

thorium ions in the trap create more ThO^+ molecules the longer they are stored in the trap. The molecules have a different level scheme and cannot be excited with the 401.9 nm laser.

The formation of thorium oxide is a big problem for every experiment with trapped Th^+ ions. The buffer gas system was built with multiple gas purifiers, heated parts of the buffer gas system and usage of the purest available helium to ensure a low oxygen impurity helium system. However, as it can be seen in figure 6.7, oxide formation has to be strongly avoided (e.g. heating the vacuum system will remove oxygen impurities [134]) before the observation of ^{229m}Th can succeed.

Laser excitation and buffer gas quenching works efficiently on the 401.9 nm line in the given setup. While comparable trap designs achieve a number of about 0.05 detected photons per ion and second [129], it was possible to detect 3 photons/ion/s in this thesis.

7 Summary and Outlook

The present thesis described several steps towards the direct observation of the isomeric state of ^{229}Th. The confirmation of the low-lying state ^{229m}Th would provide a link between nuclear physics and atomic physics and may open a new field of research as well as providing a new approach to current investigations as the search for variations of the fundamental constants.

Thorium recoil atoms ejected from a ^{233}U source have been accumulated on substrates transparent in the 160 nm region. Since the α-decay of ^{233}U will produce thorium atoms where about 2% of the produced nuclei are in the isomeric state, this method served two purposes at once. It overcame the necessity to excite the isomeric state and produced a layer of ^{229m}Th on a substrate that was as free from contaminations with other radioactive atoms as possible. Compared with other methods for separation of radioactive nuclei, for instance chemical separation methods with an execution time of about 30 minutes prior to the experiment, recoil separation is a fast process and allows to start measuring approximately 30 seconds after accumulation. The setback of the experiment was the quality of the uranium source used in the experiment. It had an age of three years and therefore consisted of multiple decay products of the neptunium series with short lifetimes. In addition, it was not a metallic uranium layer but contaminated with other products used in the electroplating process. Hence the obtained capture rate for ^{229m}Th was only about 3–4 per second. The results of the measurement showed no evidence of photons produced in the decay of the isomeric state of thorium. The small detected signal could be explained by Cherenkov radiation in the substrate produced by in the decay of β-emitters implanted and produced on the surface. The negative result led to a complete new scheme for the detection of the isomeric state and the setup of a linear Paul trap.

To obtain the possibility to load an ion trap with thorium ions, laser ablation ion production has been investigated. Laser ablation can remove atoms from a solid surface and ionize the atoms in the created plasma. This overcomes the need for photoionization lasers and creates thorium ions during the very short time span of the 4 ns pulse duration. Thorium could be ablated and singly and doubly charged ions were identified using a time-of-flight mass spectrometer. Other metals generally used in ion trap experiments could be ablated and ionized as well. Highly reactive surfaces such as strontium, that creates an oxide layer when handled in a normal air atmosphere, could be cleaned with multiple laser shots until only Sr^+ was ablated. This offers a new and easy way to load ion traps. Multiple

preparation methods and substrates for a thorium solution were tested and enabled to load our ion trap either by ablation from a metallic ^{232}Th wire or from ^{232}Th in a nitrate. Thereby, it is possible to load ^{229}Th from a solution into the trap in later experiments.

The linear Paul trap was loaded with ^{232}Th and characterized by several different methods. The buffer gas cooling and the influence of the laser ablation velocity distribution were investigated by using a channeltron ion detector, where the trap was completely emptied and the number of stored ions was counted. A voltage of $U_{RF} = 500$ V was sufficient to capture all ions created during the laser ablation. The measured number of stored ions was compared with measurements using the resonant electronic detection of the secular motion, where the ions kept stored in the trap. A number of $8 \cdot 10^4$ trapped ions was confirmed with these measurements.

The short laser pulse width opened a way to measure a possible phase dependence of the ion capture probability with the RF field. The predicted phase dependence [117] was not observed when comparing similar loading conditions. However, the loading conditions changed during observed gas discharges. These discharges were induced by electrons that short circuited the electrodes and led to a higher ion production rate in the plasma during the laser ablation. The probability of the occurrence of these gas discharges showed a high probability for phase angles between -45° and 45° and is explained by phase angle dependent forces on the electrons during the laser ablation.

The establishment of an optical detection method for ions stored in the linear Paul trap was shown. Using buffer gas collision quenching, the metastable levels were depopulated and a closed cycle for the excitation of the 24873 cm^{-1} level was obtained. Higher buffer gas pressure increased the quenching rate and decreased the temperature of the ions in the trap at the same time. The buffer gas allowed to cool the ions to room temperature at a pressure of 0.1 Pa.

Even if the excitation of $^{229\mathrm{m}}$Th became harder with the shift of the expected energy of the isomeric state from 3.5 eV to 7.6 eV in 2007, interest in the isomeric state of ^{229}Th aroused as well in other working groups. Experiments with ionized thorium in a linear Paul trap were conducted with buffer gas cooling and laser ablation loading of Th^{3+}. While experiments in 2008 with trapped $^{232}Th^{3+}$ could only observe a lifetime of about 1.2 s in the trap before decay via charge exchange with vacuum or buffer gas contaminants [135], it was possible in 2009 to cool the ions to room temperature by buffer gas quenching. Thus laser cooling of $^{232}Th^{3+}$ was achieved, increasing the lifetime to about 650 s [134] and obtaining coulomb crystals in a linear ion trap.

The approach of a solid state experiment in a thorium doped crystal [20] is newly revisited [136] in parallel to ion trap experiments. The possibility of conducting nuclear magnetic resonance spectroscopy and Mössbauer experiments with these crystals is a promising alternative to ion trap experiments. The potential to directly

excite the isomeric state of thorium with synchrotron radiation in thorium-doped crystals is a striking reason to follow this approach.

It was not possible to detect the isomeric state in the framework of this thesis. An experimenter is confronted with too many imponderabilia about thorium and its isomeric state to hope for a fast success. This thesis is an intermediate and necessary step towards the direct observation of the isomeric state of thorium. The excitation of the 24873 cm^{-1} level is the first step of the two photon excitation of the atomic shell and the subsequent transfer of the energy to the nucleus. Laser ablation loading and the linear Paul trap are prepared for ^{229}Th. Detection methods are established. ^{229}Th will be installed in the vacuum chamber, oxygen impurities will be removed by baking out the whole system. Spectroscopical studies in the range of 55000 cm^{-1} to 65000 cm^{-1} will reveal the accessible levels and complete the two stage excitation scheme. The direct observation of the isomeric state is pending. It's time to detect the isomeric state.

Bibliography

[1] H. Becquerel. Sur les radiations émises par phosphorescence. *Comptes Rendus*, 122:420–421, 1896.

[2] W. D. Phillips. Nobel Lecture: Laser cooling and trapping of neutral atoms. *Reviews of Modern Physics*, 70(3):721–741, 1998.

[3] T. W. Hänsch. Nobel Lecture: Passion for precision. *Reviews of Modern Physics*, 78(4):1297–1309, 2006.

[4] T. Rosenband, D. B. Hume, p. O. Schmidt, C. W. Chou, A. Brusch, L. Lorini, W. H. Oskay, R. E. Drullinger, T. M. Fortier, J. E. Stalnaker, S. A. Diddams, W. C. Swann, N. R. Newbury, W. M. Itano, D. J. Wineland, and J. C. Bergquist. Frequency Ratio of Al^+ and Hg^+ Single-Ion Optical Clocks; Metrology at the 17th Decimal Place. *Science*, 319(5871):1808–1812, 2008.

[5] T. Remetter, P. Johnsson, J. Mauritsson, K. Varjú, Y. Ni, F. Lépine, E. Gustafsson, M. Kling, J. Khan, R. López-Martens, K. J. Schafer, M. J. J. Vrakking, and A. L'Huillier. Attosecond electron wave packet interferometry. *Nature Physics*, 2(5):323–326, 2006.

[6] J. Mauritsson, P. Johnsson, E. Mansten, M. Swoboda, T. Ruchon, A. L'Huillier, and K. J. Schafer. Coherent Electron Scattering Captured by an Attosecond Quantum Stroboscope. *Physical Review Letters*, 100(7):073003, 2008.

[7] F. Bloch and E. M Purcell. *Nobel Lectures in Physics 1942–1962*, pages 197–234. World Scientific, Singapore, 1993.

[8] T. C. Gibbs. *Principles of Mössbauer spectroscopy.* Chapmann and Hall, London, 1976.

[9] F. Asaro and I. Perlman. Isomeric State of Uranium-235. *Physical Review*, 107(1):318–319, 1957.

[10] J. R. Huizenga, C. L. Rao, and D. W. Engelkemeir. 27-Minute Isomer of U^{235}. *Physical Review*, 107(1):319–320, 1957.

[11] M. S. Freedman, F. T. Porter, F. Wagner, and P. P. Day. Transition in 26-min U^{235m} of Less Than 23 Electron Volts. *Physical Review*, 108(3):836–841, 1957.

[12] G. C. Baldwin and S. A. Wender. Effect of Laser Radiation on the Decay of ^{235m}U. *Physical Review Letters*, 48(21):1461–1464, 1982.

[13] S. Matinyan. Lasers as a bridge between atomic and nuclear physics. *Physics Reports*, 298(4):199–249, 1998.

[14] B. Crasemann. Some aspects of atomic effects in nuclear transitions. *Nuclear Instruments and Methods*, 112(1–2):33–39, 1973.

[15] D. Kekez, A. Ljubičić, K. Pisk, and B. A. Logan. Nuclear Deexcitation via the Electronic-Bridge Mechanism. *Physical Review Letters*, 55(13):1366–1368, 1985.

[16] R. G. Helmer and C. W. Reich. An excited state of ^{229}Th at 3.5 eV. *Physical Review C*, 49(4):1845–1858, 1994.

[17] B. R. Beck, J. A. Becker, P. Beiersdorfer, G. V. Brown, K. J. Moody, J. B. Wilhelmy, F. S. Porter, C. A. Kilbourne, and R. L. Kelley. Energy Splitting of the Ground-State Doublet in the Nucleus ^{229m}Th. *Physical Review Letters*, 98(14):142501, 2007.

[18] W. M. Itano. External-Field Shifts of the $^{199}Hg^{+}$ Optical Frequency Standard. *Journal of Research of the National Institute of Standards and Technology*, 105(6):827–837, 2000.

[19] A. A. Madej and J. E. Bernard. *Frequency measurement and control - advanced techniques and future trends*. Springer, Berlin, 2001.

[20] E. Peik and Chr. Tamm. Nuclear laser spectroscopy of the 3.5 eV transition in Th-229. *EPL (Europhysics Letters)*, 61(2):181–186, 2003.

[21] S. B. Utter, P. Beiersdorfer, A. Barnes, R. W. Lougheed, J. R. Crespo López-Urrutia, J. A. Becker, and M. S. Weiss. Reexamination of the Optical Gamma Ray Decay in ^{229}Th. *Physical Review Letters*, 82(3):505–507, 1999.

[22] E. Browne. Nuclear Data Sheets for A = 235,239. *Nuclear Data Sheets*, 98(3):665–800, 2003.

[23] L. A. Kroger and C. W. Reich. Features of the low-energy level scheme of ^{229}Th as observed in the α-decay of ^{233}U. *Nuclear Physics A*, 259(1):29–60, 1976.

[24] E. Ruchowska, W. A. Płóciennik, J. Żylicz, H. Mach, J. Kvasil, A. Algora, N. Amzal, T. Bäck, M. G. Borge, R. Boutami, P. A. Butler, J. Cederkäll, B. Cederwall, B. Fogelberg, L. M. Fraile, H. O. U. Fynbo, E. Hagebø, P. Hoff, H. Gausemel, A. Jungclaus, R. Kaczarowski, A. Kerek, W. Kurcewicz, K. Lagergren, E. Nacher, B. Rubio, and A. Syntfeld. Nuclear structure of ^{229}Th. *Physical Review C*, 73(4):044326, 2006.

[25] A. M. Dykhne and E. V. Tkalya. Matrix element of the anomalously low-energy (3.5±0.5 eV) transition in ^{229}Th and the isomer lifetime. *JETP Letters*, 67(4):251–256, 1998.

[26] S. Gerstenkorn, P. Luc, J. Verges, D. W. Englekemeir, J. E. Gindler, and F. S. Tomkins. Structures hyperfines du spectre d'étincelle, moment magnétique et quadrupolaire de l'isotope 229 du thorium. *Journal de Physique France*, 35(6):483–495, 1974.

[27] S. G. Nilsson. Binding States of Individual Nucleons in Strongly Deformed Nuclei. *Kongelige Danske Videnskabernes Selskab, Matematisk-fysiske Meddelelser*, 29(16), 1955.

[28] G. Musiol, J. Ranft, R. Reif, and D. Seeliger. *Kern- und Elementarteilchenphysik*. VCH Verlagsgesellschaft, Weinheim, 1988.

[29] W. Demtröder. *Experimentalphysik 4: Kern-, Teilchen- und Astrophysik*. Springer, Berlin, 1998.

[30] L. Bergmann and C. Schaefer. *Band 4: Teilchen*. Lehrbuch der Experimentalphysik. de Gruyter, Berlin, 1992.

[31] K. Gulda, W. Kurcewicz, A. J. Aas, M. J. G. Borge, D. G. Burke, B. Fogelberg, I. S. Grant, E. Hagebø, N. Kaffrell, J. Kvasil, G. Løvhøiden, H. Mach, A. Mackova, T. Martinez, G. Nyman, B. Rubio, J. L. Tain, O. Tengblad, and T. F. Thorsteinsen. The nuclear structure of ^{229}Th. *Nuclear Physics A*, 703(1–2):45–69, 2002.

[32] A. C. Hayes, J. L. Friar, and P. Möller. Splitting sensitivity of the ground and 7.6 eV isomeric states of ^{229}Th. *Physical Review C*, 78(2):024311, 2008.

[33] E. Litvinova, H. Feldmeier, J. Dobaczewski, and V. Flambaum. Nuclear structure of lowest ^{229}Th states and time-dependent fundamental constants. *Physical Review C*, 79(6):064303, 2009.

[34] K. Fajans. Radioactive Transformations and the Periodic System of The Elements. *Berichte der Deutschen Chemischen Gesellschaft*, 46:422–439, 1913.

[35] A. M. Dykhne, N. V. Eremin, and E. V. Tkalya. Alpha decay of the first excited state of the Th-229 nucleus. *JETP Letters*, 64(5):345–349, 1996.

[36] V. F. Strizhov and E. V. Tkalya. Decay channel of low-lying isomer state of the ^{229}Th nucleus, Possibilities of experimental investigation. *Soviet Physics JETP*, 72(3):387, 1991.

[37] E. V. Tkalya, A. N. Zherikhin, and V. I. Zhudov. Decay of the low-energy nuclear isomer ^{229}Th^{m} ($3/2^{+}$, 3.5±1.0 eV) in solids (dielectrics and metals): A new scheme of experimental research. *Physical Review C*, 61(6):064308, 2000.

[38] N. W. Ashcroft and D. N. Mermin. *Solid State Physics*. Thomson Learning, Toronto, 1976.

[39] E. V. Tkalya. Nonradiative decay of the low-lying nuclear isomer ^{229m}Th(3.5 eV) in a metal . *JETP Letters*, 70(6):371–374, 1999.

[40] E. V. Tkalya. Properties of the optical transition in the ^{229}Th nucleus. *Physics-Uspekhi*, 46(3):315–320, 2003.

[41] E. V. Tkalya. Spontaneous emission probability for M1 transition in a dielectric medium: ^{229m}Th($3/2^{+}$, 3.5 ± 1.0 eV) Decay. *JETP Letters*, 71(8):311–313, 2000.

[42] M. Morita. Nuclear Excitation by Electron Transition and Its Application to Uranium 235 Separation. *Progress of Theoretical Physics*, 49(5):1574–1586, 1973.

[43] P. Kálmán and T. Keszthelyi. Laser-driven inverse electronic bridge process: An optical tool for determining low-energy separation of nearby nuclear states. *Physical Review C*, 49(1):324–328, 1994.

[44] F. F. Karpeshin, I. M. Band, M. B. Trzhaskowskaya, and B. A. Zon. Study of ^{229}Th through laser-induced resonance internal conversion. *Physics Letters B*, 282(3–4):267–270, 1992.

[45] F. F. Karpeshin and M. B. Trzhaskovskaya. Impact of the electron environment on the lifetime of the ^{229}Th^{m} low-lying isomer. *Physical Review C*, 76(5):054313, 2007.

[46] F. F. Karpeshin, I. M. Band, and M. B. Trzhaskovskaya. 3.5-eV isomer of ^{229}Th: How it can be produced. *Nuclear Physics A*, 654(3–4):579–596, 1999.

[47] H. G. Dehmelt. Mono-ion oscillator as potential ultimate laser frequency standard. *IEEE Transactions on Instrumentation and Measurement*, 31(2):83–87, 1982.

[48] W. J. Marciano. Time Variation of the Fundamental "Constants" and Kaluza-Klein Theories. *Physical Review Letters*, 52(7):489–491, 1984.

[49] S. G. Karshenboim. Some possibilities for laboratory searches for variations of fundamental constants. *Canadian Journal of Physics*, 78(7):639–678, 2000.

[50] V. V. Flambaum. Variation of Fundamental Constants. *Atomic Physics 20, ICAP 2006*, 869(1):29–36, 2006.

[51] S. Karshenboim, V. Flambaum, and E. Peik. Atomic Clocks and Constraints on Variations of Fundamental Constants. In *Springer Handbook of Atomic, Molecular, and Optical Physics*, pages 455–463. Springer, New York, 2006.

[52] V. V. Flambaum. Enhanced Effect of Temporal Variation of the Fine Structure Constant and the Strong Interaction in Th^{229}. *Physical Review Letters*, 97(9):092502, 2006.

[53] V. V. Flambaum and V. A. Dzuba. Search for variation of the fundamental constants in atomic, molecular, and nuclear spectra. *Canadian Journal of Physics*, 87:25–33, 2009.

[54] J. C. Berengut, V. A. Dzuba, V. V. Flambaum, and S. G. Porsev. Proposed Experimental Method to Determine α Sensitivity of Splitting between Ground and 7.6 eV Isomeric States in ^{229}Th. *Physical Review Letters*, 102(21):210801, 2009.

[55] D. G. Burke, P. E. Garrett, T. Qu, and R. A. Naumann. Additional evidence for the proposed excited state at $\leq$ 5 eV in ^{229m}Th. *Physical Review C*, 42(2):R499–R501, 1990.

[56] C. W. Reich and R. G. Helmer. Energy Separation of the Douplet of Intrinsic States at the Ground State of ^{229}Th. *Physical Review Letters*, 64(3):271–273, 1990.

[57] O. V. Vorykhalov and V. V. Koltsov. Search for an Isomeric Transition of Energy Below 5eV in ^{229}Th Nucleus. *Bulletin of the Russian Academy of Science: Physics*, 59(1):20–24, 1995.

[58] T. T. Inamura and H. Haba. Search for a "3.5-eV isomer" in ^{229}Th in a hollow-cathode electric discharge. *Physical Review C*, 79(3):034313, 2009.

[59] T. Mitsugashira, M. Hara, T. Ohtsuki, H. Yuki, K. Takamiya, Y. Kasamatsu, A. Shinohara, H. Kikunaga, and T. Nakanishi. Alpha-decay from the 3.5 eV isomer of ^{229}Th. *Journal of Radioanalytical and Nuclear Chemistry*, 255(1):63–66, 2003.

[60] G. M. Irwin and K. H. Kim. Observation of Electromagnetic Radiation from Deexcitation of the ^{229}Th Isomer. *Physical Review Letters*, 79(6):990–993, 1997.

[61] D. S. Richardson, D. M. Benton, D. E. Evans, J. A. R. Griffith, and G. Tungate. Ultraviolet Photon Emission Observed in the Search for the Decay of the ^{229}Th Isomer. *Physical Review Letters*, 80(15):3206–3208, 1998.

[62] J. P. Young, R. W. Shaw, and O. F. Webb. Spectral Studies Related to the 3.5 eV Isomeric State of Th-229. *AIP Conference Proceedings*, 454:235–242, 1998.

[63] Y. Kasamatsu, H. Kikunaga, K. Takamiya, T. Mitsugashira, T. Nakanishi, Y. Ohkubo, T. Ohtsuki, W. Sato, and A. Shinohara. Search for the decay of ^{229m}Th by photon detection. *Radiochimica Acta*, 93:511–514, 2005.

[64] G. M. Irwin and K. H. Kim. Comment. *Physical Review Letters*, 83(5):1073, 1999.

[65] K. Pachucki, S. Wycech, J. Żylicz, and M. Pfützner. Nuclear-spin mixing oscillations in ^{229}Th^{89+}. *Physical Review C*, 64(6):064301, 2001.

[66] I. M. Band. Discrete conversion of gamma rays in ^{229}Th and in highly ionized ^{125}Te^{Q} ions. *Journal of Experimental and Theoretical Physics*, 93(5):948–956, 2001.

[67] F. F. Karpeshin, I. M. Band, M. B. Trzhaskovskaya, and M. A. Listengarten. Optical pumping ^{229m}Th through NEET as a new effective way of producing nuclear isomers. *Physics Letters B*, 372(1–2):1–7, 1996.

[68] P. Kálmán and T. Bükki. Deexcitation of ^{229}Th^{m}: Direct γ decay and electronic-bridge process. *Physical Review C*, 63(2):027601, 2001.

[69] Z. O. Guimar aes Filho and O. Helene. Energy of the $3/2^+$ state of ^{229}Th reexamined. *Physical Review C*, 71(4):044303, 2005.

[70] V. Barci, G. Ardisson, G. Barci-Funel, B. Weiss, O. El Samad, and R. K. Sheline. Nuclear structure of ^{229}Th from γ-ray spectroscopy study of ^{233}U α-particle decay. *Physical Review C*, 68(3):034329, 2003.

[71] R. G. Helmer and C. van der Leun. Recommended standards for γ-ray energy calibration (1999). *Nuclear Instruments and Methods in Physics Research Section A: Accelerators, Spectrometers, Detectors and Associated Equipment*, 450(1):35–70, 2000.

[72] C. K. Stahle, C. A. Allen, K. R. Boyce, R. P. Brekosky, G. V. Brown, J. Cottam, E. Figueroa-Feliciano, M. Galeazzi, J. D. Gygax, M. B. Jacobson, R. L. Kelley, D. Liu, D. McCammon, R. A. McClanahan, S. H. Moseley, F. S. Porter, L. E. Rocks, A. E. Szymkowiak, and J. E. Vaillancourt. The next-generation microcalorimeter array of XRS on Astro-E2. *Nuclear Instruments and Methods in Physics Research Section A: Accelerators, Spectrometers, Detectors and Associated Equipment*, 520(1–3):466–468, 2004.

[73] E. Peik. Long-lasting photoluminescence in polymers. *Journal of Physics D: Applied Physics*, 40(11):3330–3334, 2007.

[74] P. A. Čerenkov. *Nobel Lectures in Physics 1942–1962*, pages 426–440. World Scientific, Singapore, 1999.

[75] E. Browne, E. B. Norman, R. D. Canaan, D. C. Glasgow, J. M. Keller, and J. P. Young. Search for decay of the 3.5-eV level in ^{229}Th. *Physical Review C*, 64(1):014311, 2001.

[76] Y.A. Akovali. Nuclear data sheets for A = 233. *Nuclear Data Sheets*, 59(1):263–331, 1990.

[77] M. J. Berger, J. S. Coursey, M. A. Zucker, and J. Chang. Stopping-Power and Range Tables for Electrons, Protons, and Helium Ions. NISTIR 4999, NIST Standard Reference Database 124.

[78] J. F. Ziegler. Srim-2003. *Nuclear Instruments and Methods in Physics Research Section B: Beam Interactions with Materials and Atoms*, 219–220:1027–1036, 2004.

[79] T. Mayer-Kuckuk. *Physik der Atomkerne*. Teubner, Stuttgart, 1970.

[80] H. Bateman. The solution of a system of differential equations occurring in the theory of radioactive transformations. *Proceedings of the Cambridge Philosophical Society*, 15:423–427, 1910.

[81] E. H. Belcher. The Luminescence of Irradiated Transparent Media and the Cerenkov Effect. I. The Luminescence of Aqueous Solutions of Radioactive Isotopes. *Proceedings of the Royal Society of London. Series A. Mathematical and Physical Sciences*, 216(1124):90–102, 1953.

[82] Y.A. Akovali. Nuclear data sheets for A = 229. *Nuclear Data Sheets*, 58(2):555–588, 1989.

[83] L. Gmelin. *Gmelins Handbuch der anorganischen Chemie. System-Nummer 44. Thorium und Isotope*. Deutsche Chemische Gesellschaft, Berlin, 8th edition, 1926.

[84] R. Srinivasan. Ablation of polymers and biological tissue by ultraviolet lasers. *Science*, 234(4776):559–565, 1986.

[85] W. E. Stephens. A Pulsed Mass Spectrometer with Time Dispersion. *Physical Review*, 69(11–12):691, 1946.

[86] C. Phipps. *Laser Ablation and its Applications*. Springer, Berlin, 2007.

[87] Q. Lu, S. S. Mao, X. Mao, and R. E. Russo. Delayed phase explosion during high-power nanosecond laser ablation of silicon. *Applied Physics Letters*, 80(17):3072–3074, 2002.

[88] J. C. Miller and R. F. Haglund. *Laser Ablation and Desorption*. Academic Press, New York, 1998.

[89] S. D. Brorson, A. Kazeroonian, J. S. Moodera, D. W. Face, T. K. Cheng, E. P. Ippen, M. S. Dresselhaus, and G. Dresselhaus. Femtosecond room-temperature measurement of the electron-phonon coupling constant γ in metallic superconductors. *Physical Review Letters*, 64(18):2172–2175, 1990.

[90] G. L. Eesley. Generation of nonequilibrium electron and lattice temperatures in copper by picosecond laser pulses. *Physical Review B*, 33(4):2144–2151, 1986.

[91] B. N. Chichkov, C. Momma, S. Nolte, F. von Alvensleben, and A. Tünnermann. Femtosecond, picosecond and nanosecond laser ablation of solids. *Applied Physics A: Materials Science & Processing*, 63(2):109–115, 1996.

[92] E. Bernal G., L. P. Levine, and J. F. Ready. Time-of-Flight Spectrometer for Laser Surface Interaction Studies. *Review of Scientific Instruments*, 37(7):938–941, 1966.

[93] R. D. Knight. Storage of ions from laser-produced plasmas. *Applied Physics Letters*, 38(4):221–223, 1981.

[94] M. Hashida, A. F. Semerok, O. Gobert, G. Petite, Y. Izawa, and J. F-. Wagner. Ablation threshold dependence on pulse duration for copper. *Applied Surface Science*, 197–198:862–867, 2002.

[95] L. Torrisi, G. Ciavola, S. Gammino, L. Ando, A. Barna, L. Laska, and J. Krasa. Metallic etching by high power Nd:yttrium–aluminum–garnet pulsed laser irradiation. *Review of Scientific Instruments*, 71(11):4330–4334, 2000.

[96] W. C. Wiley and I. H. McLaren. Time-of-Flight Mass Spectrometer with Improved Resolution. *Review of Scientific Instruments*, 26(12):1150–1157, 1955.

[97] B.T. Chait and K. G. Standing. A time-of-flight mass spectrometer for measurement of secondary ion mass spectra. *International Journal of Mass Spectrometry and Ion Physics*, 40(2):185–193, 1981.

[98] B. Thestrup, B. Toftmann, J. Schou, B. Doggett, and J. G. Lunney. Ion dynamics in laser ablation plumes from selected metals at 355 nm. *Applied Surface Science*, 197–198:175–180, 2002.

[99] M. Guilhaus. Special feature: Tutorial. Principles and Instrumentation in Time-of-flight Mass Spectrometry. Physical and Instrumental Concepts. *Journal of Mass Spectrometry*, 30(11):1519–1532, 1995.

[100] G. A. M. Hussein. Rare earth metal oxides: formation, characterization and catalytic activity Thermoanalytical and applied pyrolysis review. *Journal of Analytical and Applied Pyrolysis*, 37(2):111–149, 1996.

[101] G. Grundmeier and B. Schinkinger. Ultra-dünne Schichten auf Basis der Flammenpyrolyse. In *Jahrbuch der Oberflächentechnik*, pages 83–87. Eugen G. Leuze Verlag, Bad Saulgau, 2005.

[102] H. G. Dehmelt. *Advances in Atomic Molecular and Optical Physics 3*, page 53. Academic Press, New York, 1967.

[103] W. Paul, O. Osberghaus, and E. Fischer. Ein Ionenkäfig. *Forschungsberichte des Wirtschafts- und Verkehrsministeriums Nordrhein-Westfalen*, 413, 1958.

[104] G. Werth, V. Gheorghe, and F. G. Major. *Charged particle traps II: Applications*. Springer Series on Atomic, Optical, and Plasma Physics. Springer, Berlin, 2009.

[105] F. G. Major, V. N. Gheorghe, and G. Werth. *Charged Particle Traps: Physics and Techniques of Charged Particle Field Confinement*. Springer Series on Atomic, Optical, and Plasma Physics. Springer, Berlin, 2005.

[106] W. Paul. *Nobel Lectures in Physics 1981–1990*, pages 601–622. World Scientific, Singapore, 1993.

[107] W. Paul and H. Steinwedel. Ein neues Massenspektrometer ohne Magnetfeld. *Zeitschrift für Naturforschung Teil A*, 8:448–450, 1953.

[108] M. G. Raizen, J. M. Gilligan, J. C. Bergquist, W. M. Itano, and D. J. Wineland. Ionic crystals in a linear Paul trap. *Physical Review A*, 45(9):6493–6501, 1992.

[109] L. Ruby. Applications of the Mathieu equation. *American Journal of Physics*, 64(1):39–44, 1996.

[110] P. K. Ghosh. *Ion Traps*. Clarendon Press, Oxford, 1995.

[111] L. D. Landau and E. M. Lifshitz. §30. Bewegung im schnell oszillierenden Feld. In *Lehrbuch der Theoretischen Physik. Band I: Mechanik*, pages 107–110. Akademie-Verlag, Berlin, 1962.

[112] F. v. Busch and W. Paul. Über nichtlineare Resonanzen im elektrischen Massenfilter als Folge von Feldfehlern. *Zeitschrift für Physik A Hadrons and Nuclei*, 164(5):588–594, 1961.

[113] F. Diedrich, E. Peik, J. M. Chen, W. Quint, and H. Walther. Observation of a Phase Transition of Stored Laser-Cooled Ions. *Physical Review Letters*, 59(26):2931–2934, 1987.

[114] D. R. Denison. Operating Parameters of a Quadrupole in a Grounded Cylindrical Housing. *Journal of Vacuum Science and Technology*, 8(1):266–269, 1971.

[115] R. Iffländer and G. Werth. Optical Detection of Ions Confined in a rf Quadrupole Trap. *Metrologia*, 13(3):167–170, 1977.

[116] H. A. Schuessler, E. N. Fortson, and H. G. Dehmelt. Hyperfine Structure of the Ground State of $^3He^+$ by the Ion-Storage Exchange-Collision Technique. *Physical Review*, 187(1):5, 1969.

[117] E. Fischer. Die dreidimensionale Stabilisierung von Ladungsträgern in einem Vierpolfeld. *Zeitschrift für Physik*, 156(1):1–26, 1959.

[118] Kristian Mølhave. *Construction of and Experiments with a Linear Paul Trap*. Masters Thesis, Institute of Physics and Astronomy, Århus, Denmark, 2000.

[119] F. G. Major and H. G. Dehmelt. Exchange-Collision Technique for the rf Spectroscopy of Stored Ions. *Physical Review*, 170(1):91–107, 1968.

[120] F. Arbes, T. Gudjons, F. Kurth, G. Werth, F. Marin, and M. Inguscio. Lifetime measurements of the $3D_{3/2}$ and $3D_{5/2}$ metastable states in CaII. *Zeitschrift für Physik D Atoms, Molecules and Clusters*, 25(4):295–298, 1993.

[121] O Chun-Sing and H. A. Schuessler. Mass-selective trapping of pulsed charged particle beams. *Applied Physics B: Lasers and Optics*, 27(3):129–135, 1982.

[122] V. H. S. Kwong. Production and storage of low-energy highly charged ions by laser ablation and an ion trap. *Physical Review A*, 39(9):4451–4454, 1989.

[123] Y. Hashimoto, L. Matsuoka, H. Osaki, Y. Fukushima, and S. Hasegawa. Trapping Laser Ablated Ca^+ Ions in Linear Paul Trap. *Japanese Journal of Applied Physics*, 45(9A):7108–7113, 2006.

[124] D. B. Robb and M. W. Blades. Optimum phase angle for laser desorption ion trap mass spectrometry is dependent on the number of ions produced. *International Journal of Mass Spectrometry*, 190–191:69–80, 1999.

[125] R. Zalubas and C. H. Corliss. Energy Levels and Classified Lines in the Second Spectrum of Thorium (Th II). *Journal of research of the National Bureau of Standards. Section A. Physics and chemistry*, 78A(2):163–246, 1974.

[126] H. Nilsson, Z. G. Zhang, H. Lundberg, S. Johansson, and B. Nordström. Experimental oscillator strengths in Th II. *Astronomy & Astrophysics*, 382:368–377, 2002.

[127] M. Knoop, M. Vedel, and F. Vedel. Collisional quenching and j-mixing rate constants for the $3D$ levels of Ca^+. *Physical Review A*, 58(1):264–269, 1998.

[128] G. Tommaseo, T. Pfeil, G. Revalde, G. Werth, P. Indelicato, and J. P. Desclaux. The g_J-factor in the ground state of Ca^+. *The European Physical Journal D - Atomic, Molecular, Optical and Plasma Physics*, 25(2):113–121, 2003.

[129] W. Kälber. *Kernladungsradien und Kernmomente von Thorium-Isotopen aus laserspektroskopischen Untersuchungen an gespeicherten Thorium-Ionen in einer Hochfrequenz-Ionenfalle*. PhD Thesis, Kernforschungszentrum Karlsruhe, Karlsruhe, Germany, 1989.

[130] B. A. Palmer and R. Jr. Engleman. *Atlas of the Thorium Spectrum*. Los Alamos National Laboratory, Los Alamos, 1983.

[131] C. Gerthsen and H. Vogel. *Gerthsen Physik*. Springer, Berlin, 19th edition, 1997.

[132] H. Haken and H. C. Wolf. *Atom- und Quantenphysik*. Springer, Berlin, 8th edition, 2003.

[133] I. I. Sobel'man. *Atomic Spectra and Radiative Transitions*. Springer, Berlin, 2nd edition, 1992.

[134] C. J. Campbell, A. V. Steele, L. R. Churchill, M. V. DePalatis, D. E. Naylor, D. N. Matsukevich, A. Kuzmich, and M. S. Chapman. Multiply Charged Thorium Crystals for Nuclear Laser Spectroscopy. *Physical Review Letters*, 102(23):233004, 2009.

[135] A. V. Steele. *Barium ion cavity qed and triply ionized thorium ion trapping*. PhD Thesis, Georgia Institute of Technology, Atlanta, USA, 2008.

[136] W. G. Rellergert, D. DeMille, R. R. Greco, M. P. Hehlen, J. R. Torgerson, and E. R. Hudson. Optical transition in the ^{229}Th nucleus in a solid-state environment. *arXiv*, 0905.2230v2, 2010.

Danksagung

Physik ist gar nicht so schwer. Eine Danksagung schon. Denn Danke sagen muss man ganz allein, während ich mich glücklich schätzen darf, niemals mit der Physik allein gelassen worden zu sein. In den vergangenen Jahren haben viele Menschen mein Leben bereichert, indem sie ihr Wissen, ihre Erfahrung, ihr Können und ihre Zeit mit mir geteilt haben und dadurch sowohl zu einem wichtigen Teil dieser Arbeit als auch meines Lebens geworden sind. Diese Seite kann niemals ausreichen, um mich bei all diesen Menschen angemessen zu bedanken. Es ist mir wichtig, es trotzdem zu versuchen.

Zuallererst möchte ich meinem Doktorvater Ekkehard Peik ganz herzlich danken. Sein fantastisches Verständnis für die Zusammenhänge der Physik, seine Fähigkeit, diese Zusammenhänge auch zu vermitteln sowie seine immer hilfsbereite und freundliche Art haben mein Leben und diese Arbeit mehr als bereichert und machen ihn auf seine ganz besondere Weise zum besten Mentor, den ich mir wünschen konnte.

Für die wundervolle Zeit, die wir gemeinsam nicht nur im Labor verbracht haben und in der ich sehr viel lernen konnte, möchte ich Maxim Okhapkin danken. Vor allem die leidenschaftlichen, russisch lauten Diskussionen werden mir noch lange in Erinnerung bleiben. Mit Andrey Herrera verbinden mich viele gemeinsame Monate im Labor beim Basteln, Schrauben und Messen, die dadurch nicht nur doppelt interessant, sondern auch unterhaltsam wurden. Darüber hinaus haben sowohl Maxim als auch Andrey meinen Wortschatz durch wildes Arbeitsgruppen-Esperanto außergewöhnlich erweitert.

Ganz fantastische Unterstützung habe ich von Thomas Leder und Dieter Griebsch erhalten. Wilde Skizzen wurden gemeinsam mit ihren Ideen und ihrer Hilfe von „undurchführbar“ zu „genau was ich brauche“ umkonstruiert und meisterhaft in die Tat umgesetzt.

Im Kopfermann-Bau habe ich dank Thomas Polewka, Jürgen Becker und Michael Rost eine sehr angenehme Arbeitsatmosphäre genießen dürfen, in der mir auch bei der ausgefallensten Frage noch engagiert geholfen wurde. Desweiteren gilt mein Dank natürlich Christian Tamm und allen Mitarbeitern des Fachbereichs Zeit und Frequenz, die mir immer tatkräftig, hilfsbereit und freundlich zur Seite standen.

Mein größtes Dankeschön gilt jedoch denjenigen, die mein Leben liebevoll begleiten und jeden Tag zu einem besonderen Tag werden lassen: Meinen Freunden, meinen Eltern mit ihrer grenzenlosen Unterstützung und Ilka, die immer für mich da ist.

Curriculum Vitae

Name:	Kai Zimmermann
Date of birth:	25th December 1976
Place of birth:	Berlin, Germany

01.07.1983 – 31.06.1989	Grundschule auf dem Tempelhofer Feld, Berlin
01.07.1989 – 31.06.1996	Askanisches Gymnasium, Berlin School leaving certificate: Abitur
01.09.1996 – 30.09.1997	Civil service in a residential home for mentally handicapped persons of the Lebenshilfe e.V. in the field of occupational therapy
01.10.1997 – 14.10.2003	Technische Universität Berlin University degree: Diplom-Physiker
01.11.2003 – 15.09.2004	One year stay abroad in Australia
01.07.2005 – 30.06.2009	Research assistant at the Institute of Quantum Optics of the Gottfried Wilhelm Leibniz Universität Hannover, place of work Physikalisch-Technische Bundesanstalt in Braunschweig
01.07.2009 –	Research assistant at the Physikalisch-Technische Bundesanstalt in Braunschweig